12-24-2016

Nuclear Structure of ^{186}Re

David A. Matters

Recommended Citation

Matters, David A., "Nuclear Structure of ^{186}Re" (2016). *Theses and Dissertations*. 497.
https://scholar.afit.edu/etd/497

Nuclear Structure of ^{186}Re

DISSERTATION

David A. Matters, Major, USA
AFIT-ENP-DS-16-D-017

DEPARTMENT OF THE AIR FORCE
AIR UNIVERSITY

AIR FORCE INSTITUTE OF TECHNOLOGY

Wright-Patterson Air Force Base, Ohio

DISTRIBUTION STATEMENT A
APPROVED FOR PUBLIC RELEASE; DISTRIBUTION UNLIMITED

AFIT-ENP-DS-16-D-017

NUCLEAR STRUCTURE OF ^{186}RE

DISSERTATION

Presented to the Faculty
Graduate School of Engineering and Management
Air Force Institute of Technology
Air University
Air Education and Training Command
in Partial Fulfillment of the Requirements for the
Degree of Doctor of Philosophy

David A. Matters, BA, MA, MBA, MS
Major, USA

December 2016

DISTRIBUTION STATEMENT A
APPROVED FOR PUBLIC RELEASE; DISTRIBUTION UNLIMITED

AFIT-ENP-DS-16-D-017

NUCLEAR STRUCTURE OF ^{186}RE

DISSERTATION

David A. Matters, BA, MA, MBA, MS
Major, USA

Committee Membership:

J. W. McClory, Ph.D.
Chair

J. J. Carroll, Ph.D.
Member

K. C. Gross, Ph.D.
Member

W. P. Baker, Ph.D.
Member

AFIT-ENP-DS-16-D-017

Abstract

The unstable odd-Z, odd-N isotope ^{186}Re exists in a mid-shell deformed region of the chart of the nuclides where long-lived nuclear isomers are common. ^{186}Re (ground-state half-life $T_{1/2} = 3.7186$ d) has an isomer with a half-life of $\sim 2.0 \times 10^5$ y. The ^{186m}Re isomer is a candidate energy-storage medium for a radioisotope power source of military importance that would operate on the principle of isomer depletion. Data about levels and transitions above the ^{186m}Re isomer, absent from the adopted level scheme for ^{186}Re, are needed to identify a means of depleting the isomer. Four experiments were performed to investigate the ^{186}Re level structure, which involved three different reactions: $^{187}\text{Re}(n, 2n\gamma)^{186}\text{Re}$, $^{185}\text{Re}(n, \gamma)^{186}\text{Re}$, and $^{186}\text{W}(d, 2n\gamma)^{186}\text{Re}$. In each of these experiments, γ-ray spectra from the decay of excited states in ^{186}Re were measured and analyzed to reveal information about the discrete-level structure of ^{186}Re. This work resulted in new information about γ-ray transitions that feed the ^{186m}Re isomer, an improved value for the excitation energy of the isomer, independent measurements of the ^{186}Re neutron-separation energy and the cross section for thermal-neutron capture on ^{185}Re, and numerous γ-ray transitions and levels in ^{186}Re which are not included in the adopted level scheme.

To Megan, Xavier, and Aurelia

Acknowledgements

I would first like express my gratitude to my dissertation committee for their guidance throughout my studies, and for the autonomy they granted me during my research efforts. Special thanks are due to my advisor, Dr. John McClory, who supported me in my lifelong goal of becoming a physicist. Without his advocacy on my behalf, I would not have had the opportunity to to extend my time at AFIT and complete a Ph.D. at this point in my Army career. I am very grateful to Dr. Jeff Carroll and Dr. Chris Chiara of the Army Research Laboratory for their mentorship and instruction in the fascinating field of nuclear-structure physics. I had many opportunities to collaborate with nuclear physicists around the world who deserve sincere thanks for their guidance during experiments, data analysis, and manuscript production: Drs. Nik Fotiades, Ron Nelson, and Matt Devlin of Los Alamos Neutron Science Center, Drs. Aaron Hurst and Rick Firestone of Lawrence Berkeley National Laboratory, Dr. Laszlo Szentmiklósi of the Budapest Neutron Centre, Dr. Milan Krtička of Charles University in Prague, Drs. Filip Kondev and Mike Carpenter of Argonne National Laboratory, and Dr. Greg Lane of the Australian National University. Finally, recognition is due to the agencies that funded my travel for the projects described in this document: the Defense Threat Reduction Agency and the Domestic Nuclear Detection Office of the Department of Homeland Security.

David A. Matters

Table of Contents

List of Figures

Figure Page

List of Tables

List of Abbreviations

Abbreviation		Page
IT	isomeric transition	1
USNDP	U.S. Nuclear Data Program	2
NNDC	National Nuclear Data Center	2
ENSDF	Evaluated Nuclear Structure Data File	2
XUNDL	eXperimental Unevaluated Nuclear Data List	2
ENDF	Evaluated Nuclear (reaction) Data File	2
IAEA	International Atomic Energy Agency	2
RIPL	Reference Input Parameter Library	3
GEANIE	GErmanium Array for Neutron Induced Excitations	8
LANSCE	Los Alamos Neutron Science Center	8
BRR	Budapest Research Reactor	9
BNC	Budapest Neutron Centre	9
PGAA	Prompt Gamma-ray Activation Analysis	9
HPGe	high-purity germanium	9
ANU	Australian National University	9
RCNP	Research Center for Nuclear Physics	10
CAGRA	Clover Array Gamma-ray spectrometer at RCNP for Advanced research	10
ICC	internal conversion coefficient	16
BrIcc	Band-Raman Internal Conversion Calculator	16
BCS	Bardeen-Cooper-Schrieffer	29
IS	intermediate state	49

Abbreviation		Page
ICS	integrated cross sections	50
NSR	Nuclear Science References	52
EGAF	Evaluated Gamma-ray Activation File	54
ARL	Army Research Laboratory	55
BGO	bismuth germanate	60
ToF	time-of-flight	60
LBNL	Lawrence Berkeley National Laboratory	72
LD	level density	84
PSF	photon strength function	84
CTF	constant temperature formula	85
BSFG	backshifted Fermi gas	85
BA	Brink-Axel	87
KMF	Kadmenski, Markushev, and Furman	87
GLO	generalized Lorentzian	87
MGLO	modified generalized Lorentzian	87
P-D	population-depopulation	101
AME	Atomic Mass Evaluation	113
ANL	Argonne National Laboratory	116
LEPS	low-energy photon spectrometers	119

NUCLEAR STRUCTURE OF ^{186}RE

I. Introduction

1.1 Background

Rhenium ($Z = 75$) is a transition element that exists naturally in two isotopes: ^{185}Re (abundance 37.398%) and ^{187}Re (abundance 62.602%) [1]. Rhenium has the notable physical property that its melting point among metallic elements is second only to tungsten, which makes it suitable for use in high-temperature applications. Due to its rarity, rhenium metal is very expensive [2].

The unstable odd-Z, odd-N isotope ^{186}Re has a half-life in its ground state of 3.7186 days, from which it decays via electron capture (7.47%) to form ^{186}W or by β^- emission (92.53%) to ^{186}Os. ^{186}Re has an unusually long-lived metastable state (isomer) with a half-life of $\sim 2.0 \times 10^5$ years. The ^{186m}Re isomer (identified with a superscript m for metastable) decays only by γ-ray cascade to the ground state, in the process known as isomeric transition (IT) [3, 4].

1.2 Motivation

Research on ^{186}Re is motivated by the need for nuclear-structure and reaction data, astrophysical questions concerning the rhenium/osmium cosmochronometer, and the possible use of long-lived isomers in the development of a radioisotope power source.

1.2.1 Nuclear Data Needs.

The U.S. Nuclear Data Program (USNDP) is managed by the National Nuclear Data Center (NNDC) at Brookhaven National Laboratory. The databases maintained by the NNDC are organized according to application, and include nuclear-structure as well as nuclear-reaction data. Among these databases are the Evaluated Nuclear Structure Data File (ENSDF) and the eXperimental Unevaluated Nuclear Data List (XUNDL), which contain information about nuclear level schemes, and the Evaluated Nuclear (reaction) Data File (ENDF), which holds cross-section information for various nuclear reactions. Data published in nuclear-science journals are evaluated periodically for inclusion in the evaluated databases.

The nuclear data maintained in these databases are important to applications across the spectrum of nuclear science and technology. Advanced reactor design, nonproliferation, nuclear medicine, national security, and basic science all rely on accurate structure and reaction data maintained in the evaluated databases [5].

Nonproliferation/Safeguards.

Active and passive interrogation technologies used in nonproliferation applications such as the detection of special nuclear materials rely on activation cross sections from the ENDF and γ-ray energies from the ENSDF. Nuclear-reaction and structure data are also used by the International Atomic Energy Agency (IAEA) for nuclear-materials safeguards, in which elemental- and isotopic-composition analysis is used to identify potential reprocessing of spent nuclear fuel.

Nuclear Power.

Advanced nuclear-reactor designs rely on reaction cross-section data for the purpose of evaluating structural materials used throughout the reactor and in the nuclear fuel cycle. Data maintained in the ENDF are particularly important in these applications, and there is a continued effort to make these data more accurate as design margins in advanced reactor designs improve.

Nuclear Medicine.

The ground state of ^{186}Re has a medical application as a high specific-activity β^- emitter, useful for the treatment of certain bone and breast cancers. Due to its relatively short half-life, production of this isotope must be maintained continuously to maintain a consistent supply for patients in need of this type of treatment. As part of the U.S. Department of Energy's isotope program, ^{186}Re is produced by thermal neutron capture on ^{185}Re at reactors, or by proton-induced reactions on tungsten at accelerator facilities [6, 7]. Accurate reaction cross sections are important to planning the national effort to maintain a supply of ^{186}Re for medical treatment.

Validation of Nuclear Models.

^{186}Re lies at the edge of a mid-shell deformed region of the chart of the nuclides, and experimental nuclear data regarding isotopes in this mass region are important for validating models of nuclear structure and reactions. The ENSDF feeds a specific data library relevant to nuclear-reaction models, the Reference Input Parameter Library (RIPL), which is maintained by the IAEA and used as the default library in most major nuclear-reaction codes (including the Talys 1.6, CoH 3.4, and dicebox codes used in this research). When experimental cross-section data are not available, modeled cross sections produced by codes such as TALYS provide the input to the ENDF database, so accurate nuclear data in RIPL are especially important for applications [8, 9].

1.2.2 Re-Os Cosmochronometer.

^{187}Re has a ground-state half-life of 4.33×10^{10} years, and it decays by β^- emission to form the stable isotope ^{187}Os [10]. A comparison of the relative abundances of ^{187}Os and ^{187}Re in astronomical objects such as meteorites allows one to estimate the duration of time from the synthesis of these nuclides in high neutron-flux events [11]. Because the half-life of ^{187}Re is on the order of the age of the universe ($15 \pm 2 \times 10^9$ y), these estimates are useful for dating supernova events up to the age of the Milky Way galaxy [12].

Nucleosynthesis involves the study of nuclear reactions in stellar environments, resulting in the production of elements heavier than hydrogen. The formation of the isotopes ^{187}Re and ^{187}Os involves two processes: a rapid (r) process and a slow (s) process, so defined by the rate of neutron-capture events in the stellar environment. Both the s and r processes populate the neutron-heavy radionuclides, which tend to decay by β^- emission to form stable nuclides. The r process, believed to occur during neutron-star mergers and supernovae, is characterized by incredibly high neutron fluxes. The resulting neutron-capture rates are so great that unstable nuclei are much more likely to undergo neutron capture before they have the opportunity to β decay. The s process, which is thought to occur during a star's helium-burning phase, involves neutron fluxes low enough that the time between neutron-capture events is on the order of the β-decay lifetime of the radionuclides produced in this process [13].

The production of ^{187}Os occurs almost entirely by the s process, and ^{187}Re is primarily produced by the r process. ^{186}Re is a branch point in these two processes, and it can decay into ^{186}Os or ^{186}W with a half-life of 3.7186 d, or it can undergo neutron capture to create ^{187}Re [14, 15, 16]. The long-lived ^{186m}Re isomer can be created in the reactions $^{185}\text{Re}(n,\gamma)^{186m}$Re and $^{186g}\text{Re}(\gamma,\gamma')^{186m}$Re, or destroyed in the $^{186m}\text{Re}(\gamma,\gamma')^{186g}$Re reaction, though cross sections for these reactions are not well known. As a result, the role of ^{186m}Re in rhenium and osmium nucleosynthesis is not fully understood, and it could be a source of error in the ^{187}Re/^{187}Os chronometer [17]. This motivation for the study of the level structure above the isomer in ^{186}Re is discussed in greater detail in Chapter III.

1.2.3 Isomer Power Source.

The theoretical energy-storage potential of long-lived nuclear isomers is greater than chemical-energy sources by up to six orders of magnitude, an attractive property for numerous military applications. As technology on the battlefield improves, deployed military forces are in need of increasingly powerful energy sources to run equipment, and portability is very important. This requirement was highlighted in a 2013 report by the Defense Science Board, which recommended that $25 million be allocated to research related to developing a radioisotope power source [18].

The energy densities of nuclear isomers are second only to fissile isotopes, but the means of depleting isomers, or inducing them to release their excess energy on demand, in practical quantities has not yet been demonstrated [19]. If isomer depletion could be reliably achieved, it would likely lead to high-power energy sources much cleaner than nuclear reactors. When an isomer decays by γ-ray cascade to the ground state the energy released does not involve transmutation, so the products are less radioactive than the fission products that constitute the majority of nuclear-reactor waste.

Many nuclear isomers are known, with excitation energies of several eV to several MeV and lifetimes typically ranging from microseconds to thousands of years. However, those with half-lives greater than one year are rare, and at present only 12 are known [20]. It is these long-lived isomers that have the greatest potential for energy storage, and they are the focus of research aimed at demonstrating isomer depletion with a positive energy balance.

All isomers with the exception of ^{180m}Ta are unstable, and they naturally release their excess energy through either β decay or IT. The focus of isomer-depletion research involves exciting the nucleus in the isomer state into a higher-lying state from which it can decay promptly to the ground state, releasing the excitation energy of the isomer in the process. Depletion has been achieved in several experiments involving neutron bombardment and X-ray irradiation of an isomeric target, though in each case more energy was put into the target than was emitted.

The second longest-lived nuclear isomer known, ^{186m}Re, has a $\sim 2.0 \times 10^5$-y half-life and therefore exists as a relatively stable energy storage medium [21]. If ^{186m}Re could be depleted from the isomer to the ^{186}Re ground state, it would then β^- decay with a half-life of 3.7186 d. The resulting energy released would consist of γ rays and/or conversion electrons with energies summing to 148.2 keV from the isomer depletion and β^- electrons from the ground-state decay of ^{186}Re with an endpoint energy of 1.07 MeV [3, 22]. The highly-energetic β^- electrons could generate a usable current in a high-bandgap semiconductor such as SiC, or by sandwiching a scintillator with a photocathode [23].

Isomer depletion through on-resonance photon excitation to a higher-lying state above the isomer has been proposed for experiments designed to investigate the potential of an isomer power source [19]. The higher-energy state in the depletion pathway would need to be connected to the ground state via a cascade of γ rays for spontaneous decay to occur. In the case of ^{186}Re, there are no levels or γ-ray transitions above the isomer in the adopted level scheme, so no such intermediate states are known [3]. Such levels and transitions in ^{186}Re are needed to design future direct-depletion experiments involving tunable high-energy photon sources. The cross sections for photon-induced nuclear excitation and depletion measured in such experiments would be useful for determining the feasibility of constructing an isomer power source with ^{186m}Re.

1.3 Problem

The primary intent of this research was to conduct a thorough examination of the low-energy nuclear level structure of ^{186}Re. At present, the level structure of ^{186}Re is not well known, and the adopted level scheme includes numerous tentative assignments [3]. While the focus of this research effort was on the discovery of new levels and transitions involved in feeding the long-lived ^{186m}Re isomer, the investigations were also useful for validating or revising tentative assignments in the adopted level scheme. A search for states with decay pathways to both the isomer and ^{186}Re ground state was of particular interest, since the energies of these states are important in the design of direct-depletion experiments that could lead to the development of an isomer power source. Secondary to the effort of expanding the nuclear-structure data on ^{186}Re was making independent measurements of the total radiative thermal-neutron capture cross section on ^{185}Re and the ^{186}Re neutron-separation energy. Measurements of reaction cross sections and excited-state energies were compared with the output from theoretical models, as applicable, to validate experimental results.

1.4 Hypothesis

In-beam γ-ray spectroscopic measurements involving the ^{187}Re$(n, 2n\gamma)^{186}$Re, ^{185}Re$(n, \gamma)^{186}$Re, and ^{186}W$(d, 2n\gamma)^{186}$Re reactions could be analyzed to determine valuable new nuclear-structure and reaction data for ^{186}Re. These data would be valuable additions to structure and reaction databases that are used in a variety of nuclear applications.

Specific information about levels and transitions that feed the ^{186m}Re isomer would have direct applications to the problems of assessing the accuracy of the Re/Os cosmochronometer and investigating the potential use of ^{186}Re in an isomer power source.

1.5 Methods

In order to conduct a more complete spectroscopic analysis of ^{186}Re than that described in the existing literature (which has primarily been deduced from studies of ^{185}Re(n, γ) and single-nucleon transfer reactions), multiple experiments involving different reactions had to be performed to measure the γ-ray transitions following production of these excited states. The dynamics of the reactions studied are described in Chapter II. Summaries of the experiments and the methods that were used to analyze the data from these experiments are described in the following paragraphs, and more detailed information about the specific experiments and facilities is contained in Chapters III, IV, and V.

1.5.1 ^{187}Re$(n, 2n\gamma)^{186}$Re Experiment.

The GErmanium Array for Neutron Induced Excitations (GEANIE) γ-ray spectrometer at the Los Alamos Neutron Science Center (LANSCE) was used to obtain γ-ray spectra and production cross-section data from fast-neutron induced reactions on an enriched ^{187}Re metal target. Examination of the data revealed new γ-ray transitions in ^{186}Re and verified transitions and levels previously reported in the literature. Known γ-ray transitions in the neighboring odd-Z, odd-N isotope ^{184}Re, which has a similar structure to that of ^{186}Re, were used to identify and place transitions above the ^{186m}Re isomer. To motivate level spin-parity assignments and the placement of γ-ray transitions in the level scheme, a goodness-of-fit analysis was performed between experimental excitation functions and cross sections calculated with the CoH 3.4 and Talys 1.6 reaction codes.

1.5.2 ^{185}Re$(n, \gamma)^{186}$Re Experiment.

The 10 MW$_t$ Budapest Research Reactor (BRR) at the Budapest Neutron Centre (BNC) was used as a thermal-neutron source for the examination of prompt γ rays produced via neutron capture on ^{185}Re. The Prompt Gamma-ray Activation Analysis (PGAA) apparatus at BNC, which consists of a single Compton-suppressed high-purity germanium (HPGe) detector, was used to measure γ-ray spectra from (n, γ) reactions on an enriched ^{185}Re target. These spectra were analyzed to identify γ-ray transitions reported in the adopted level scheme for ^{186}Re. Gamma-ray production cross sections were derived from peak fits and used in conjunction with the DICEBOX Monte-Carlo statistical-decay code to determine the total thermal-neutron capture cross section σ_0 for ^{185}Re.

1.5.3 ^{186}W$(d, 2n\gamma)^{186}$Re Experiments.

The CAESAR γ-ray spectrometer at the Australian National University (ANU) was used to measure the γ decay of excited states in ^{186}Re populated in ^{186}W$(d, 2n)^{186}$Re reactions. After measuring γ-ray excitation functions for the production of ^{186}Re at different deuteron energies, a beam energy of 14.5 MeV was determined to maximize production of the ^{186m}Re isomer. A short (~1.5 day) run was accomplished at this beam energy, and γ-γ coincidences from this experiment were analyzed to reveal levels and γ-ray transitions not in the evaluated literature.

Because of the limited amount of data taken during the ANU experiment, a second experiment was performed to investigate the same ^{186}W$(d,2n)^{186}$Re reaction at the Research Center for Nuclear Physics (RCNP) at Osaka University, Japan. The RCNP was host to the joint U.S. – Japanese Clover Array Gamma-ray spectrometer at RCNP for Advanced research (CAGRA) project, which was used to measure γ-ray coincidences from the irradiation of an enriched ^{186}W foil with 14.5 MeV deuterons. The resulting γ-γ coincidence matrices and γ-γ-γ cubes were analyzed to confirm the placements of γ-ray transitions in the ^{186}Re level scheme proposed from the analysis of the ANU data set.

II. Theory

Elucidating the level structure of the ^{186}Re nucleus is the ultimate focus of this dissertation research. Because ^{186}Re is an odd-Z, odd-N deformed nucleus, its level scheme is characterized by a particularly high level density at low energies. Using the techniques of in-beam γ-ray spectroscopy, the complex level scheme of this nuclide can be investigated. For the study of ^{186}Re, γ-ray spectra were measured from the following reactions: $^{187}\mathrm{Re}(n,2n)^{186}\mathrm{Re}$, $^{185}\mathrm{Re}(n,\gamma)\mathrm{Re}$, and $^{186}\mathrm{W}(d,2n)^{186}\mathrm{Re}$. The dissertation research thus spans two distinct, albeit related, fields: nuclear structure and nuclear reactions. This chapter will provide a brief overview of common nuclear models and the motivation behind the study of ^{186}Re. The dynamics of nuclear reactions and the reaction-modeling codes employed in the research will be discussed, as well as the physics of nuclear isomers. Experimental data-analysis techniques and systematics that are specific to each of the reactions studied will be discussed in greater detail in the applicable chapters that follow.

2.1 Nuclear Structure

Nuclear-structure physics involves the study of nuclear levels with excitation energies of several MeV and below, and associated electromagnetic transitions. Models describing the motion of protons and neutrons (nucleons) in the nucleus are generally categorized in terms of collective (macroscopic) and microscopic models [24].

2.1.1 The Nuclear Landscape.

Early in the 20th century, patterns in the stability or instability of known nuclides provided clues to understanding nuclear-structure physics. In the Segré chart of the nuclides, a plot showing the known nuclei according to their proton number Z and neutron number N (Figure 1), the stable nuclei emerge in a valley in the center of the chart. When plotted according to the usual convention of Z versus N, the unstable proton-rich isotopes are located to the north of the valley, and the unstable neutron-rich isotopes are south of the valley.

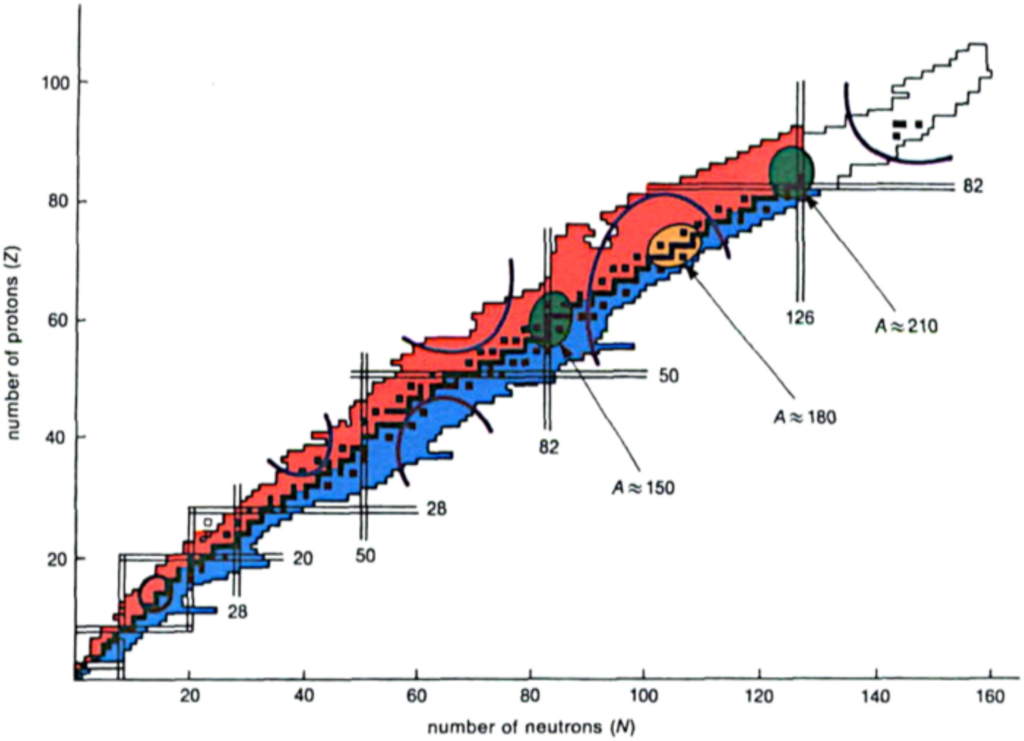

Figure 1. The Segré chart of the nuclides, showing known nuclides plotted with their proton number Z versus neutron number N. The black squares in the central valley of the chart represent the stable nuclei. Blue squares identify nuclei that predominantly decay by β^- emission, and red squares identify those that decay mainly by β^+ emission or electron capture (ε). The double vertical or horizontal lines are the magic numbers predicted by the shell model. Purple arcs enclose regions in which nuclei are commonly deformed, and green- and yellow-highlighted areas refer to locations where nuclear isomers (spin-trap and K-trap, respectively) are generally found. Nuclear deformation and the physics of isomers will be discussed in later sections. Figure copyright 1994, IOP Publishing. Reproduced with permission from [25].

The shape of the valley of stability informed the development of the liquid-drop model (discussed later in this section), the first successful collective, or macroscopic, nuclear model. Nuclei in which neutron or proton numbers are equal to 2, 8, 20, 28, 50, 82, or 126 (referred to as the magic numbers) are known empirically to have greater binding energies than their neighbors, and are therefore especially stable. Efforts to explain this behavior, which is not predicted by collective models, led to the quantum-mechanical shell model of nuclear structure. The magic numbers (with the exceptions of $N, Z = 2$ and $Z = 126$) are identified in Figure 1.

2.1.2 Microscopic Models.

In microscopic models of the nucleus, the nucleons are treated as individual particles rather than collectively. The underlying goal of these models is to solve the Schrödinger equation for the nuclear wavefunction, where the Hamiltonian operator includes the interactions between all Z protons and N neutrons in the nucleus. In practice, this is an n-body problem that requires simplifying assumptions to solve for all but the lightest nuclei [24]. The shell model, which is the most successful model of nuclear structure to date, is one of a number of microscopic models [26].

Shell Model.

The shell model involves a mean-field approximation in which the nuclear potential is assumed to be the spherically symmetric Woods-Saxon potential:

$$V(r) = \frac{-V_0}{1 + \exp[(r - R)/a]}, \tag{1}$$

where $V_0 \approx 50$ MeV, $R = 1.25A^{1/3}$ fm and $a = 0.524$ fm [27]. Solving the Schrödinger equation

$$\hat{H}|\psi\rangle = E|\psi\rangle, \tag{2}$$

for nucleons moving independently in this potential, where

$$\hat{H} = \sum_{i=1}^{Z,N} \left(\frac{-\hbar^2}{2m_i} \nabla_i^2 + V(r_i) \right) \tag{3}$$

is the Hamiltonian operator, results in the set of energy levels ordered as in the left-hand side of Figure 2. When the potential is modified to include the effects of spin-orbit ($\vec{L} \cdot \vec{S}$) coupling, the states with orbital angular momentum $\ell > 0$ split into two distinct energy levels, or orbitals, resulting in the level-energy diagram on the right-hand side of of Figure 2. Orbitals are identified with their quantum numbers n, ℓ, and $j = \ell + s$, where $s, p, d, f, \ldots$ refers to $\ell = 0, 1, 2, 3, \ldots$ The individual-nucleon orbitals determine the overall nuclear spin J and wavefunction parity π, and the method for deducing the ground-state J^π will be discussed in Section 2.1.4.

The shell-model energy levels in Figure 2 emerge in several groupings, termed major shells, and significant gaps appear between shells at Z, N=2, 8, 20, 28, 50, 82, 126, and 184. These shell gaps match the empirical magic numbers exactly up to $Z, N = 82$ and $N = 126$. Furthermore, the shell model predicts that $Z = 126$ and $Z, N = 184$ are magic, although superheavy nuclei with these Z or N have not yet been found in nature or synthesized in the laboratory to confirm these predictions [27]. Minor shell gaps are also observed at $N, Z = 40$ and $Z = 64$ for certain N [26]. These shell gaps are not identified in Figure 2, but their effects are experimentally observable.

The shell model explains why doubly-magic nuclei, those with both Z and N equal to magic numbers, have large energy gaps between the ground state and the first intrinsic excited state (the lowest-energy excited state resulting from an orbital configuration different than that of the ground state, and not from collective, e.g., rotational, motion). Because of the energy gap between shells, a large amount of

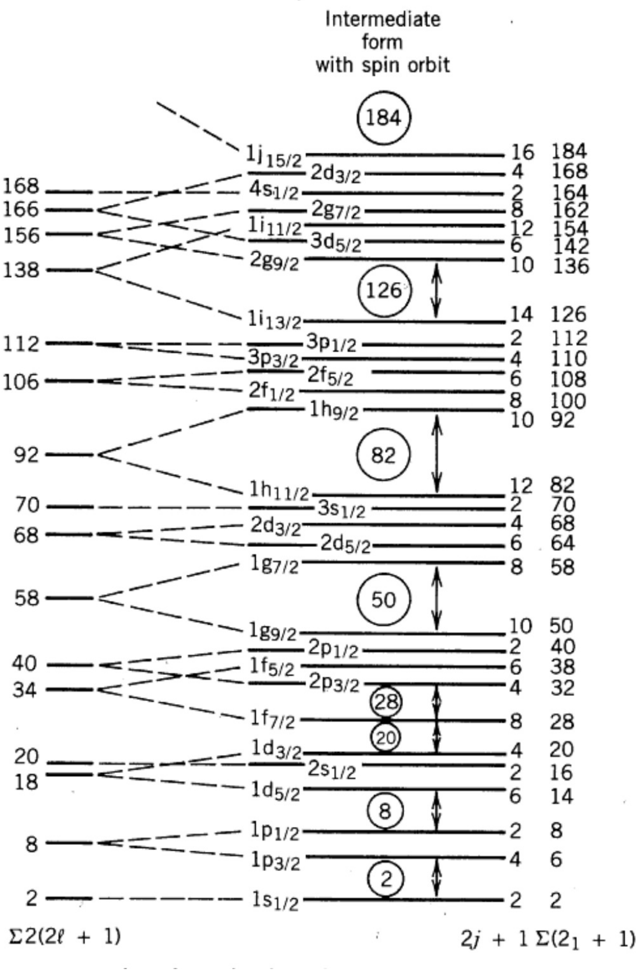

Figure 2. Diagram of energy levels in the shell model, showing the lifting of degeneracy in the $\ell > 0$ states when the spin-orbit interaction is included in the nuclear potential. The capacity of each orbital and the total number of nucleons when each orbital is filled are listed to the right of each level. The magic numbers, which correspond to completely filled shells, are circled. Reproduced with permission from [27].

energy is required to promote a nucleon to an orbital in the next empty shell to create such an excited state.

One major limitation of the shell model arises from the assumption that the potential $V(r)$ in Equation (1) is spherically symmetric. The energy levels predicted by the shell model are therefore not applicable to cases where the nucleus has a non-spherical shape. A modification to the shell model that assumes a deformed potential, known as the Nilsson model, is used to make predictions about deformed nuclei. One such deformed nucleus is the subject of this work, ${}^{186}_{75}\mathrm{Re}_{111}$, which exists between shells ($50 < Z < 82$ and $82 < N < 126$). In this mid-shell region of the chart of the nuclides, highlighted in Figure 1, nuclear deformation contributes to the prevalence of long-lived isomers.

Electromagnetic Transitions and Selection Rules.

Electromagnetic transitions between nuclear states comprise electromagnetic radiation (γ rays) and internal conversion. When a transition proceeds by internal conversion, the nucleus decays by transferring energy to an atomic electron via a virtual photon, which causes the electron to be excited into a different atomic orbital or ejected from the atom. The ratio of the probability P_{IC} of a transition proceeding by internal conversion to the probability P_γ that it results in γ-ray emission is defined as the internal conversion coefficient (ICC): $\alpha = P_{\mathrm{IC}}/P_\gamma$. ICCs are either measured from conversion-electron spectrometry, or they are calculated using theoretical models such as that applied in the Band-Raman Internal Conversion Calculator (BrIcc) code [28, 29].

In general, electromagnetic transitions involve radiation with a characteristic multipolarity XL, and are categorized as electric or magnetic dipoles ($E1$ or $M1$), quadrupoles ($E2$ or $M2$), octupoles ($E3$ or $M3$), etc. Calculations of the matrix elements for transitions between initial states with spin-parity $J_i^{\pi_i}$ to final states with spin-parity $J_f^{\pi_f}$ lead to the following selection rules that identify allowable transition multipolarities:

$$\begin{gathered} |J_i - J_f| \leq L \leq J_i + J_f \\ \pi_i \pi_f = \begin{cases} (-1)^L & \text{for electric transitions} \\ (-1)^{L+1} & \text{for magnetic transitions} \end{cases} \end{gathered} \tag{4}$$

Here J_i and J_f are the angular momentum quantum numbers of the initial and final states, respectively, and L is the multipole order of the electromagnetic transition. The parities of the initial- and final-state wavefunctions, $\pi_{i,f}$, can take on values of +1 (even parity) or -1 (odd parity). The change in parity $\pi_i \pi_f$ between initial and final states determines the electric or magnetic character of the allowed transitions based on their multipole order [26]. When there is no change in parity, even multipoles correspond to electric transitions and odd-multipole transitions are magnetic. The opposite is true when there is a change in parity between the initial and final states.

Weisskopf Estimates.

For given initial and final states, the selection rules defined by Equation (4) permit more than one allowed transition whenever $J_i + J_f > |J_i - J_f|$. In general, of the allowed transitions, the one of lowest multipole order is most likely. Furthermore, transitions with electric character are more likely than those with magnetic character. The relative probabilities of allowed transitions between states are quantified by their transition rates, which can be approximated using the Weisskopf estimates [27].

The Weisskopf estimates are derived by calculating transition-matrix elements assuming transitions between nuclear states are due to a single particle moving in a Woods-Saxon potential [Equation (1)]. Because the Woods-Saxon potential is spherically symmetric, the Weisskopf estimates are only directly applicable to spherical nuclei, and even in these cases the estimated rates are only roughly comparable to measured decay lifetimes [24, 27].

The formulation of the Weisskopf estimates listed below yields transition rates λ in units of s^{-1} given the transition energy E in MeV and the atomic number A. For electric transitions with multipole order up to 5 ($E1$ through $E5$), they are:

$$\begin{aligned}\lambda(E1) &= 1.0 \times 10^{14} A^{2/3} E^{3} \\ \lambda(E2) &= 7.3 \times 10^{7} A^{4/3} E^{5} \\ \lambda(E3) &= 34 A^{2} E^{7} \\ \lambda(E4) &= 1.1 \times 10^{-5} A^{8/3} E^{9} \\ \lambda(E5) &= 2.38 \times 10^{-10} A^{10/3} E^{11}.\end{aligned} \tag{5}$$

The Weisskopf estimates for the rates of $M1$ through $M5$ transitions are:

$$\begin{aligned}\lambda(M1) &= 5.6 \times 10^{13} E^{3} \\ \lambda(M2) &= 3.5 \times 10^{7} A^{2/3} E^{5} \\ \lambda(M3) &= 16 A^{4/3} E^{7} \\ \lambda(M4) &= 4.5 \times 10^{-6} A^{2} E^{9} \\ \lambda(M5) &= 7.29 \times 10^{-13} A^{8/3} E^{11}.\end{aligned} \tag{6}$$

Although the transition rates predicted by the Weisskopf estimates are typically order-of-magnitude approximations to rates obtained from half-life measurements, the estimates reveal some of the systematic behavior governing the lifetimes of nuclear states. For a given A, the transition rate increases with the energy E of the transition as E^{2L+1}, where L is the multipole order of the transition [24, 27]. It follows from the dependence on E that very low-energy transitions are inhibited, a fact confirmed by experiment. However, the dominant term in each of the transition rates listed in Equations (5) and (6) is the leading constant, which decreases by nearly six orders of magnitude each time the multipole order L is incremented. This fact is important for explaining isomer lifetimes, and will be revisited in Section 2.3.

Deformed Shell Model.

The shell model is widely regarded as the most successful model in nuclear-structure physics, with applications ranging from predicting excited-state energy levels to explaining systematic behavior in proton- and neutron-separation energies and neutron-capture cross sections. The predictions of the shell model agree well with experiment when N or Z are in close proximity to the magic numbers, because these nuclei are nearly spherical [26]. The assumption that the nuclear potential is spherically symmetric, however, limits the predictive power of the shell model when the nucleus is known to be spherically asymmetric. Spherical asymmetry is common for nuclei between shell closures, such as those in the mid-shell $150 \leq A \leq 190$ mass range of interest in this work.

In general, for a deformed nucleus, the nuclear radius R is given in terms of the spherical harmonics $Y_{2\mu}(\theta, \phi)$ by the function

$$R = R_0 A^{1/3} \left[1 + \sum_{\mu} \alpha^*_{2\mu} Y_{2\mu}(\theta, \phi) \right], \tag{7}$$

where A is the mass number, $R_0 = 1.25$ fm, and the $\alpha^*_{2\mu}$ are the complex conjugates of the expansion coefficients for the spherical harmonics [24, 26]. For spherical nuclei, $\alpha_{2\mu} = 0$ for all μ, and the formula reduces to $R = R_0 A^{1/3}$.

The most commonly-encountered type of nuclear deformation is quadrupole deformation, in which the nucleus can take on either an oblate (frisbee) or prolate (rugby ball) shape. Deformation can also occur when the nucleus is stretched or compressed along a direction perpendicular to the axis of nuclear symmetry, resulting in axial asymmetry. For a quadrupole-deformed nucleus, the nonzero coefficients in Equation (7) are α_{20} and $\alpha_{2\pm2}$. These coefficients can be written in terms of a parameter β and an angle γ that are more intuitively related to the type and extent of the deformation:

$$\alpha_{20} = \beta \cos\gamma$$
$$\alpha_{2\pm2} = \frac{1}{\sqrt{2}}\beta \sin\gamma. \tag{8}$$

In Equation (8), β specifies the type and degree of static quadrupole deformation ($\beta > 0$ for prolate nuclei, and $\beta < 0$ for oblate nuclei), and $0° \leq \gamma \leq 30°$ corresponds to the degree of axial deformation ($\gamma = 0°$ for an axially-symmetric nucleus, and $\gamma = 30°$ for the maximum degree of axial asymmetry) [24, 26]. The equipotential surfaces defining the shapes of quadrupole-deformed nuclei are shown in Figure 3, in which the effects of varying β and γ are illustrated. Further discussion of nuclear deformation will be focused on axially-symmetric states as they apply to ^{186}Re.

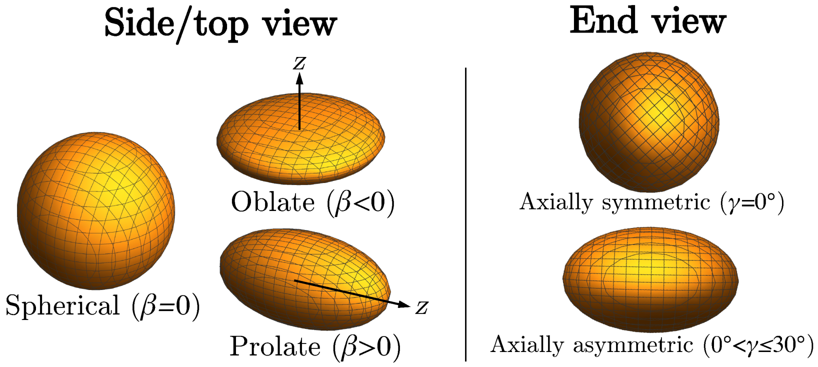

Figure 3. Characteristic shapes of equipotential surfaces in deformed nuclei, with the axis of nuclear symmetry identified as the z axis. The spherical shape has $\beta = 0$, while the oblate and prolate shapes have $\beta < 0$ and $\beta > 0$, respectively. The axial symmetry is a function of $0° \leq \gamma \leq 30°$, and the end views (with the z axis coming out of the page) show different degrees of axial asymmetry for the prolate shape.

The shell model, modified with an axially-symmetric deformed potential, is known as the Nilsson model. In the Nilsson model, the energy levels depend on the degree of deformation ϵ, which is related to the parameter β according to the expression

$$\beta = \sqrt{\pi/5}\left(\frac{4}{3}\epsilon + \frac{4}{9}\epsilon^2 + \frac{4}{27}\epsilon^3 + \frac{4}{81}\epsilon^4 + \ldots\right). \tag{9}$$

The deformation parameter for ^{186}Re is $\beta = 0.221$, which when substituted into Equation (9) yields $\epsilon = 0.20$ [30]. The energy levels that result from solving the Schrödinger equation with an axially-symmetric deformed potential are displayed in neutron- and proton-specific plots such as those of Figure 4. These plots are referred to as Nilsson diagrams [26].

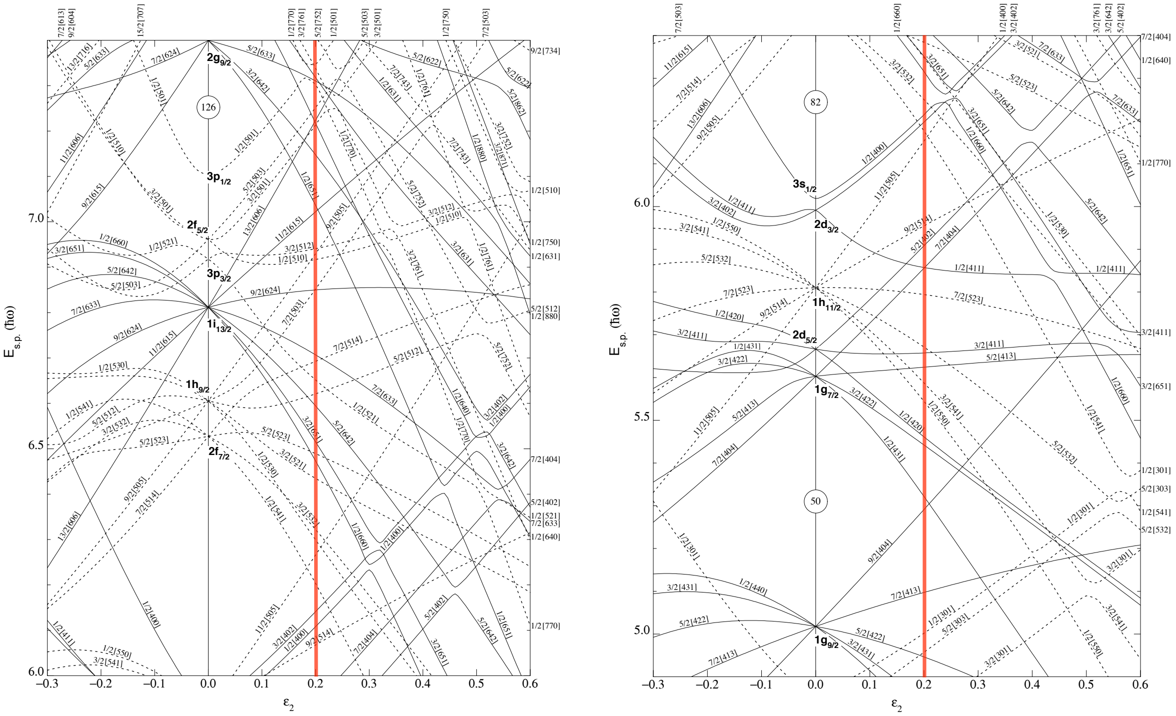

(a) Neutron energy levels

(b) Proton energy levels

Figure 4. Nilsson-model energy-level diagrams for (a) neutrons and (b) protons in nuclei with $82 \leq N \leq 126$ and $50 \leq Z \leq 82$. The degree of deformation ϵ (ϵ_2 in the figure) is negative for oblate nuclei and positive for prolate nuclei. The value $\epsilon = 0.20$ for ^{186}Re is identified in (a) and (b) with a vertical red line. Shell-model energy levels in spherical nuclei are shown along the vertical black line at $\epsilon = 0$, with magic numbers circled. Figure copyright 2009 Wiley-VCH Verlag GmbH & Co. KGaA. Reproduced with permission from [10].

In the Nilsson model, because of collective rotation the magnitude J of the total angular momentum is not a constant of the motion, so J is not a good quantum number. The angular-momentum quantum number used in the Nilsson model is the projection K of the angular-momentum vector on the axis of nuclear symmetry.

The total angular momentum J results from summing the angular momenta of individual valence nucleons, where the single-particle angular momentum is identified with a lowercase j. The projection of the single-particle angular momentum j on the axis of symmetry is defined as Ω, as shown in Figure 5. For a nucleus with two valence nucleons with angular momenta j_1 and j_2, the total angular momentum is $J = j_1 + j_2$, and its projection is $K = \Omega_1 + \Omega_2$.

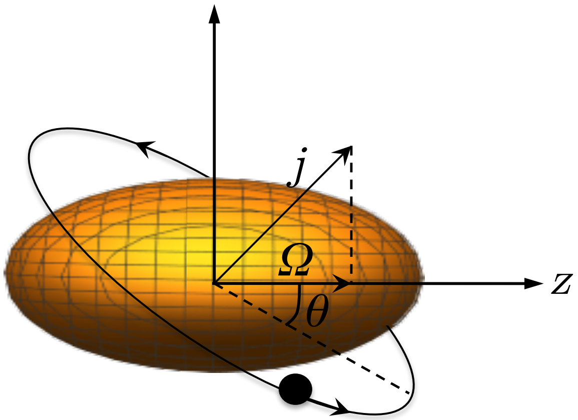

Figure 5. Definition of quantum number Ω for a prolate-deformed nucleus with spin j due to the orbit of a single nucleon. The angle of inclination θ is measured relative to the axis of nuclear symmetry (defined as the z axis).

Discrete single-particle levels in the Nilsson model are labeled according to the convention $\Omega^{\pi}\,[Nn_z\Lambda]$, in which Ω^{π} defines the Ω value of the state and the parity π of the wavefunction, N is the principle quantum number of the major shell, n_z is the number of nodes of the wavefunction in the z direction, and Λ is the projection of the orbital angular momentum on the axis of symmetry [26]. A nucleon with intrinsic spin 1/2 can have a spin projection $\Sigma = \pm 1/2$ on the symmetry axis, so that $\Omega = \Lambda + \Sigma$.

The orbital angular-momentum vector of a single particle orbiting a deformed nucleus can take on distinct inclinations relative to the axis of symmetry. The energy of the single-particle orbit depends on the angle of inclination θ, a quantized value that is related to the average distance between the orbiting nucleon and the rest of the nucleus. For orbits with small θ, the orbiting nucleon remains close to the central nuclear mass throughout its path, so the attractive nature of the strong force causes it to be more tightly bound. Its energy is thus lowered relative to that of a spherical state with the same j value. Conversely, a nucleon in an orbit with large θ (up to 90°) spends the majority of its orbit at a greater distance from the central mass, and its energy is raised relative to the spherical-state energy. Two orbits with the same single-particle angular momentum j but different θ are illustrated in Figure 6.

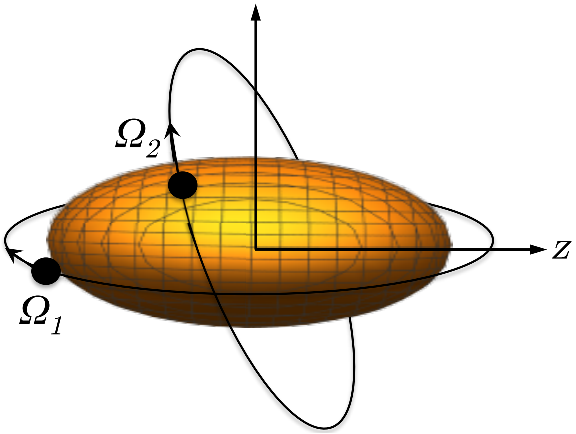

Figure 6. Two single-nucleon orbits about a prolate-deformed nucleus at different angles of inclination relative to the axis of nuclear symmetry, identified as the z axis. The orbit labeled $\mathbf{\Omega_1}$ has a lower energy than the one labeled $\mathbf{\Omega_2}$.

In a spherical nucleus, there is no preferred axis of symmetry, and as a result the energy levels are degenerate in the Ω quantum number. As deformation increases, this degeneracy lifts and the single-particle energy levels split into distinct levels with $\Omega = {}^1/_2, {}^3/_2, ..., j$, with energies raised or lowered based on the angle of inclination of the single-nucleon orbital as described above. This effect is evident in Figure 4.

K-Hindrance.

Because of the assumption of a spherical potential in the derivation of the Weisskopf estimates [Equations (5) and (6)], they are not directly applicable to deformed nuclei. Quantum-mechanical selection rules derived from the Nilsson model require that the multipole order L of a transition be equal to or greater than the difference in K between the initial and final state. This selection rule is not strictly observed, and symmetry breaking can lead to transitions in which $L < \Delta K$, though such transitions are hindered.

The degree of K-hindrance of an electromagnetic transition with $L < \Delta K$ is governed by the value $\nu = \Delta K - L$. A quantity known as the reduced hindrance f_ν is defined by the equation

$$f_\nu = \left(\frac{\lambda^W}{\lambda}\right)^{1/\nu}, \tag{10}$$

where λ is the decay constant, and λ^W is the decay constant from the Weisskopf estimates. The value of f_ν has been shown by Löbner to be approximately 100 for a wide range of possible values for ν and L [31]. *Ceteris paribus*, increasing ΔK by one results in a 100-fold decrease in λ [32].

2.1.3 Collective Models.

In collective models of the nucleus, nuclear properties are modeled without attempting to describe the interactions between individual protons and neutrons. Instead, empirical observations are explained as arising from the average motion of nucleons in the nucleus. Collective models generally attempt to explain the systematics of particular nuclear properties, such as binding energies, masses, and level densities.

Liquid-Drop Model.

Early in the investigation of nuclear structure, attempts to explain nuclear binding energies led to the development of the liquid-drop model by H. Bethe and C. Weizsäcker. Nuclear binding energies (measured in MeV/nucleon), as a function of mass number A, are known to follow a curve that increases rapidly from ^{1}H to ^{12}C, peaks at ^{56}Fe, and then slowly decreases thereafter as A increases. The curve can be fitted by the function

$$B = a_v A - a_s A^{2/3} - a_c Z(Z-1)A^{-1/3} - a_{sym}\frac{(A-2Z)^2}{A} + \delta, \tag{11}$$

where B is the binding energy per nucleon in MeV/u, $a_v = 15.5$ MeV, $a_s = 16.8$ MeV, $a_c = 0.72$ MeV, $a_{sym} = 23$ MeV, and

$$\delta = \begin{cases} -a_p A^{-3/4} & \text{for } N \text{ and } Z \text{ odd} \\ 0 & \text{for } A \text{ odd} \\ +a_p A^{-3/4} & \text{for } N \text{ and } Z \text{ even,} \end{cases} \tag{12}$$

where $a_p = 34$ MeV [27].

Early scattering experiments supported the idea that the nucleus has a constant density, and a volume V proportional to $A^{1/3}$ [27]. Given that $V \propto A^{1/3}$, the first three terms in Equation (11) are seen to represent the mass-energy contained in the volume of the nucleus, adjusted for the surface tension and the Coulomb repulsion of the protons. This naturally led to the idea that the nucleus could be modeled as a charged droplet of liquid. Adjustments are generally made to improve the accuracy of the liquid-drop model by accounting for a tendency towards equal numbers of neutrons and protons in the nucleus, and for neutrons and protons to pair together [the terms containing the a_{sym} component and δ in Equation (11)]. When these adjustments are incorporated, the model's predictions of nuclear masses and neutron- and proton-separation energies show good agreement with experiment [24].

Bohr-Mottelson Model.

Analogous to the effects observed in visible or infrared spectra described by molecular vibration and rotation, γ-ray spectra also have features explainable by the bulk motion of nucleons in the nucleus. Nuclear excitations resulting from collective nuclear vibration and rotation form the foundation upon which A. Bohr and B. Mottelson developed their model of the nucleus in the 1950s [33].

Prompt γ-ray spectra from reactions involving large transfers of angular momentum to a target nucleus reveal clear patterns in discrete-level energies that follow the $E \propto J(J+1)$ energy dependence of the quantum rigid rotor. This behavior supports the idea that a deformed nucleus can rotate collectively about an axis perpendicular to the axis of symmetry. Collective rotational motion in deformed nuclei can lead to mixing between different-K states, an effect that is attributed to the Coriolis effect, which tends to align the angular momentum vector with the axis of rotation [26].

In addition to rotational excitations, the nucleus can also be excited into vibrational modes. Vibrational modes of excitation involve collective motion in the β or γ degrees of freedom introduced in Section 2.1.2. A β vibration occurs when the nucleus extends and contracts along the axis of symmetry, such that the deformation parameter β oscillates about some mean value. In a γ vibration, the nucleus extends and contracts along an axis perpendicular to the axis of symmetry, and the degree of axial asymmetry given by the angle γ oscillates [24, 26]. The β and γ vibrational modes are illustrated in Figure 7.

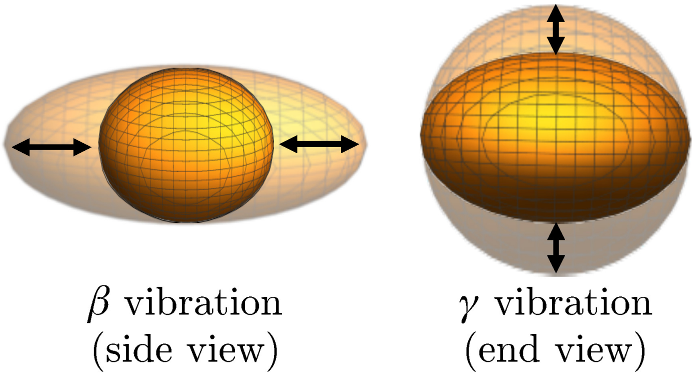

Figure 7. Collective vibrations of a nucleus in the β and γ degrees of freedom. A β vibration extends and contracts the nucleus along its symmetry axis, and a γ vibration is described by a periodic variation in axial asymmetry.

Other Models.

Two other collective models of the nucleus deserve mention here, although they will be explained in greater detail in Chapter IV. The Fermi gas model can be used to calculate the average kinetic energy of nucleons. Additionally, it has been used to derive the symmetry term in Equation (11) from first principles [24]. In the Fermi gas model, the nucleus is approximated as a gas of noninteracting fermions, and from this assumption the total kinetic energy is calculated. The particular application of the model used in this work (Chapter IV) further assumes the gas has two components (protons and neutrons), and it incorporates an energy backshift and spin-dependent term to better fit experimental level-density data. An alternative to the backshifted Fermi gas model is the constant-temperature model, also described in Chapter IV, in which a constant nuclear temperature is assumed to derive level densities as a function of excitation energy.

2.1.4 Combined Models.

The predictive power of the models introduced above to describe nuclear properties and behavior is enhanced when collective and microscopic models are combined. In general, most combined models incorporate a core-plus-valence-nucleons description of the nucleus to make predictions about nuclei away from the magic numbers [24].

Independent Particle Approximation.

In the independent particle approximation, it is assumed that the motion of unpaired valence nucleons (often called quasiparticles) are responsible for observed nuclear properties. Without such an approximation, it would be very difficult to apply the results of microscopic models to all but the nuclei with N or Z immediately adjacent to the magic numbers [26].

To apply the independent particle approximation, shell-model orbitals are filled according to the Pauli exclusion principle, where the capacity of each orbital is a function of the ℓ quantum number. Protons and neutrons tend to pair to create zero-total angular momentum ($J = L + S$) states, a consequence of which is the fact that all even-Z, even-N nuclei have $J = 0$ in the ground state. One can apply this pairing property to predict the spin and parity J^{π} of ground-state nuclear wavefunctions in odd-Z and/or odd-N nuclei. By filling orbitals sequentially as they appear in the shell-model diagram of Figure 2, the remaining unpaired proton and/or neutron will have the spin j and parity $\pi = (-1)^{\ell}$ from its orbital assignment (although residual interactions affect the accuracy of this methodology in practice). The spin J of the nuclear ground state becomes a vector sum of the angular momenta j_p, j_n of the unpaired proton and/or neutron, and the parity π is the product of the parities π_p, π_n of the unpaired nucleons [27]. Intrinsic excited states are created by promoting an unpaired nucleon to a higher-lying orbital, or by breaking a pair and promoting one or both nucleons to higher-lying orbitals. A similar technique is applied to deduce intrinsic-state spins and parities in deformed nuclei from the single-particle Nilsson orbitals.

A direct consequence of the requirement to break a pair of nucleons to create an intrinsic excited state in an even-Z, even-N nucleus is the fact that these nuclei typically have high-energy first excited states (excluding collective rotational excitations) and low level densities. By comparison, in nuclei with odd Z or N, no energy is required to break a pair before promoting the valence nucleon(s) to higher-lying orbital(s), so intrinsic excited states occur at comparatively much lower energies. Because of this fact, nuclei with odd Z or N have relatively high level densities at low excitation energies [27].

The independent particle approximation, although quite useful for explaining general nuclear properties, is ultimately an oversimplification. Some properties, such as configuration mixing, can be explained only when nucleon-nucleon interactions are included in nuclear models. Nucleon-nucleon interactions are accounted for in mean-field solutions to the Schrödinger equation by including a residual-interaction perturbation term in the Hamiltonian [26]. Residual interactions, of which nucleon-nucleon pairing is dominant, shift the energies of multi-quasiparticle configurations. A number of models are used to explain the pairing interaction, including an application of the Bardeen-Cooper-Schrieffer (BCS) theory commonly used to explain superconductivity [24]. The effects of residual interactions on the Nilsson-model energy levels for two-quasiparticle states in ^{186}Re will be discussed in Chapter V.

Types of Nuclear Excitations.

The rotational and vibrational excitations characteristic of the Bohr-Mottelson model are distinct from the intrinsic excitations predicted by the shell or Nilsson models. Intrinsic excitations are the result of the promotion of one or more nucleons to higher-energy orbitals, and collective excitations can occur in conjunction with any intrinsic state to further increase the excitation energy of the nucleus. The experimental level schemes of most nuclei reveal bands of rotationally-excited states built on distinct intrinsic excited states. Transitions within rotational bands are generally unhindered, while those connecting different rotational bands can often be inhibited by differences in the J and K quantum numbers, or by differences in the configurations of the states upon which the bands are built. In mid-shell deformed nuclei with odd Z and odd N, such as the ^{186}Re nucleus studied in this work, the accuracy of theoretical predictions is generally limited by the complexity and number of possible interactions involved. Experimental data are the most important source of information about the discrete levels and transitions in these nuclei.

Gyromagnetic Factors.

In the rotational model, the presence of the positively-charged protons implies that the nucleus is a rotating charged body, and it must therefore have a magnetic moment. The total nuclear magnetic moment μ is due to the collective rotation of the core and the motion of the unpaired valence nucleons , and it can be written as

$$\mu = \left[g_R J + (g_K - g_R) \frac{K^2}{J+1} \right] \mu_N. \tag{13}$$

Here, J and K are defined as in Section 2.1.2, and $\mu_N = \frac{e\hbar}{2m_pc}$ (where m_p is the rest mass of the proton) is the nuclear magneton. The gyromagnetic factors g_R and g_K are related to the contributions of the nuclear core and valence nucleons, respectively, to the overall magnetic moment [34, 35].

The rotational g-factor g_R is related to the charge-carrying capacity of a uniformly-rotating body, and in a simple model in which the protons are assumed to be uniformly distributed throughout the nucleus, it is given by $g_R = Z/A$ [33, 34]. Experimental measurements of magnetic moments for $A \approx 180$ nuclei have shown that this approximation overestimates the true value of g_R, so a quenched value $g_R = 0.7 \times Z/A$ is typically used instead [36]. The intrinsic g-factor g_K depends on the coupling of single-quasiparticle orbital and spin angular momenta, and values for the g_K are generally deduced from empirical measurements of magnetic moments [34].

In γ-ray spectroscopy, the absolute value of the difference $|g_K - g_R|$ can be determined from experimentally-measured transition energies and γ-ray branching ratios, and this difference should be constant for a particular rotational band. Because of the dependence of the g_K on the orbital configuration, measured $|g_K - g_R|$ values can be compared with calculated quantities to motivate multi-quasiparticle Nilsson-model configurations for intrinsic excited states [37, 38, 39, 40]. This type of analysis is discussed in greater detail in Chapter V.

2.2 Nuclear Reactions

Nuclear reactions are the primary experimental means by which nuclear structure is studied. A nuclear reaction, commonly written

$$a + \mathrm{X} \rightarrow \mathrm{Y} + b, \tag{14}$$

where a is the projectile, X is the target nucleus, Y is the residual nucleus and b is the outgoing particle, is routinely abbreviated X(a, b)Y. The specific conditions of the reaction products Y and b, including excited states, define the reaction channel. Certain reaction channels may be closed if the incident particle does not have enough energy or angular momentum to generate a particular final configuration [27].

Nuclear-reaction models are typically categorized as direct and compound models, the latter of which involves the creation of a compound nucleus C^*, written

$$a + \mathrm{X} \rightarrow \mathrm{C}^* \rightarrow \mathrm{Y} + b. \tag{15}$$

The primary difference between direct and compound reactions is the time scale of the reaction: for direct reactions, the time scale is on the order of the time it takes for the incident particle to transit the target nucleus, $\mathcal{O}(10^{-22}\ \mathrm{s})$. Reactions involving a compound nucleus, by contrast, occur on time scales $\mathcal{O}(10^{-16}\ \mathrm{s})$ [27, 41].

It is important to note that nuclear reactions are not in reality separated neatly into direct and compound reactions. In low-energy regimes where incident-particle energies are less than approximately 10 MeV/nucleon, the accessible reaction channels are typically dominated by compound reactions, while at higher energies direct reactions become the primary mechanism. However, at all energies greater than the threshold energy of the reaction, most reactions will progress by some combination of direct and compound mechanisms [27]. As a result, the reaction codes TALYS 1.6 and CoH 3.4 discussed in Section 2.2.4 implement both models to compute theoretical cross sections.

The three reactions studied in this work, described in Chapter I, are predominantly compound-nucleus reactions. The choice to study three reactions that resulted in the same product nucleus was motivated by the fact that each reaction preferentially produces excited states in $^{186}\mathrm{Re}$ with different J^π assignments. A schematic of the regions in the level scheme populated in the $^{187}\mathrm{Re}(n,2n)$, $^{185}\mathrm{Re}(n,\gamma)$, and $^{186}\mathrm{W}(d,2n)$ reactions studied in this work is shown in Figure 8. In the figure, the states populated in each reaction are highlighted relative to the yrast line, defined as the locus of nuclear excited states with the lowest energy for a given spin assignment [26]. Following production, excited states can

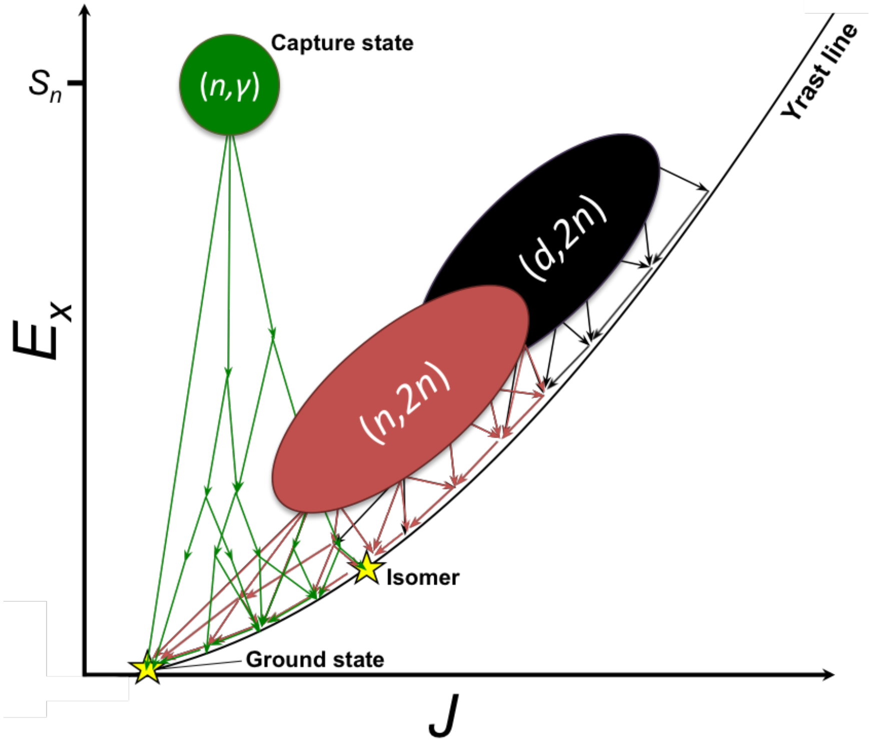

Figure 8. Schematic plot of ^{186}Re excited states populated in ^{185}Re(n,γ), ^{187}Re($n,2n$), and ^{186}W($d,2n$) reactions, and γ rays emitted during their decay. In the figure, excitation energy E_x is plotted against the spin J for the populated states. All excited states in ^{186}Re lie above the yrast line, defined in the text.

decay via a number of possible γ-ray cascades, but the population of certain excited states is ultimately governed by the amount of angular momentum imparted to the compound nucleus by the projectile in each reaction. The thermal neutrons incident on the target nuclei in the (n,γ) reaction have negligible kinetic energy and zero orbital angular momentum, so neutron capture results in low-spin states at high excitation energy. Because the incident neutrons and deuterons in the $(n,2n)$ and $(d,2n)$ reactions have more kinetic energy, they generate excited ^{186}Re nuclei at comparatively higher spins but lower excitation energies. In (n,γ) reactions, the γ-ray cascade following decay of compound nucleus can lead to higher-spin states, but this is less likely than in the case of the other two reactions in which the compound nucleus has a higher initial spin. Therefore, the $(n,2n)$ and $(d,2n)$

reactions were expected to yield more information about excited states and γ-ray transitions feeding the $J^\pi = (8^+)$ isomer in ^{186}Re than the (n,γ) reaction.

2.2.1 Reaction Energetics.

Conservation of mass energy in a nuclear reaction X(a,b)Y leads to the reaction Q value, defined as the difference in mass energy mc^2 between the exit- and entrance-channel particles:

$$Q = (m_\mathrm{X} + m_a - m_\mathrm{Y} - m_b)c^2. \tag{16}$$

Radiative-capture (n,γ) reactions have positive Q values, and are therefore energetically possible on any nucleus (except ^{4}He) at any incident neutron energy [42].

The $(n,2n)$ and $(d,2n)$ reactions studied in this work are both endothermic reactions, with $Q < 0$. There is a minimum, or threshold kinetic energy T_th, the projectile a must have in order to make the reaction energetically possible. This threshold energy is calculated from conservation of linear momentum to be

$$T_\mathrm{th} = -Q\frac{m_\mathrm{Y} + m_b}{m_\mathrm{Y} + m_b - m_a}. \tag{17}$$

The threshold kinetic energy is slightly greater than the reaction Q value. In order to populate an excited state in the product nucleus with an excitation energy E_x, the value Q in Equation (17) must be replaced by $(Q - E_x)$ [27].

(n,γ) Reaction Energetics.

The energy required to separate a neutron from the nucleus is defined as the neutron-separation energy S_n, which is equal to the binding energy of the last neutron. It is given for the nucleus ${}^{A}_{Z}\mathrm{X}_N$ as

$$S_n = \left[m\left({}^{A-1}_{Z}\mathrm{X}_{N-1}\right) - m\left({}^{A}_{Z}\mathrm{X}_N\right) + m\left({}^{1}_{0}n\right)\right]c^2. \tag{18}$$

Comparison of Equation (18) with Equation (16) shows that for slow-neutron capture on a nucleus ${}^{A}_{Z}\mathrm{X}_N$ (when the kinetic energy T of the neutron is negligible), the Q value is equal to the neutron-separation energy S_n for the isotope ${}^{A+1}_{Z}\mathrm{X}_{N+1}$. Upon capture, this energy is made available to the compound nucleus as excitation energy, and is released via γ-ray cascade. For the ${}^{185}\mathrm{Re}(n,\gamma){}^{186}\mathrm{Re}$ reaction, the Q value is equal to $S_n = 6179.59(5)$ keV [43]. Following capture, the compound nucleus proceeds towards thermal equilibrium, and the probability of a single nucleon attaining enough energy to escape from the nucleus, or evaporate, is negligible. The only likely decay channel available is therefore γ-ray emission [8].

The excitation energy of the capture state, and therefore the neutron-separation energy can be determined from the measured prompt γ-ray energies emitted following capture. The energies E_t of transitions between levels can be determined by correcting the measured γ-ray energies E_γ for the nuclear recoil energy E_R:

$$E_t = E_\gamma + E_R = E_\gamma + \frac{E_\gamma^2}{2m_{\mathrm{nuc}}c^2}, \tag{19}$$

where m_{nuc} is the rest mass of the product nucleus [42]. Primary γ-ray transitions, which directly feed low-energy levels from the capture state, are identified by the binding-energy test. If a recoil-corrected transition with energy $E_t = E_\gamma + E_R$ is expected to feed a known level with excitation energy E_x^{lit}, and S_n^{lit} is the literature value of the neutron-separation energy, then the binding energy test involves the comparison

$$E_t \overset{?}{=} S_n^{\mathrm{lit}} - E_x^{\mathrm{lit}}, \tag{20}$$

up to experimental uncertainty. After primary transitions are identified using the binding-energy test, averaging over the sum of primary-transition energies with known excitation energies of the discrete levels they feed can be used to obtain a measurement of the neutron-separation energy S_n for the product nucleus.

(n, xn) Reaction Energetics.

Neutron-induced (n, xn) reactions have energy thresholds governed by the binding energy of the compound nucleus. It is apparent from Equation (16) that the Q value of the $^{187}\text{Re}(n, n')^{187}\text{Re}$ reaction is equal to zero, so the excitation energy of the product nucleus can only result from a difference in the kinetic energies of the incident and emitted neutrons. Using the adopted mass values from Reference [44], Equation (17) gives a reaction threshold energy for the $^{187}\text{Re}(n, 2n)^{186}\text{Re}$ reaction of $T_{\text{th}} = 7.399$ MeV. Likewise, the $^{187}\text{Re}(n, 3n)^{185}\text{Re}$ reaction has a threshold energy of $T_{\text{th}} = 13.612$ MeV.

The probabilities of decay of the compound nucleus via different reaction channels affect the reaction cross sections. The cross sections for the $^{187}\text{Re}(n, xn)^{188-x}\text{Re}$ reactions $(1 \leq x \leq 3)$ are plotted in Figure 9 using data obtained from the ENDF. Because of a lack of experimental data for neutron-induced reactions on ^{187}Re, the cross-section data adopted for the most recent ENDF database, ENDF-VII.1, consist of values calculated with the TALYS 1.2 nuclear reaction code [9]. Above the threshold energy of 7.399 MeV for the $(n, 2n)$ reaction, the cross section for the $^{187}\text{Re}(n, n')^{187}\text{Re}$ reaction decreases as the $^{187}\text{Re}(n, 2n)^{186}\text{Re}$ reaction becomes energetically possible. Similarly, the cross section for the $^{187}\text{Re}(n, 2n)^{186}\text{Re}$ reaction decreases and that of the $^{187}\text{Re}(n, 3n)^{185}\text{Re}$ reaction increases above the $(n, 3n)$ threshold energy of 13.612 MeV. It is therefore possible to apply selection thresholds, or cuts, at

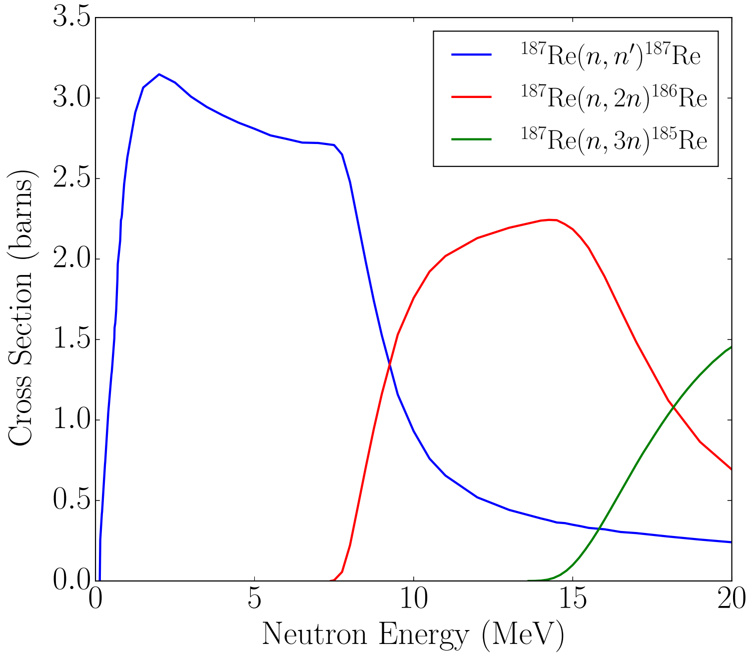

Figure 9. Modeled cross sections for (n, n'), $(n, 2n)$, and $(n, 3n)$ reactions on ^{187}Re, plotted against neutron energy E_n. For $E_n > 1$ MeV the cross section for radiative capture (n, γ) is negligible compared to the reactions shown. Data for this plot were obtained from the ENDF [9, 45].

neutron energies of ∼10 MeV and ∼18 MeV to separate the reaction products by channel during experimental data analysis.

$(d, 2n)$ Reaction Energetics.

A plot of the experimental and TALYS-modeled excitation functions for the $^{\mathrm{nat}}\mathrm{W}(d, xn)^{186g}\mathrm{Re}$ reaction reveal an apparent threshold energy of 7 MeV (Figure 10). Tungsten has no stable isotopes with $A > 186$, so the ^{186}Re yield from deuteron irradiation of natural tungsten is due entirely to the reaction $^{186}\mathrm{W}(d, 2n)^{186}\mathrm{Re}$. Application of Equation (17) with masses from Reference [44] gives a threshold energy of $T_{\mathrm{th}} = 3.626$ MeV for the $^{186}\mathrm{W}(d, 2n)^{186}\mathrm{Re}$ reaction. The difference in values between the calculated threshold energy and that apparent from Figure 10 is due to the fact that the $(d, 2n)$ reaction is induced by the deuteron, a charged particle, and the projectile must have additional kinetic energy to overcome the Coulomb barrier of the target ^{186}W nucleus.

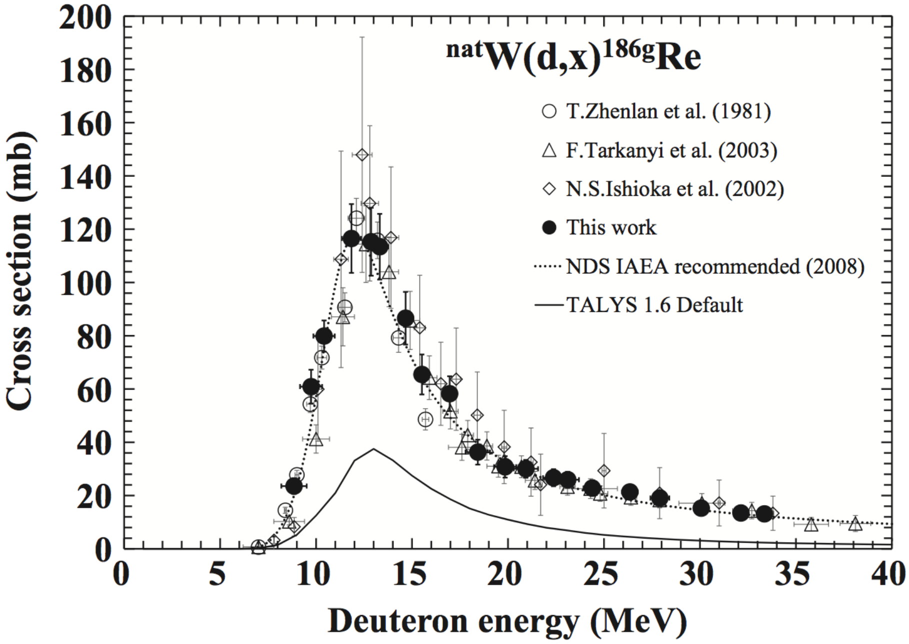

Figure 10. Experimental and modeled cross sections for (d, xn) reactions on ^{nat}W resulting in the production of ground-state ^{186}Re, plotted against deuteron energy up to 40 MeV. The ground state ^{186g}Re yield (excluding the isomer ^{186m}Re) is due entirely to the $^{186}W(d, 2n)^{186g}$Re reaction channel. Reprinted from Reference [7] with permission from Elsevier.

The $(d, 2n)$ reactions described in Chapter V were initiated with monoenergetic 12.5-MeV and 14.5-MeV deuterons on an enriched ^{186}W target. These energies were selected on the basis that they provide an optimum balance between maximizing the yield of ^{186}Re while minimizing the contributions from other reaction channels.

2.2.2 Direct Reactions.

Direct reactions are characterized by the fact that they involve few nucleons, and only a small number of degrees of freedom in the nucleus are excited. Some examples of direct reactions include elastic (Rutherford) scattering and single-nucleon pickup or stripping reactions such as (p, d) or (d, p). Reaction channels for direct reactions typically open at energies higher than those of compound-nucleus reactions.

The reactions and energy regimes considered in this work suggest that direct reactions play a less significant role than do compound-nucleus reactions, and as a result, this chapter will be primarily focused on reactions involving a compound nucleus. However, the optical model is incorporated into the reaction codes used in this research, so it will be briefly discussed.

Optical Model.

In the optical model, the projectile is represented by a wave, which scatters off a complex potential $U(r) = V(r) + iW(r)$, where $V(r)$ and $W(r)$ are real-valued functions. The real and imaginary parts $V(r)$ and $W(r)$ of the potential account for elastic scattering and absorption, respectively. In the simplest application of the optical model, the potential can be represented as a square well or in terms of the Woods-Saxon potential defined in Equation (1). Applications of the optical model in modern reaction codes such as Talys 1.6 and CoH 3.4 involve much more complex potentials that produce better fits to experimental cross-section data.

Given a potential, the wave function for the incoming particle is taken to be a plane wave $\psi(r) = e^{ikr}$, while that of the outgoing particle is a spherical wave $\psi(r) = e^{ikr}/r$. Solving the Schrödinger equation and equating boundary conditions at the nuclear radius permits one to determine the scattered-wave amplitude for the purpose of evaluating transmission and reflection coefficients. These coefficients are related to the average cross sections for absorption and reflection [27].

2.2.3 Compound-Nucleus Reactions.

In a compound-nucleus reaction, the projectile is captured by the target nucleus, forming a compound nucleus that decays via particle and/or γ-ray emission. These reactions, which include (n, γ), $(n, 2n)$, and $(d, 2n)$, involve many degrees of freedom in the nucleus and may include the excitation of all nucleons. After the projectile interacts with the nucleus, the compound nucleus proceeds towards a state of thermal equilibrium. The time scale of the reaction is therefore on the order of the equilibration time of the nucleus, which is $10^{-18} - 10^{-16}$ s [41]. On the time scale of equilibration, statistical fluctuations in the nucleon energies can result in one or more nucleons achieving enough energy to escape the nucleus. This so-called evaporative effect is highly dependent on incident-particle energy. The more energy the projectile imparts to the compound nucleus, the greater the chances of additional nucleon evaporation (evident in the plot shown in Figure 9).

Extreme Statistical Model.

N. Bohr postulated in 1936 that the mode of formation of a compound nucleus and its mode of decay are independent processes [46]. The mode of decay depends only on the energy, angular momentum, and parity of the compound nucleus C^*, and not on the specific way it was produced [47]. Because of the long time scales of compound-nucleus reactions compared to direct reactions, the compound nucleus, as it approaches thermal equilibrium, essentially forgets the means by which it was formed. This assumption forms the basis of the extreme statistical model, which is applied in the DICEBOX code and the Hauser-Feshbach formalism used in the TALYS 1.6 and COH 3.4 reaction codes described in Section 2.2.4.

Resonances.

Compound-nucleus reactions can proceed through quasi-bound states, which are discrete states similar to those involved in a direct reaction. These states have high probabilities of formation, and their energies correspond to the energies of resonances in reaction cross sections. According to the energy-time version of

Heisenberg's uncertainty principle ($\Delta E = \Gamma = \hbar/\tau$) the lifetimes $\tau \sim 10^{-16} - 10^{-18}$ s of compound nuclei result in energy widths $\Gamma \sim 1$ eV $-$ 1 keV of resonance peaks in the excitation functions [41]. These resonance widths become important when populating states where the Q value of the reaction plus the projectile energy equals the excitation energy of the excited state to within $\pm\Gamma/2$. For a resonant reaction progressing from an entrance channel with partial width of formation Γ_α to an exit channel with partial width of decay Γ_β, the cross section is given by the Breit-Wigner formula

$$\sigma(E) = \frac{\pi}{k^2} g \frac{\Gamma_\alpha \Gamma_\beta}{(E - E_R)^2 + \Gamma^2/4}, \tag{21}$$

where E is the energy of the incident particle, $k = p/\hbar$ is the wave number of the center-of-mass system, E_R is the resonant energy, and $\Gamma = \sum_i \Gamma_i$ is the sum over the partial widths of all the ways the compound nucleus can decay after formation. Note that Equation (21) defines a Lorentzian shape for the resonant cross section. The coefficient g is a statistical weighting factor to account for the angular momentum and spin of the system,

$$g = \frac{2J + 1}{(2i + 1)(2I + 1)}, \tag{22}$$

where i and I are the spins of the projectile and target, and J is the total angular momentum (orbital and intrinsic spin) of the resonance [27, 41].

Hauser-Feshbach Model.

In the extreme statistical model of compound-nucleus reactions, the assumption that formation and decay are independent processes implies that the cross section for a reaction to proceed via a specific formation (subscript α) and decay (subscript

β) channel can be factored as

$$\sigma_{\alpha\beta} = \sigma_{\alpha}^{\mathrm{CN}} P_{\beta}, \tag{23}$$

where $\sigma_{\alpha}^{\mathrm{CN}}$ is the cross section for formation of the compound nucleus and P_{β} is the probability that the reaction will proceed via decay mode β, given by

$$P_{\beta} = \frac{\Gamma_{\beta}}{\sum_{\mathrm{all}\ \beta} \Gamma_{\beta}}. \tag{24}$$

In reaction codes that incorporate the Hauser-Feshbach model, the cross sections for formation $\sigma_{\alpha}^{\mathrm{CN}}$ are related to an optical transmission coefficient T_{α} determined using the optical model:

$$\sigma_{\alpha}^{\mathrm{CN}} = \frac{\pi}{k^2} g T_{\alpha}, \tag{25}$$

where k and g are defined as in Equations (21) and (22) [41]. Assuming for now that the particles and resonances all have spin zero, then $g = 1$, and the cross section $\sigma_{\alpha\beta}$ becomes

$$\sigma_{\alpha\beta} = \frac{\pi}{k_{\alpha}^2} T_{\alpha} P_{\beta}. \tag{26}$$

The principle of detailed balance (reversible processes) states that the cross sections for the reaction and its inverse must be related by

$$\sigma_{\alpha\beta} k_{\alpha}^2 = \sigma_{\beta\alpha} k_{\beta}^2, \tag{27}$$

so that

$$\frac{P_{\alpha}}{T_{\alpha}} = \frac{P_{\beta}}{T_{\beta}} \equiv \lambda = \mathrm{const}. \tag{28}$$

Since the sum of the probabilities of all possible decay or formation modes must be equal to one,

$$\sum_{\beta} P_{\beta} = \lambda \sum_{\beta} T_{\beta} = 1 = \sum_{\alpha} P_{\alpha}, \tag{29}$$

λ becomes

$$\lambda = \frac{1}{\sum_\gamma T_\gamma}, \tag{30}$$

where γ is a dummy variable signifying any mode of either formation or decay. The probability of the reaction proceeding via a specific decay mode β is then

$$P_\beta = \lambda T_\beta = \frac{T_\beta}{\sum_\gamma T_\gamma}. \tag{31}$$

The Hauser-Feshbach cross section $\sigma^{\mathrm{HF}}_{\alpha\beta}$ for the reaction is defined for spin-zero particles and resonances as the average

$$\sigma^{\mathrm{HF}}_{\alpha\beta} = \langle \sigma^{\mathrm{CN}}_{\alpha\beta} \rangle = \frac{\pi}{k_\alpha^2} \cdot \frac{T_\alpha T_\beta}{\sum_\gamma T_\gamma}. \tag{32}$$

Incorporating spin requires a summation over all possible spin-parities J^π of the compound nucleus,

$$\sigma^{\mathrm{HF}}_{\alpha\beta} = \langle \sigma^{\mathrm{CN}}_{\alpha\beta} \rangle = \frac{\pi}{k_\alpha^2} \cdot \sum_{J,\pi} \frac{2J+1}{(2i+1)(2I+1)} \cdot \frac{T_\alpha T_\beta}{\sum_\gamma T_\gamma}, \tag{33}$$

where i and I are the spins of the projectile and target, respectively [41]. The Hauser-Feshbach reaction model tends to overestimate the cross sections when compared to experimental data because of an underlying assumption made in applying the optical model to evaluate the transmission coefficients. This assumption is that resonance cross sections are equal to their peak values given by the Breit-Wigner formula [Equation (21)]. As a result, Equation (33) is sometimes modified to include a scaling coefficient $\eta < 1$ to correct for the overestimation [13].

The reaction code TALYS 1.6 and COH 3.4 both compute Hauser-Feshbach cross sections for compound-nucleus reactions. To average over the σ^{CN}, these codes utilize discrete-level information from RIPL below a user-defined energy cutoff E_c

and semi-empirical models of nuclear level densities above E_c [48, 49]. Both codes derive the transmission coefficients T_γ from an application of the optical model.

2.2.4 Reaction Codes.

The reaction codes used in this work are TALYS 1.6, CoH 3.4, and DICEBOX, each of which is capable of computing theoretical cross sections for different reaction types given discrete-level information about the nuclei involved. Both TALYS 1.6 and CoH 3.4 incorporate an optical model and Hauser-Feshbach statistical calculations, as well as a pre-equilibrium exciton model to cover reactions that progress through a compound state that has not reached thermal equilibrium. DICEBOX is a statistical-decay code that performs a Monte-Carlo simulation of γ-ray cascades following neutron capture for the purpose of computing (n, γ) reaction cross sections.

TALYS 1.6.

The TALYS program is a FORTRAN-based code that models nuclear reactions in mid- to high-Z elements in the 1 keV – 200 MeV energy range. Cross sections are calculated in TALYS using a Monte-Carlo algorithm that employs the Hauser-Feshbach statistical model. TALYS was developed by a European collaboration, and it has a large international user group due to the fact that it can generate cross sections and Q values for reactions on unstable nuclei for which there is little experimental data available. TALYS is also commonly used to validate experimental cross-section measurements. The program is remarkably flexible, and it permits the user to modify an input deck to adjust the specific reaction models and parameters used in the statistical calculations [49].

CoH 3.4.

CoH is a C++ code developed at LANSCE as an update to an earlier (pre-2008) FORTRAN-based code known as GNASH. Both CoH and GNASH calculate cross sections for reactions on mid- to high-Z elements using a combination of optical and Hauser-Feshbach models. For neutron-induced reactions, CoH can output differential partial γ-ray cross sections for neutrons above 1 keV, which was useful for validating the results of the $^{187}\mathrm{Re}(n, 2n\gamma)$ measurements made in this work. CoH differs from TALYS mainly in the specific choices of optical-model potentials used in the calculations [48, 50].

DICEBOX.

Dicebox is a FORTRAN-based Monte-Carlo code for simulating the statistical cascade of γ rays following cold- or thermal-neutron capture. Dicebox comes with a library of PYTHON scripts that automate building the input deck required by the FORTRAN routines. Other PYTHON scripts can be used to display the DICEBOX output textually and graphically [8, 51].

The program calculates discrete-level populations from the quasicontinuum, defined as the set of all excited states with energies greater than some critical energy E_{crit} [52]. The DICEBOX algorithm relies on theoretical models of the level density and photon strength function to simulate the level scheme above E_{crit} and calculate the γ-ray transition probabilities in the (n, γ) cascade. The output includes a calculated total radiative neutron-capture cross section σ_0, which results from summing the ground-state population from simulated levels above E_{crit} with the experimentally-measured partial cross sections for transitions feeding the ground state from levels below E_{crit} (illustrated in Figure 11).

By comparing the calculated level populations with experimentally-measured

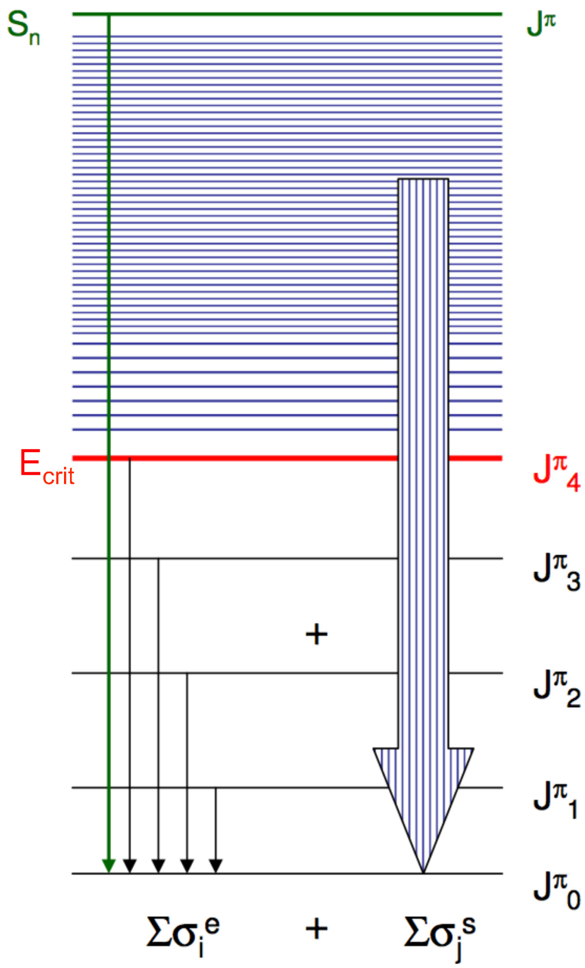

Figure 11. Schematic diagram showing γ-ray transitions following thermal-neutron capture, resulting in a product nucleus with a neutron-separation energy S_n. Contributions to the total thermal-neutron capture cross section σ_0 include the partial cross sections for transitions feeding the ground state from discrete levels below $E_{\rm crit}$ (with spin-parity assignments identified by J_i^π) and the quasicontinuum (levels above $E_{\rm crit}$). The ground-state feeding from the capture state and levels below $E_{\rm crit}$ is given by the sum $\sum \sigma_i^{\rm e}$, and DICEBOX performs a Monte-Carlo simulation to compute the contribution $\sum \sigma_j^{\rm s}$ from the quasicontinuum. Reproduced with permission from [5].

cross sections for depopulating a given level below $E_{\rm crit}$, one can evaluate the accuracy and completeness of nuclear-level scheme information. In this way, DICEBOX can be used as a tool for studying both nuclear reactions and structure.

2.3 Metastable Excited States (Nuclear Isomers)

The motivation for this research is the study of long-lived nuclear isomers, as stated in Chapter I. Long isomer lifetimes result from differences in angular momentum (magnitude and orientation) between the isomer state and lower-lying levels to which the isomer can decay. From an applications perspective, the interest in long-lived isomers is due to their large stored-energy densities. In order to make the energy stored in nuclear isomers useful, it must be possible to induce them to release their energy on demand in a process referred to as isomer depletion.

2.3.1 Spin-trap and K-trap Isomers.

The two types of isomers of interest here are spin-trap and K-trap isomers. In spin-trap isomers the magnitude of the isomer's angular-momentum vector is the dominant factor in its long lifetime, and in K-trap isomers a change in angular-momentum orientation contributes to the isomer lifetime. In plots of excitation energy versus spin J and spin projection K, spin-trap and K-trap isomers appear as local minima, as illustrated in Figure 12. Gamma decays between the isomer and ground states of the nuclei represented in the schematic diagrams of the figure are inhibited.

In spin-trap isomers, significant differences in spin between the isomer and levels to which it can decay result in long isomer lifetimes [19, 25, 53]. In Figure 12(a), this is illustrated by an isomer with a relatively large spin (due to the motion of several valence nucleons) and a $J = 0$ ground state. The lifetimes of spin-trap isomers can be explained by examining the electromagnetic-transition selection rules [Equation (4)] and the Weisskopf estimates [Equations (5) and (6)]. For a transition between states that involves a large change in the magnitude of the angular-momentum vector ($\Delta J = |J_i - J_f|$), the transition must have multipole

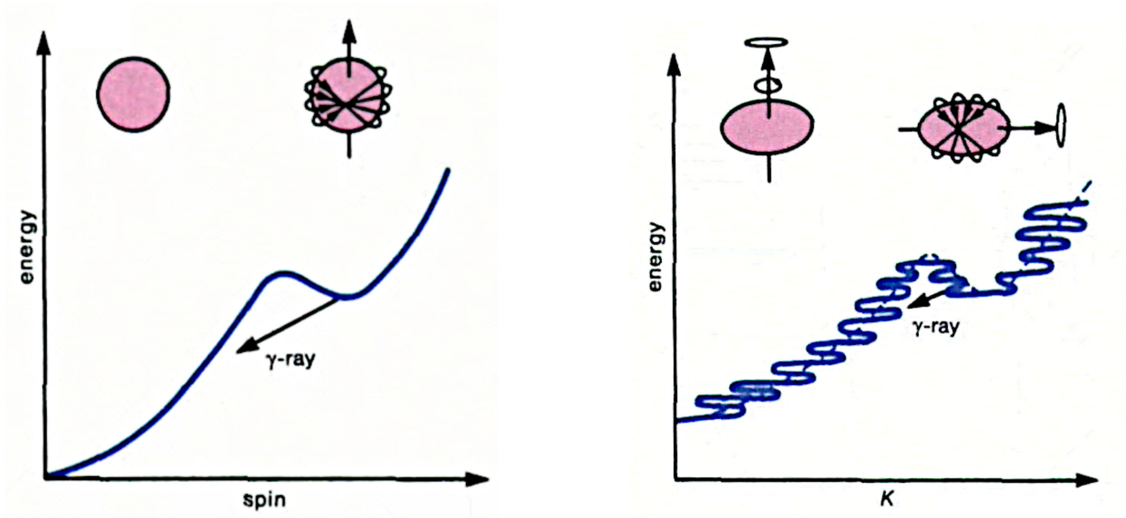

(a) Spin-trap isomer (b) K-trap isomer

Figure 12. Excitation energy plotted as a function of J and K for nuclei with (a) spin-trap and (b) K-trap isomers. In nuclei with both types of isomers, there is a local minimum in the excitation energy that represents the isomer. A wobbling motion (due to Coriolis mixing) of the deformed nucleus is responsible for the variation in the curve shown in (b). Figure copyright 1994, IOP Publishing. Reproduced with permission from [25].

order $L \geq \Delta J$, and large multipole-order transitions have characteristically small decay rates. Thus, for a high-J isomer whose only possible decay paths are to low-J states, the isomer will have a relatively long lifetime. This is precisely the case with the 148.2-keV isomer in ^{186}Re, which only decays by means of an $E5$ transition and has a lifetime of $\sim 2.0 \times 10^5$ y [3].

In deformed nuclei, transitions between states are affected by the K quantum number. When there is a large ΔK between the isomer and lower-lying states to which it can decay, the more-likely dipole and quadrupole transitions are hindered according to Equation (10). This effect increases the lifetime of these so-called K-trap isomers, commonly found in the $A \approx 180$ mass region, in which a change in the orientation of the total angular momentum vector contributes to the isomer lifetime [25, 53]. In Figure 12(b), the angular momentum vector changes orientation by 90° between the isomer and ground state. This represents the maximum possible value of ΔK, so any possible direct transitions between the states are K-hindered.

2.3.2 Activation and Depletion of Isomers.

Although large changes in J or K result in a barrier between the ground state and isomer that inhibits direct transitions between the two states, a sequence of uninhibited (small ΔJ or ΔK) transitions involving a higher-energy intermediate state (IS) can create a pathway. Through such a pathway, a nucleus in the isomer state can be induced to decay to the ground state (isomer depletion), or a nucleus in the ground state can be excited into the isomer (activation).

In isomer depletion, the IS would be a state that is closely matched to the isomer in J and K that is known to decay via γ-ray cascade to the ground state [19]. By resonant excitation from an external source, such as a photon with an energy matching that of a known transition between the IS and the isomer, the nucleus could be raised into the IS. From the IS, the excited nucleus can decay back to the isomer or to the ground state [54, 55]. The opposite scenario represents activation, in which the nucleus is resonantly excited from the ground state into an IS closely matched in J and K to the ground state, from which it can decay by γ-ray cascade to populate the isomer. The processes of isomer depletion and activation via photon excitation are illustrated schematically in Figure 13.

The cross sections for achieving isomer depletion or activation via resonant nuclear excitation are governed by the energy width $\Gamma_{\mathrm{IS}} = \hbar/\tau$ of the IS (where τ is the lifetime of the IS), and by the decay widths $\Gamma^{\gamma}_{i\to\mathrm{IS}}$ and $\Gamma_{\mathrm{IS}\to f}$ of the transitions involved. If the initial state is identified with a subscript i and the final state with a subscript f, then for activation $i = g$ (ground state) and $f = m$ (isomer), and $i = m$ and $f = g$ for depletion. If a transition between an IS and the initial state has an energy $E_{\mathrm{t}} = E_{\mathrm{IS}} - E_i$, then the probability of achieving resonant excitation is high

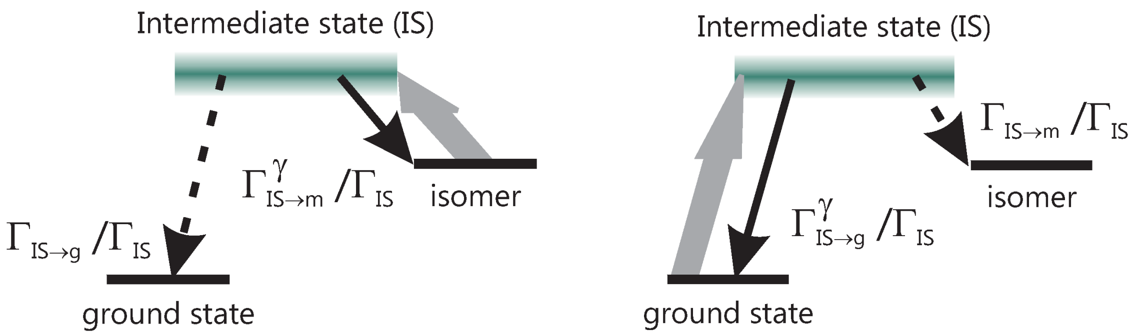

(a) Depletion

(b) Activation

Figure 13. Schematics of isomer depletion and activation schemes involving resonant photon excitation. Gray arrows represent resonant photoexcitation into the IS from the isomer (a) or ground state (b). The dashed lines starting at the IS indicate γ-ray cascade to the ground state (b) or isomer (a), while the solid black lines represent back-decays from the IS to the initial state. The resonance widths for each transition are indicated by the variable Γ. Figure reproduced with permission from [56].

when the source of the excitation transfers energy to the nucleus in the range $E_{\mathrm{t}} \pm \Gamma_{\mathrm{IS}}/2$.

2.3.3 Resonant Photoexcitation.

There are a number of methods for resonantly exciting a nucleus into an IS in order to achieve isomer depletion or activation, one method of which is photon (γ, γ') excitation. The resonances for exciting specific nuclear states via (γ, γ') reactions are narrow compared to the energy FWHMs achievable by high-energy photon sources, so cross sections for depletion and activation are typically reported as integrated cross sections (ICS) [54]. For each IS involved in depletion or activation, there is an associated ICS, based on the lifetime of the IS and the widths of the transitions involved, given by the expression

$$\mathrm{ICS}_{\mathrm{IS}} = \frac{\lambda^2}{4} g \frac{\Gamma^{\gamma}_{i\to\mathrm{IS}} \Gamma_{\mathrm{IS}\to f}}{\Gamma_{\mathrm{IS}}}, \tag{34}$$

where λ is the photon wavelength for a γ-ray transition from an initial state with spin assignment J_i to an intermediate state with spin J_{IS} [57]. The g term is a spin-statistical factor given by

$$g = \frac{2J_i + 1}{2J_{\mathrm{IS}} + 1}. \tag{35}$$

The probability of achieving isomer activation or depletion via photoexcitation with a high-energy photon source (e.g., a Bremsstrahlung generator), is given by the ratio of final-state nuclei N_f to initial-state nuclei N_i

$$\frac{N_f}{N_i} = \sum_j \mathrm{ICS}_j \frac{d\Phi}{dE}, \tag{36}$$

where E is the photon energy, and $\frac{d\Phi}{dE}$ is the time-integrated spectral flux density of the source. The sum is over all the IS with energies accessible given the source spectrum, each with an integrated cross section ICS_j for populating the final state via the j^{th} IS [58].

Although it is possible to calculate individual ICS using Equation (34), the transition widths in the formula depend on accurate knowledge of the lifetimes of all states involved in decay pathways between the IS, ground state, and isomer. In practice, some of these lifetimes are unknown, and a more reliable source for the ICS is direct measurement of (γ, γ') reactions.

2.4 Literature Review

An extensive review of the literature on ^{186}Re was conducted, which covered both nuclear-structure and reaction information. The following sections briefly summarize the structure and reaction data contained in the evaluated and unevaluated databases, which were the primary sources of information about the ^{186}Re nucleus. Sources of information that addressed experimental facilities and analytical techniques are cited in Chapters III, IV, and V.

2.4.1 Nuclear Structure of ^{186}Re.

The Nuclear Science References (NSR) database lists 260 references for the isotope ^{186}Re [59]. The evaluation for the $N = 186$ isobar was last completed in 2003 [3]. Of these 260 references in the NSR, 24 are cited in the ENSDF, including four articles that establish the nuclear level scheme [21, 60, 61, 62]. The remaining 20 articles cited in the ENSDF address other nuclear data such as quadrupole moments, half-life, and mass.

The first published analysis of the low-energy level structure of ^{186}Re was performed by Lanier *et al.* in 1969, which incorporated data from (d, p), (d, t), and (n, γ) reactions [60]. This paper was followed by the discovery, reported in 1972 by Seegmiller, Lindner, and Meyer, of an isomer with an excitation energy of 149(7) keV [21]. The group used mass spectrometry and decay-γ spectroscopy of an irradiated $^{\mathrm{nat}}$Re sample to measure an isomer lifetime of 2.0×10^5 y. The measured lifetime was compared with the Weisskopf estimates to deduce that the isomer decays via a ~50-keV $E5$ transition to the $J^\pi = 3^-$ state at 99.3 keV. From this, the isomer spin-parity was reported as $J^\pi = 8^+$. The partial ^{186}Re level scheme from Reference [21] is shown in Figure 14. The proposed feeding of the isomer shown in Figure 14 from the 186-keV and 259-keV levels has not been confirmed, and the structure above the isomer in the ENSDF-adopted level scheme is absent entirely [3].

The majority of the rotational-band structure for ^{186}Re included in the ENSDF is the result of a γ-γ coincidence analysis by J. Glatz from slow-neutron capture on ^{185}Re in 1973 [61]. Further information about the low-spin level structure was reported by F. Bečvář *et al.* in 1983, which was the result of prompt-γ spectroscopy from ^{185}Re(n, γ) reactions at resonant $(E_n = 2 - 110$ eV$)$ neutron energies [62].

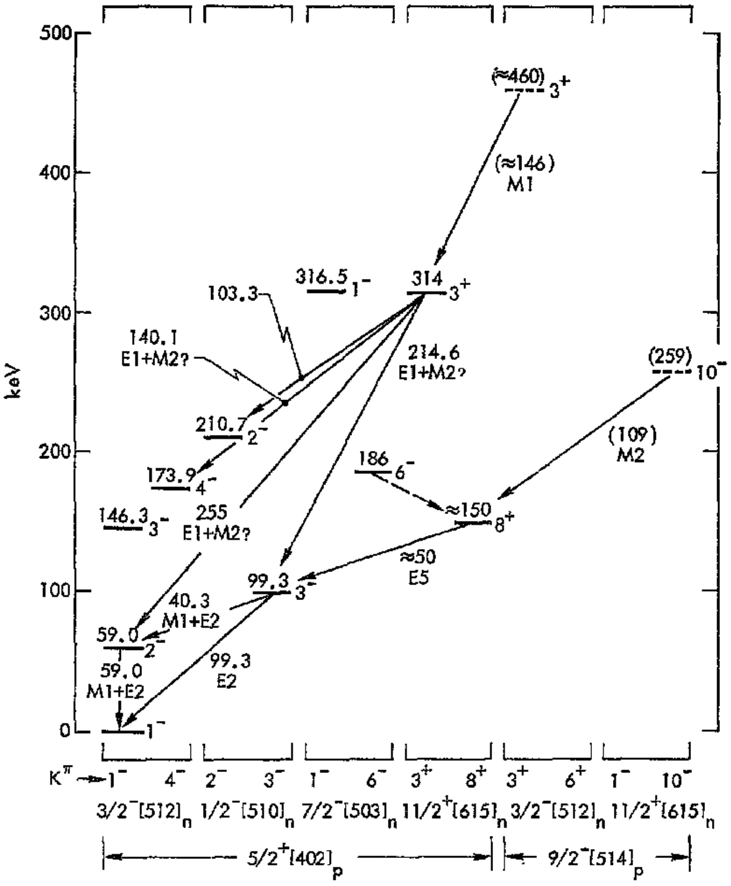

Figure 14. Partial ^{186}Re level scheme showing orbitals for the unpaired proton and neutron in the Nilsson convention K^{π} $[Nn_z\Lambda]$ below the horizontal axis. The spherical-state J^{π} corresponding to each state is identified next to the the respective level in the diagram, while the K^{π} values for each distinct two-particle state appear at the bottom of the diagram. Tentative assignments are identified with parentheses, and the two transitions feeding the ~150-keV isomer are questionable. Figure copyright 1972 Elsevier B.V. Reproduced with permission from [21].

The XUNDL includes one article with a date of 2009, so the data contained in the article have not yet been evaluated for inclusion in the ENSDF. This work, by C. Wheldon *et al.*, is an investigation of excited states in ^{186}Re populated in the transfer reaction ^{187}Re(p, d). Level energies were determined by measuring the energy differences between the incident protons and the outgoing deuterons, and the group reported the discovery of 30 new levels in ^{186}Re [63]. Experimental level energies were compared with the results of Nilsson-model calculations to propose configurations for some of the new levels.

2.4.2 Neutron-capture Cross Sections for ^{185}Re.

Total neutron-capture cross-section data for ^{185}Re contained in the ENDF are based on the 1987 measurements of Macklin and Young and modeled cross sections from the TALYS code [64, 45]. Partial γ-ray production cross-section data are contained in the Evaluated Gamma-ray Activation File (EGAF), a database of neutron-capture γ-ray cross sections used for elemental analysis. [65] The data contained in the EGAF for the $^{185}\mathrm{Re}(n,\gamma)^{186}\mathrm{Re}$ reaction were evaluated in 2003 by R. Firestone, and they consist of cross sections from thermal-neutron irradiation of elemental rhenium at the BRR [65].

III. Fast Neutron Reactions on ^{187}Re

The study of the structure of ^{186}Re using the neutron-induced reaction $^{187}\mathrm{Re}(n,2n)^{186}\mathrm{Re}$ described in this chapter resulted in a manuscript submitted for publication in the American Physical Society journal Physical Review C on 26 July 2015. Referee criticism was received on 27 August, and the manuscript was resubmitted on 9 September. This chapter contains the full text of the manuscript, titled "New transitions and feeding of the $J^{\pi} = (8^{+})$ isomer in ^{186}Re," as it was published on 9 November 2015. It is reproduced from Reference [22] with permission. Further information about the experimental facilities and data analysis techniques is contained in Reference [66].

The manuscript was prepared by the primary author in cooperation with scientists from the Army Research Laboratory (ARL) and LANSCE. J. J. Carroll and C. J. Chiara of ARL participated in the experiment and provided key insights and expertise during the data analysis and interpretation. N. Fotiades of LANSCE, the principal investigator for the experiment, was responsible for the experimental setup and execution, and he provided expertise with data sorting and analysis techniques. R. O. Nelson and M. Devlin of LANSCE were subject-matter experts for the GEANIE detector array, and were involved in the experiment execution. J. W. McClory of AFIT, the primary author's research advisor, provided guidance throughout the project and reviewed the manuscript. Finally, LANSCE theorist T. Kawano wrote the CoH 3.4 code used to validate and interpret the experimental cross-section data, and he informed the primary author on the application of the code to this particular study.

3.1 Abstract

The spallation neutron source at the Los Alamos Neutron Science Center Weapons Neutron Research facility was used to populate excited states in ^{186}Re via $(n, 2n\gamma)$ reactions on an enriched ^{187}Re target. Gamma rays were detected with the the GErmanium Array for Neutron Induced Excitations spectrometer, a Compton-suppressed array of 18 HPGe detectors. Incident neutron energies were determined by the time-of-flight technique and used to obtain γ-ray excitation functions for the purpose of identifying γ rays by reaction channel. Analysis of the singles γ-ray spectrum gated on the neutron energy range $10 \leq E_n \leq 25$ MeV resulted in five transitions and one level added to the ^{186}Re level scheme. The additions include the placement of three γ rays at 266.7, 381.2, and 647.7 keV which have been identified as feeding the 2.0×10^5 y, $J^\pi = (8^+)$ isomer and yield an improved value of 148.2(5) keV for the isomer energy. These transitions may have astrophysical implications related to the use of the Re/Os cosmochronometer.

3.2 Introduction

The Re/Os radioactive decay system is a cosmochronometer for estimating the age of astronomical objects through the measurement of the relative abundances of ^{187}Re ($T_{1/2} = 4.33 \times 10^{10}$ y) and ^{187}Os (stable) [11]. The *s*-process nucleosynthesis of ^{187}Re and ^{187}Os includes ^{186}Re as a branch point, shown in Figure 15. ^{186}Re in the ground state can decay with a half-life of 3.7186 d into ^{186}Os or ^{186}W or undergo neutron capture to create ^{187}Re [14, 67], but it also possesses an especially long-lived isomer ($T_{1/2} = 2.0 \times 10^5$ y) with an excitation energy of 149(7) keV that decays 100.0% by isomeric transition to the ground state [3].

Depending on the stellar temperatures present in the *s*-process environment, the population of the ^{186}Re^m isomer may be significantly affected by the photon-induced

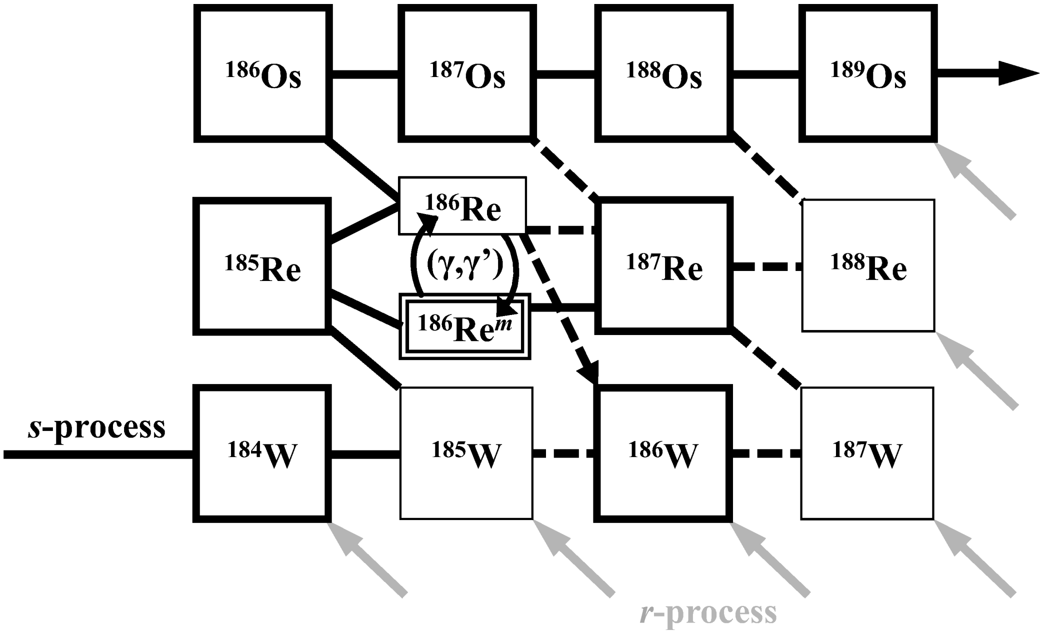

Figure 15. ***s*- and *r*-processes, identified by black and gray arrows, involved in the production of ^{187}Re and ^{187}Os. Long-lived nuclides are identified with bold boxes, with the dashed lines indicating weaker secondary processes. The outline around the isomer ^{186}Re^m and the associated (γ, γ') pathways highlight the fact that their effects are not fully understood.**

reactions ^{186}Re$(\gamma, \gamma')^{186}$Re^m and ^{186}Re$^m(\gamma, \gamma')^{186}$Re (photoexcitation and depletion, respectively). Estimation of the cross sections for these reactions requires knowledge of the ^{186}Re level structure above the isomer, and in particular identification of intermediate states (IS) present in pathways from the ground state to the isomer and vice versa. For IS excitation energies below 1 MeV, temperatures on the order of 10^8 K can result in thermal coupling between the isomer and ground states with the potential to increase the production of the ^{186}Re^m isomer [68]. This would lead to a temperature-dependent effective half-life for ^{186}Re, which could be determined using the methodology outlined in References [68, 69, 70, 71] for ^{180}Ta and ^{176}Lu. A temperature-dependent effective half-life for ^{186}Re would affect creation of ^{187}Re and represents a potential source of error in the Re/Os chronometer.

Based on an analysis of cross sections for neutron capture and the photodisintegration reaction ^{187}Re$(\gamma, n)^{186}$Re, Käppeler *et al.* concluded that the

s-process contribution to ^{187}Re due to the branching at ^{186}Re was insignificant. Other than in the case of the population of the isomer via the $^{187}\text{Re}(\gamma, n)^{186}\text{Re}^m$ reaction cited in Reference [72], the isomer's possible role in the s-process branching was not discussed.

Hayakawa *et al.* were the first to propose an alternate s-process pathway that involved the $^{186}\text{Re}^m$ isomer. The group concluded that the isomer's contribution to the creation of ^{187}Re was $0.56\% \pm 0.35\%$ and is therefore an insignificant source of error in the Re/Os chronometer [17]. However, this analysis assumed that transitions between the ground state and isomer in ^{186}Re via (γ, γ') reactions were negligible, based in part on the absence of known IS by which the resonant photoexcitation/depletion reactions could proceed. Knowledge of the low-lying IS involved in photon-induced reactions requires further investigation of the structure above the isomer in ^{186}Re, and is necessary to establish conclusions about the transition probabilities between the isomer and ground state in the s-process environment.

Using the GErmanium Array for Neutron Induced Excitations (GEANIE) detector array at the Los Alamos Neutron Science Center (LANSCE) Weapons Neutron Research (WNR) facility, γ-ray spectra obtained from neutron-induced reactions were used to identify new γ-ray transitions in ^{186}Re and to verify transitions and levels already described in the existing literature [3, 21, 60, 61, 62, 63, 73]. The primary neutron-induced reaction studied was $^{187}\text{Re}(n, 2n\gamma)^{186}\text{Re}$ from irradiating an enriched ^{187}Re target. Neutron energies were measured using the time-of-flight technique, and excitation functions for observed γ-ray transitions were generated and compared to those modeled using the reaction codes CoH 3.4 [50] and Talys 1.6 [74] for the purpose of placing transitions in the ^{186}Re level scheme.

3.3 Experiment

The LANSCE accelerator is a proton linac capable of producing beams of postively- and negatively-charged hydrogen ions with energies up to 800 MeV. For experiments at the WNR facility, spallation neutrons with energies ranging from 100 keV to 600 MeV are produced by directing pulses of H^- ions with an average current of 0.5 to 4 μA at a $^{\rm nat}$W target [75].

The GEANIE target is located 20.34 m from the spallation source along the 60° right flight path. The beam has a macropulse repetition rate of 40 or 100 Hz, with each 625-μs macropulse further divided into numerous sub-nanosecond micropulses spaced 1.8 μs apart. The pulsed nature of the beam provides the ability to measure neutron energies using the time-of-flight method, and the detection system is capable of resolving neutron energies from 0.6 to ∼200 MeV. Neutron flux at the target is measured with a fission chamber positioned at the terminus of the neutron beam tube, 18.48 m from the spallation target. The fission chamber consists of an ionization chamber that incorporates stainless steel foils coated with ^{235}U and ^{238}U, so that the known fission cross sections of these isotopes can be used to calculate the neutron flux from the counts of fission events in the ionization chamber [76]. In the $10 \leq E_n \leq 25$ MeV neutron energy range of interest for the $(n, 2n\gamma)$ reaction, the neutron fluence for the run was determined to range from $1.3 \times 10^8 - 5.0 \times 10^8$ neutrons/MeV, decreasing with increasing neutron energy. A representative profile of the fluence versus neutron energy for the GEANIE flight path can be found in Reference [77]. The size of the neutron beam arriving at the target was trimmed to a diameter of 1.27 cm using an iron collimator, prior to the beam transiting the fission chamber. More detailed information about the LANSCE facility and the GEANIE spectrometer is available in References [75, 77, 78, 79].

For this experiment, the GEANIE detector array was configured with eight planar and ten coaxial high-purity germanium (HPGe) detectors to optimize resolution and efficiency up to γ-ray energies of 4.0 MeV. Each detector was Compton suppressed using a bismuth germanate (BGO) shield. Of the 18 installed detectors, seven of each type provided usable data for offline analysis. Gamma rays were produced via neutron bombardment of a 987.1-mg target consisting of vacuum-pressed rhenium metal powder enriched to 99.52% ^{187}Re. The 1.0-mm-thick ^{187}Re target was encapsulated in a disk-shaped polycarbonate target holder. The end faces of the disk were oriented normal to the incident neutron beam. The enriched rhenium target was irradiated for 12 days at a pulse repetition rate of 40 Hz and an additional five days at 100 Hz. Energy and efficiency calibrations of the spectrometer were performed using standard ^{133}Ba and ^{152}Eu calibration sources.

3.4 Analysis and Results

The data output by the TDCs and ADCs connected to the HPGe detectors in the GEANIE array were processed online into E_γ versus neutron time-of-flight (ToF) matrices using software based on the MIDAS data acquisition package [80]. The matrices, which were generated for each HPGe detector and the fission chamber, were used to produce singles γ-ray spectra gated on specified neutron-energy ranges. A neutron-energy range of $10 \leq E_n \leq 25$ MeV was used to select the γ rays that originated primarily from $(n, 2n)$ reactions on the ^{187}Re target, as shown in the spectrum of Figure 16. Singles γ-ray spectra were fitted using the GF3 program from the RADWARE software distribution [81].

For each peak identified in the singles spectrum, the matrices were gated successively on 1-MeV-wide neutron-energy bins over the energy range $1.0 \leq E_n \leq 100$ MeV, and peaks were re-fitted to produce γ-ray yield as a function of incident neutron energy. The yield functions were divided by neutron flux to

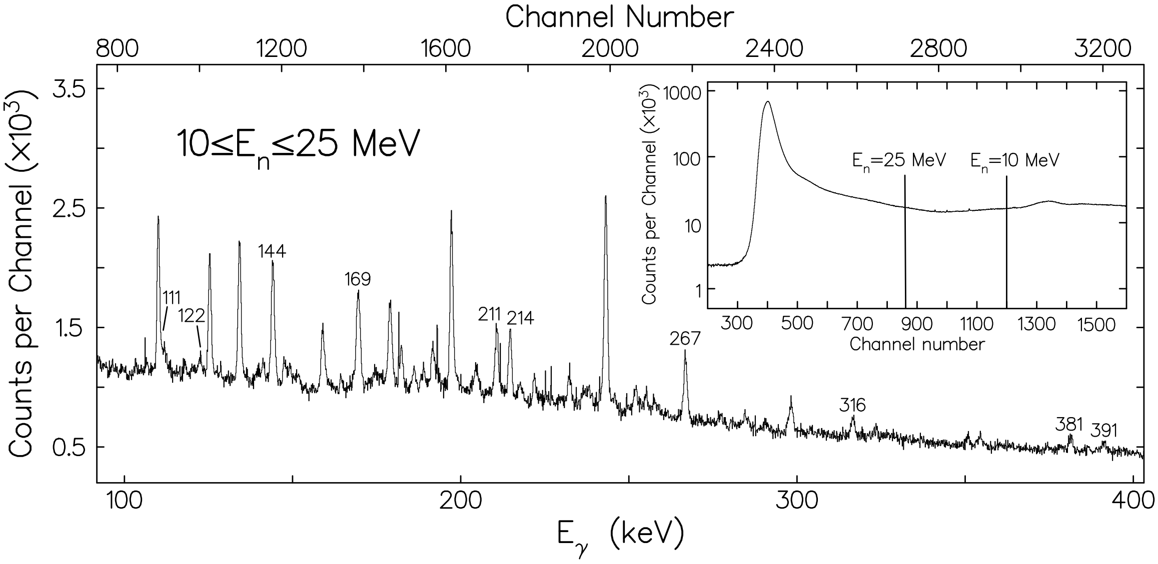

Figure 16. Summed γ-ray spectrum from the planar HPGe detectors, gated on $10 \leq E_n \leq 25$ MeV. Prominent peaks due to ^{186}Re are labeled by energy in keV, up to 400 keV. Unlabeled peaks were identified as γ rays from reactions other than ^{187}Re$(n, 2n\gamma)^{186}$Re. The inset shows the projection of the E_γ-vs.-neutron-ToF matrix on the ToF axis and the channel locations corresponding to the neutron energy cuts of 10 and 25 MeV.

produce excitation functions for each distinct γ-ray energy. For γ rays originating from the ^{187}Re$(n, 2n\gamma)^{186}$Re channel, the excitation functions rise quickly following the ^{187}Re neutron separation energy of $S_n = 7.3568$ MeV [82] to peak at neutron energies between 10 and 20 MeV [83], then decrease rapidly as the $(n, 3n\gamma)$ reaction becomes energetically favorable. The distinctive shape of the $(n, 2n\gamma)$ excitation functions distinguishes the ^{186}Re γ rays from those produced in the $(n, n'\gamma)$ and $(n, 3n\gamma)$ reaction channels, which result in excitation functions that rise and peak at neutron energies approximately 7.5 MeV lower or higher, respectively, than that of the $(n, 2n\gamma)$ channel.

Gamma rays originating from the ^{187}Re$(n, pn\gamma)^{186}$W channel also have excitation functions with a positive slope in the 10–20 MeV neutron-energy range, similar to those from the $(n, 2n\gamma)$ channel. The $(n, pn\gamma)$ excitation functions, however, show a distinctly different behavior at neutron energies above 20 MeV, where they decay much more slowly than do the $(n, 2n\gamma)$ excitation functions. To support the assignment of γ rays to ^{186}Re instead of ^{186}W in this analysis, the areas of the γ-ray peaks in the gated ($10 \leq E_n \leq 25$ MeV) projection spectrum were compared to those from the most intense γ rays in ^{186}W, the 122.64-keV $2^+ \rightarrow 0^+$ and 273.93-keV $4^+ \rightarrow 2^+$ transitions [3]. The spectrum shown in Figure 16 reveals the presence of a 122-keV peak, which is due partly to the 122.525-keV γ ray from the $(4)^- \rightarrow (3)^-$ transition in ^{186}Re, while no peak at 273.93 keV is evident. No other γ rays from ^{186}W were identifiable in the gated spectrum. This observation is supported by the fact that the ENDF/B-VII.1 total cross section at $E_n = 15$ MeV for the $^{187}\text{Re}(n, pn)^{186}\text{W}$ reaction is over two orders of magnitude smaller than that of the $^{187}\text{Re}(n, 2n)^{186}\text{Re}$ reaction [45]. Unknown γ rays with excitation functions that met the $(n, 2n\gamma)$ criteria discussed above were therefore attributed to ^{186}Re.

A total of 29 γ-ray peaks in the singles spectrum were attributed to ^{186}Re, including the nine γ rays cataloged in Table 1 that are not included in the evaluated level scheme [3]. A 1969 work by Lanier *et al.* also identified 186.00(8)-, 217.91(10)-, 266.70(20)-, and 354.10(5)-keV γ-ray transitions in ^{186}Re, similar in energy to four of the γ rays listed in Table 1, which were not placed in the ^{186}Re level scheme [3, 60]. These γ rays were observed in prompt γ-ray spectra from $(n_{\text{thermal}}, \gamma)$ reactions on ^{185}Re, measured using a bent-crystal spectrometer during irradiation of a sample of 79.2% ^{185}Re and 20.8% ^{187}Re at Risø, Denmark [60].

Table 1. Energies of γ rays attributed to ^{186}Re in this work that are not included in the evaluated level scheme [3]. Gamma rays were attributed to ^{186}Re based on an analysis of their excitation functions. Asterisks indicate γ rays observed but not placed in the level scheme in this work.

E_γ^{exp} (keV)	E_γ^{exp} (keV)	E_γ^{exp} (keV)
185.99(6)*	290.51(13)*	647.7(2)
217.62(10)*	354.28(9)*	1007.5(3)
266.69(4)	381.23(7)	1101.3(3)

The shapes of the excitation functions were further used to estimate the spin of the initial level of each observed transition. Transitions originating from low-spin states have excitation functions that rise sharply after the threshold energy of the $(n, 2n)$ reaction to peak at neutron energies near 13 MeV, while those originating from high-spin states rise more gradually and peak at neutron energies between 15 and 20 MeV. This effect is evident in Figure 17, in which excitation functions for known 111.7- and 188.8-keV γ-ray transitions in ^{186}Re are compared with that of the 266.7-keV transition assessed to originate from a high-spin state.

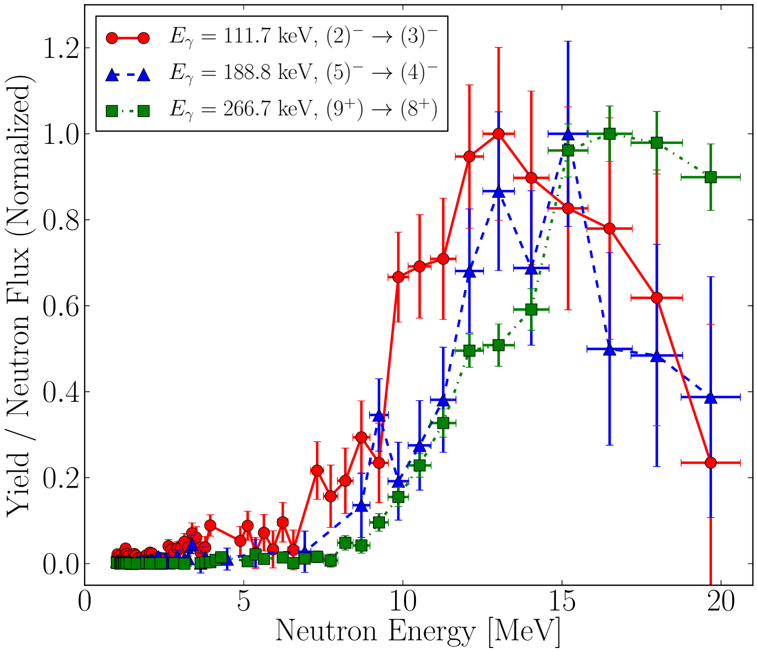

Figure 17. Experimental excitation functions for the 111.7-, 188.8-, and 266.7-keV γ-ray transitions in the ^{187}Re$(n, 2n\gamma)^{186}$Re reaction channel, normalized for the purpose of comparing their shapes. Excitation functions for transitions that originate from higher-spin states show a slower rise after the reaction threshold energy than do those originating from low-spin states. The excitation function for the 266.7-keV transition is included in the plot according to its assignment in this work as deexciting a (9^+) level to feed the (8^+) isomer.

The transitions and levels placed in the ^{186}Re level scheme in this work are listed in Table 2 and illustrated in the partial level scheme shown in Figure 18. Gamma rays previously reported were placed according to their assignment in the evaluated literature [3, 21, 60, 61, 62, 73]. Five of the nine transitions listed in Table 1 were added to the level scheme based on energy differences of levels reported in References [3] and [63] and an analysis of their excitation functions. There was insufficient information to guide the placement of the remaining four transitions, identified with asterisks in Table 1, so these were not included in the level scheme.

Table 2. Excitation energies, spin-parities, and transition energies for all levels and γ rays shown in Figure 18. Excitation energies E_x and spin-parity values J^π are the literature values unless identified in bold italics to indicate values proposed in this work. Experimental γ-ray energies E_γ^{exp} were obtained by fitting the gated $10 \le E_n \le 25$ MeV spectrum of Figure 16. Literature values E_x^{lit} and E_γ^{lit} for excitation and γ-ray energies are shown in the second and fifth columns for comparison and are taken from the adopted values listed in Reference [3] unless otherwise indicated.

E_x (keV)	$E_x^{\rm lit}$ (keV)	J^π	$E_\gamma^{\rm exp}$ (keV)	$E_\gamma^{\rm lit}$ (keV)
0.0	0.0	1^-		
59.010(3)	59.010(3)	$(2)^-$		
99.361(3)	99.361(3)	$(3)^-$		
146.274(4)	146.274(4)	$(3)^-$		
148.2(5)	149(7)	(8^+)		
~ 186	~ 186	$(6)^-$		
210.699	210.699	$(2)^-$	111.74(5)	111.337(8)
			151.38(8)	151.686(5)
			210.74(6)	210.685(17)
268.798	268.798	$(4)^-$	122.45(6)	122.525(5)
			169.44(11)	169.431(8)
			210.12(10)	209.82(2)
273.627(5)	273.627(5)	$(4)^-$		
314.009	314.009	$(3)^+$	214.60(3)	214.648(8)
			255.05(6)	254.995(15)
316.463	316.463	$(1)^-$	257.45(7)	257.446(15)
			316.45(5)	316.473(20)
322.379(6)	322.379(6)	$(3)^-$		
~ 330	~ 330	$(5)^+$	144.08(2)	144.152(5)
351.202(16)	351.202(16)	$(3)^+$		
414.9(5)[a]	414.9(5)[a]	***(9⁺)***	266.69(4)	266.70(20)[b]
420.559(7)	420.559(7)	$(4)^+$		
462.969	462.969	$(5)^-$	188.79(7)	189.313(17)
469.779	469.779	$(4)^-$	147.60(7)	147.417(6)
~ 471	~ 471	$(4)^+$	141.23(6)	141.257(5)
500.722	500.722	$(4)^+$	149.23(8)	149.520(5)
559.976	559.976	$(5)^+$	139.62(12)	139.416(7)
588.709	588.709	(4^-)	117.92(13)	118.196(4)
601.58	601.58	$(1)^+$	391.09(11)	390.91(5)
623.89	623.89	(1^-)	413.53(12)	413.21(6)
665.188	665.188	$(5)^+$	164.7(3)	164.466(8)
796.1(5)		***(10⁺)***	381.23(7)	
			647.7(2)	
1007.5(3)	1007.4(20)[a]		1007.5(3)	
1101.3(3)	1101.9(5)[a]	$(2^-,3^-)$	1101.3(3)	

[a] Proposed in Reference [63]

[b] Proposed in Reference [60]

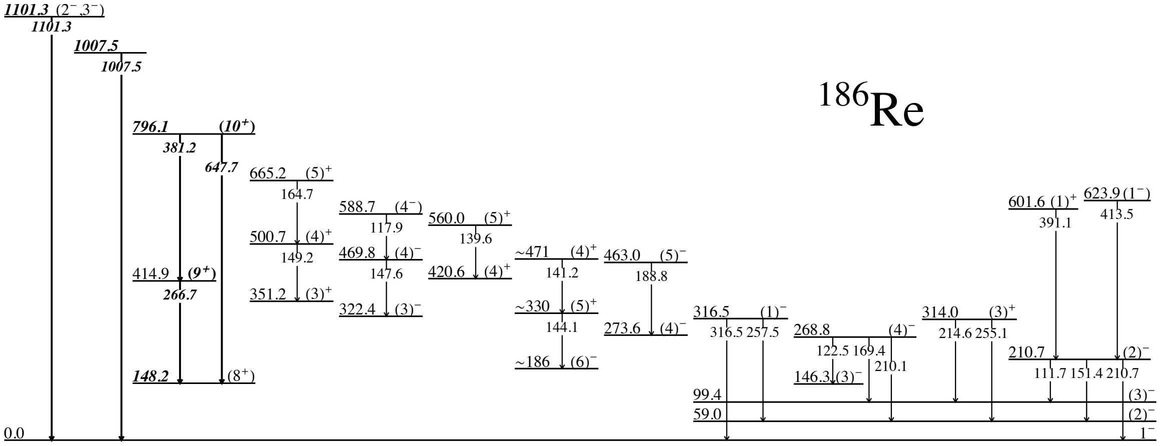

Figure 18. Partial level scheme for ^{186}Re showing the transitions observed in this work, with energies labeled in keV and tentative assignments identified with parentheses. Levels or transitions with properties in bold italics indicate proposed level energies and spin-parity assignments or transitions placed in this work. All other level energies and spin-parity assignments are those in the adopted level scheme for ^{186}Re [3].

Gamma-gamma coincidence matrices were also generated during offline data analysis, but the statistics from the γ-ray peaks produced with the neutron-energy gates of $10 \leq E_n \leq 25$ MeV applied were insufficient to assist in developing the ^{186}Re level scheme. The lack of useful coincidence data prevented the elimination of background contributions from other reaction channels in the examination of transitions of interest in ^{186}Re. Because the majority of observed γ-ray transitions showed contributions from reactions other than $(n, 2n\gamma)$ in their excitation functions, γ-ray intensities for decays in ^{186}Re could not be reliably determined and thus are not reported.

The ^{186}Re level scheme had previously been investigated primarily with information obtained from (n, γ), (d, p), and (d, t) reactions, so the low-spin $(\leq 6\hbar)$ portion of the level scheme is well-developed [3]. A 2009 paper by Wheldon *et al.* described over 30 new levels in ^{186}Re populated by (p, d) reactions on ^{187}Re at proton energies of 21 MeV, including higher-spin states not yet included in the evaluated data file [3, 63]. Measurement of the deuteron energies using a magnetic spectrograph, combined with knowledge of the incident proton energy, permitted the group to calculate excitation energies and population intensities of levels in the (p, d) reaction.

Several of the states first reported by Wheldon *et al.* were observed to be populated in the $(n, 2n)$ reaction described in this work. The 1007.5- and 1101.3-keV γ rays were placed based on the existence of levels at energies 1007.4(20) keV and 1101.9(5) keV reported in Reference [63]. Of greater significance to this study was the 414.9(5)-keV level populated in the (p, d) reaction, which was identified in Reference [63] as a higher-spin state with a possible spin-parity assignment of $J^\pi = 7^-$. In this work, the 414.9(5)-keV level was assessed as directly feeding the 149(7)-keV isomer via a 266.69(4)-keV transition, providing an improved estimate of 148.2(5) keV for the isomer energy.

The assignment of the 266.7-, 381.2-, and 647.7-keV transitions above the isomer in the level scheme of Figure 18 is supported by similarities between ^{186}Re and the neighboring odd-odd isotope ^{184}Re. Both isotopes have long-lived isomers in the 140- to 190-keV energy range, with equivalent $(\pi 5/2[402]) + (\nu 11/2[615])$ configurations [3, 21, 84]. Evaluated nuclear data reveals a well-defined structure above the $J^\pi = 8^{(+)}$ isomer in ^{184}Re, which includes 446.0-keV, $J^\pi = (9^+)$, and 727.9-keV, $J^\pi = (10^+)$, levels feeding the 188.0-keV isomer. Expecting the level structure above the isomer in ^{186}Re to show similarities to that in ^{184}Re, the analogous levels are those at 414.9 keV and 796.1 keV. The new level in ^{186}Re at 796.1 keV deexcites by emission of 381.2- and 647.7-keV γ rays. On the basis of the similar high-spin components in the excitation functions for the 381.2- and 647.7-keV γ rays, the spin-parity assignment for the 796.1-keV level is proposed as $J^\pi = (10^+)$ in this work.

Further motivating the assignment of levels above the isomer in ^{186}Re is the output from the reaction models CoH 3.4 and Talys 1.6 for a variety of considered spin assignments for the 414.9- and 796.1-keV levels. Both CoH 3.4 and Talys 1.6 incorporate an optical model and Hauser-Feshbach statistical calculations to simulate partial γ-ray cross sections given discrete level information for the nuclei involved in the reactions of interest. Due to the presence in the spectrum of γ rays from reactions other than $(n, 2n\gamma)$, experimental excitation functions included some fraction of the yield from all reaction channels that produced γ rays close to a given energy. To model this appropriately, the simulated partial cross sections from CoH 3.4 and Talys 1.6 for γ rays in the ^{187}Re$(n, 2n\gamma)^{186}$Re reaction channel were added to those from similar-energy γ rays produced in $(n, n'\gamma)$ and $(n, 3n\gamma)$ reactions. The experimental and simulated excitation functions were then normalized for the purpose of comparing their shapes, revealing in some cases a double peak when the partial γ-ray cross sections from different reaction channels had similar magnitudes.

In the case of the 266.7-keV γ-ray transition, the models demonstrate a poor fit to the experimental excitation function when the 414.9-keV level is assumed to have a spin less than $9\hbar$, evident in the plot shown in Figure 19. For the 381.2-keV γ-ray transition, the models demonstrate acceptable fits to the experimental excitation function only when the 796.1-keV level is assumed to have a spin of $10\hbar$ or greater. Output from CoH 3.4 is similar to that produced by Talys 1.6, and the shapes of the modeled excitation functions show only a minor parity dependence.

For each of the new transitions placed in the ^{186}Re level scheme, the experimental excitation functions were compared with those from CoH 3.4 and Talys 1.6 for the proposed assignments in Table 2 and Figure 18. Examples for the 266.7-, 381.2-, and 647.7-keV transitions are shown in Figure 20. The 796.1-keV level is not as strongly populated as the 414.9-keV level, so the lower-intensity 381.2- and 647.7-keV γ rays produce excitation functions with larger error bars than

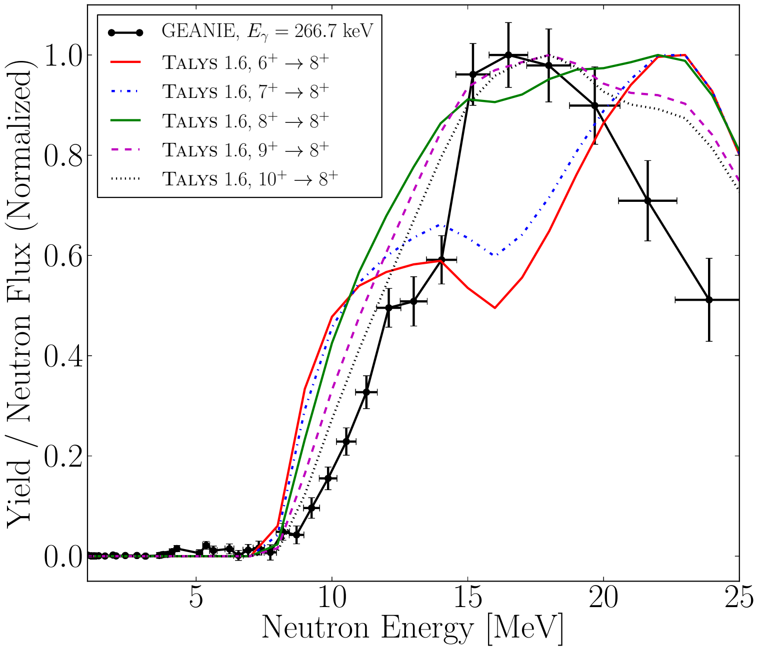

Figure 19. Experimental and TALYS-modeled excitation functions for the 266.7-keV γ-ray transition in the ^{187}Re$(n, 2n\gamma)^{186}$Re reaction channel, normalized for the purpose of comparing their shapes. Talys input was modified to include several spin-parity assignments for the initial level to rule out low-spin states feeding the isomer. The shapes of the $6^+ \rightarrow 8^+$, $7^+ \rightarrow 8^+$, and $8^+ \rightarrow 8^+$ excitation functions reveal contamination from the 267-keV transition in ^{185}Re produced in the $(n, 3n\gamma)$ reaction channel.

those of the 266.7-keV γ ray. However, both models reproduce the general shapes of the experimental excitation functions and suggest that all three γ rays originate from high-spin states as proposed in Table 2 and Figure 18.

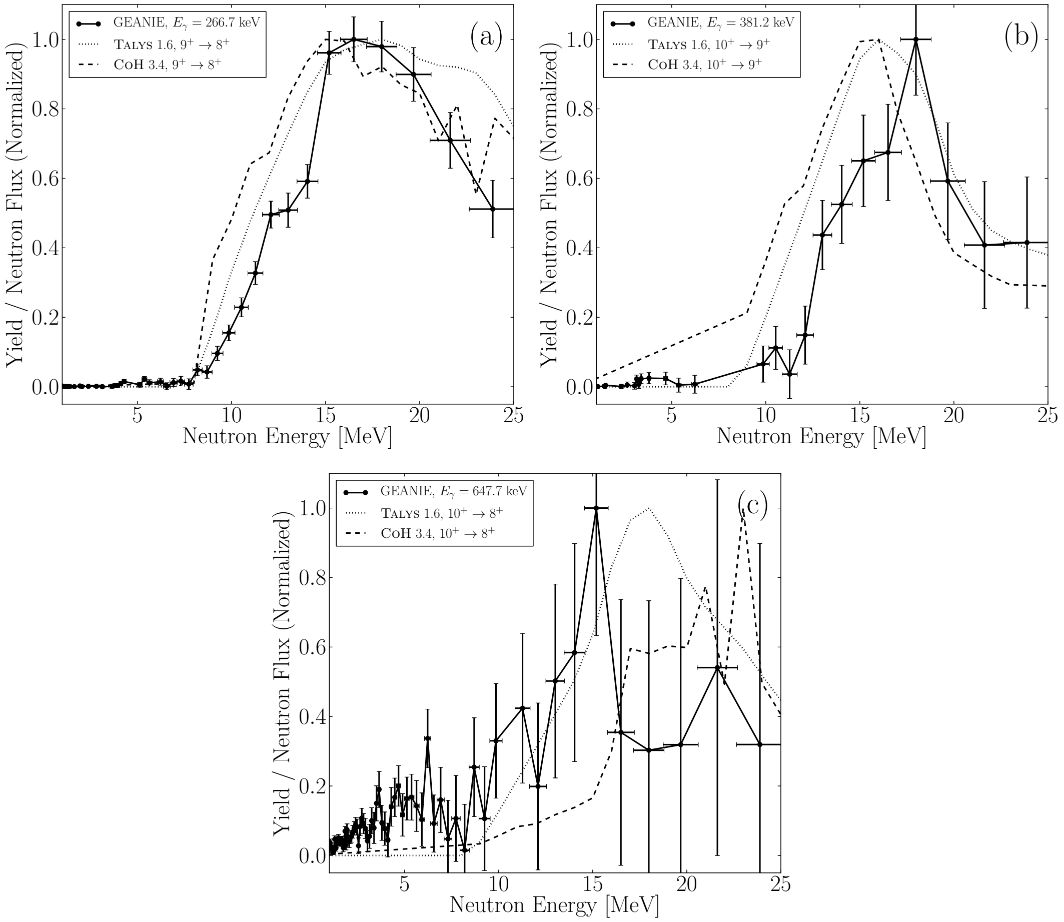

Figure 20. Excitation functions up to 25-MeV incident-neutron energy for the (a) 266.7- (b) 381.2- and (c) 647.7-keV γ rays observed in the GEANIE data. Plots are overlaid with simulated excitation functions from CoH 3.4 and TALYS 1.6 for the assignments proposed in Figure 18 and Table 2.

3.5 Conclusions

The significant outcome of this experiment was enriching the ^{186}Re level scheme with the addition of five newly placed transitions and one new level. In particular, the structure above the 2.0×10^5 y isomer in ^{186}Re has not been previously reported, and new γ-ray transitions observed in the $^{187}\text{Re}(n, 2n\gamma)^{186}\text{Re}$ reaction channel may be evidence of pathways by which the isomer is populated. Comparison of experimental and simulated excitation functions for the observed γ-ray transitions confirm the high-spin ($J \geq 7\hbar$) nature of certain levels populated in the $(n, 2n)$

reaction, while similarities between the neighboring odd-odd isotopes ^{184}Re and ^{186}Re motivated the assignment of levels and transitions above the isomer.

The new transitions identified in this work lead to an improved determination of the excitation energy of the ^{186}Re^{m} isomer with a smaller uncertainty than the reference value. The energy adopted in Reference [3] for the 2.0×10^{5} y isomer in ^{186}Re is 149(7) keV, based solely on the work of Seegmiller *et al.* [21]. The 266.69(4)-keV γ ray attributed to ^{186}Re is proposed in this work to be a transition to the isomer state from the 414.9(5)-keV level identified by Wheldon *et al.* [63]. This places the isomer energy at 148.2(5) keV, an order-of-magnitude improvement in uncertainty compared to the adopted value.

The observation of transitions feeding the isomer from higher-lying levels is a first step toward evaluating ^{186}Re as a branch point for stellar nucleosynthesis. Of future interest are the energies of low-lying IS in ^{186}Re which have decay branches leading towards both the isomer and the ground state. Such IS, which may deexcite via the 266.7-, 381.2-, and 647.7-keV transitions described in this work, are critical to the population or depopulation of the ^{186}Re^{m} isomer via (γ, γ') reactions in stellar environments. With knowledge of the astrophysically relevant IS involved in these resonant reactions, probabilities for isomer photoactivation and depletion can be estimated and the associated effects on the accuracy of the Re/Os chronometer evaluated.

IV. Radiative Neutron Capture on ^{185}Re

The study of the structure of ^{186}Re via (n, γ) reactions on ^{185}Re described in this chapter resulted in a manuscript submitted for publication in Physical Review C on 28 March 2016. The manuscript, titled "Investigation of ^{186}Re via radiative thermal-neutron capture on ^{185}Re" was published on 16 May 2016, and the full text is reproduced here with permission from Reference [43].

The manuscript was prepared by the primary author, building on the AFIT master's thesis work of A. G. Lerch (Reference [85]). The experiment was performed at the BNC by J. J. Carroll and B. Detwiler, then of Youngstown State University, and L. Szentmiklósi, Zs. Révay, and T. Belgya of the Hungarian Academy of Sciences. A. M. Hurst and R. B. Firestone of Lawrence Berkeley National Laboratory (LBNL) provided expertise with (n, γ) data analysis techniques and statistical modeling. J. W. McClory and S. R. McHale of AFIT provided guidance throughout the project and reviewed the manuscript. M. Krtička of Charles University in Prague maintains the DICEBOX statistical modeling software, and he provided important feedback on the final manuscript. B. W. Sleaford of Lawrence Livermore National Laboratory maintains the PYTHON wrappers for the DICEBOX code, which were essential during the data analysis.

4.1 Abstract

Partial γ-ray production cross sections and the total radiative thermal-neutron capture cross section for the ^{185}Re$(n, \gamma)^{186}$Re reaction were measured using the Prompt Gamma Activation Analysis facility at the Budapest Research Reactor with an enriched ^{185}Re target. The ^{186}Re cross sections were standardized using well-known ^{35}Cl$(n, \gamma)^{36}$Cl cross sections from irradiation of a stoichiometric $^{\mathrm{nat}}$ReCl$_3$

target. The resulting cross sections for transitions feeding the ^{186}Re ground state from low-lying levels below a cutoff energy of $E_c = 746$ keV were combined with a modeled probability of ground-state feeding from levels above E_c to arrive at a total cross section of $\sigma_0 = 111(6)$ b for radiative thermal-neutron capture on ^{185}Re. A comparison of modeled discrete-level populations with measured transition intensities led to proposed revisions for seven tentative spin-parity assignments in the adopted level scheme for ^{186}Re. Additionally, 102 primary γ-rays were measured, including 50 previously unknown. A neutron-separation energy of $S_n = 6179.59(5)$ keV was determined from a global least-squares fit of the measured γ-ray energies to the known ^{186}Re decay scheme. The total capture cross section and separation energy results are comparable to earlier measurements of these values.

4.2 Introduction

The Evaluated Gamma-ray Activation File (EGAF) is a coordinated research project of the International Atomic Energy Agency (IAEA) used in Prompt Gamma-ray neutron Activation Analysis (PGAA) for the determination of the elemental compositions of materials [86]. The data in the EGAF consist of capture γ-ray production cross sections (σ_γ) which were initially measured using natural elemental targets. Efforts are currently underway to improve the database using measurements on isotopically-enriched targets, e.g., Reference [8]. The methodology employed in this effort involves measurement of partial production cross sections for prompt neutron-capture γ rays using a guided thermal-neutron beam.

The total radiative thermal-neutron capture cross section σ_0 can be obtained by combining the experimental partial γ-ray production cross sections for direct population of the ground state ($\sigma_{\gamma 0}$) from low-lying levels with statistical modeling of the decay scheme to estimate the contribution of γ rays for ground-state feeding from the quasicontinuum. This method has been employed successfully with the stable palladium [87], potassium [88], gadolinium [89], and tungsten [8, 90] isotopes. Recent efforts have been focused on the actinides [91, 92].

The isotope ^{186}Re (half-life $T_{1/2} = 3.7186$ d [3]) has medical applications as a high specific-activity β^- emitter for the palliative treatment of bone metastases resulting from prostate and breast cancers [93]. For this purpose, ^{186}Re is generally produced by thermal-neutron capture on enriched ^{185}Re at reactors [94]. Medical isotope production activities involving neutron capture rely on accurate partial γ-ray production cross sections in order to calculate heating in the target and host vessel due to the local absorption of capture γ rays [95]. Independent measurements of total radiative thermal-neutron capture cross sections also add to the accuracy of existing evaluated data, used to plan the production of isotopes for patient treatment.

The object of this work is to further the effort of completing an in-depth spectroscopic study of ^{186}Re, for which the adopted level scheme data [3] in the Evaluated Nuclear Structure Data File (ENSDF) [4] includes numerous tentative spin-parity assignments and approximate level energies. Measured partial γ-ray cross sections from radiative thermal-neutron capture on an enriched ^{185}Re target, combined with statistical modeling of γ-ray cascades following neutron capture, provided an independent measurement of the total radiative thermal-neutron capture cross section for the ^{185}Re(n, γ) reaction. An independent determination of the neutron-separation energy S_n was also obtained from the observed primary γ rays in ^{186}Re. A comparison of the results from the statistical-decay model calculations to the measured γ-ray production cross-section data permitted an evaluation of the adopted decay-scheme data, e.g., spin-parity (J^π) assignments, γ-ray branching ratios, and multipole mixing ratios (δ_γ) for low-lying levels of ^{186}Re.

In addition to enriching the data contained in the EGAF, these results represent additions to the Reference Input Parameter Library (RIPL) [96], which is used to generate the Evaluated Nuclear Data File (ENDF) [9] that is employed in a variety of nuclear applications.

4.3 Experiment and Data Analysis

The experiment was performed at the Prompt Gamma Activation Analysis – Neutron Induced Prompt γ-ray Spectroscopy (PGAA-NIPS) facility at the Budapest Neutron Centre (BNC) in Budapest, Hungary, to examine the prompt γ-ray emissions from ^{186}Re following slow-neutron capture on ^{185}Re. The PGAA-NIPS facility at the BNC is positioned at the terminus of a neutron beamline extending from the 10 MW$_t$ Budapest Research Reactor. The 33.5-m beamline, constructed of 0.75-m long supermirror guide elements, provides an exceptionally low γ-ray background and a well-collimated beam of slow neutrons. The beam guide is slightly curved so that epithermal and fast neutrons, which have wavelengths less than the critical value for reflection, are not transmitted through the guide and do not reach the target. This effectively limits the flux incident on the target to thermal and cold neutrons [97]. In this experiment, neutrons were collimated prior to the target using a set of ^{6}Li-loaded polymer apertures, which defined a beam size of 2 cm × 2 cm. The total thermal-neutron flux was 1.5×10^7 neutrons cm^{-2} s^{-1}.

The high-purity germanium (HPGe) detector used at the PGAA station is an n-type closed-end coaxial detector with 27% relative efficiency, surrounded by an annular Compton-suppression shield consisting of eight bismuth germanate detector segments. The suppression shield is set in anti-coincidence mode with the HPGe detector to eliminate signals due to Compton scattering, so that the Compton background present in the resulting spectra is significantly reduced. The detector is located 23.5 cm from the center of the sample chamber, oriented at 90° to the beam direction. The detector is encased in neutron-absorbing ^{6}Li-loaded polymer sheets in order to keep the beam background low [98]. Further information about the PGAA-NIPS facility can be found in Reference [99].

The target for the experiment consisted of 150.76 mg of rhenium-metal powder enriched to 96.74% ^{185}Re. The sample was contained in a thin teflon bag, prepared according to the techniques described in Reference [100]. The sample was then aligned in an aluminum target holder, suspended by thin teflon threads, for placement in the neutron beam at an angle of 30°. Energy and efficiency calibrations of the spectrometer were performed using standard ^{133}Ba, ^{152}Eu, ^{207}Bi, ^{226}Ra, and ^{241}Am calibration sources for low energies. For energies above 1.5 MeV, samples of deuterated urea (CD_4N_2O) and polyvinyl chloride (PVC) were placed in the neutron beam, and prompt γ-rays from the $^{14}\mathrm{N}(n,\gamma)^{15}\mathrm{N}$ and $^{35}\mathrm{Cl}(n,\gamma)^{36}\mathrm{Cl}$ reactions, respectively, were used to calibrate the spectrometer [101, 102].

4.3.1 Spectroscopic Analysis.

Prompt γ-ray spectra from irradiation of the enriched ^{185}Re target were collected at two different gain settings over a 19.14-h period, and the spectra were analyzed offline using the HYPERMET-PC program [103]. A low-gain setting was used to capture the full-scale spectrum ($0 \leq E_\gamma \leq 6.5$ MeV), such that primary γ-rays up to the ^{186}Re neutron-separation energy could be identified. Representative histograms from the low-gain setting are shown in Figure 21, with a focus on the primary γ-ray peaks in the lower panel of the figure.

The high-gain setting was used to achieve improved resolution in the low-energy (≤ 1.1 MeV) region of the spectrum. This permitted fitting the large number of low-energy peaks and multiplets in the ^{186}Re spectrum. A representative portion of

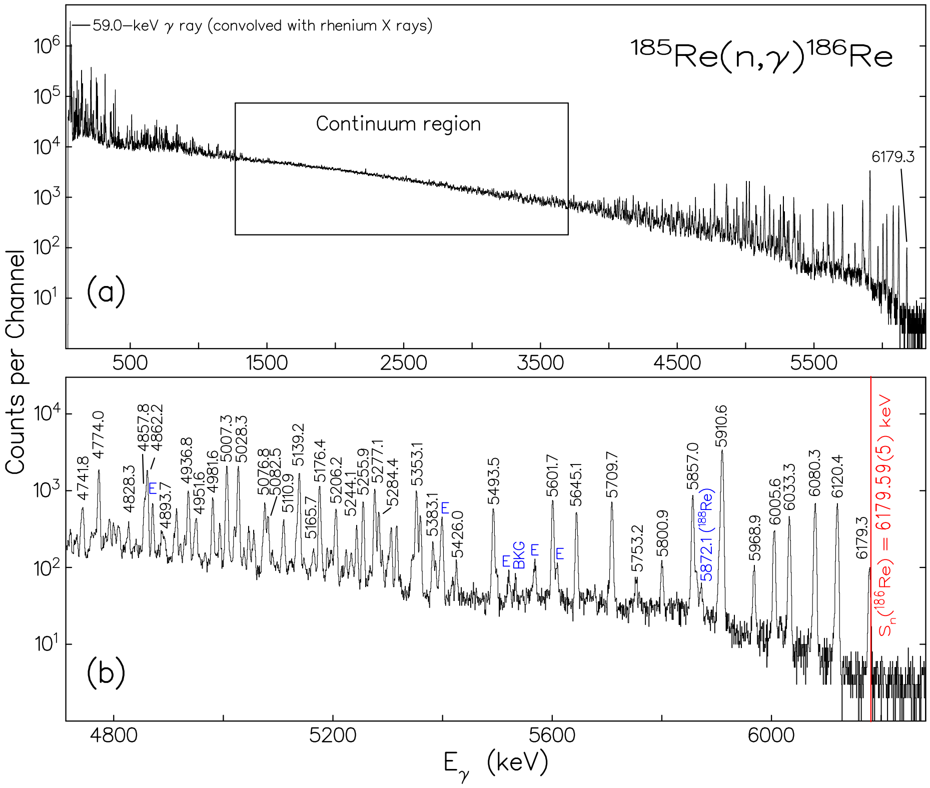

Figure 21. Representative prompt γ-ray spectra from the ^{185}Re$(n,\gamma)^{186}$Re reaction, with counts shown in logarithmic scale, measured using the low-gain setting. In (a), the entire range of γ-ray energies from ^{186}Re is shown. The peaks from the highest-intensity 59.0-keV γ ray (convolved with rhenium X rays, see Figure 22 and the text) and the 6179.3-keV primary γ ray from the capture state to the ground state are identified for orientation. The area in the center of the spectrum is the quasicontinuum region, where the level density is so high that transitions to and from levels in this region are unresolvable. In (b), an expansion of the same spectrum in the 4.7–6.5 MeV energy region is shown, in which the majority of primary γ rays were fitted. The highest-intensity primary γ rays from ^{186}Re are labeled in black, while escape peaks (E), background (BKG), and contaminant γ rays from neutron capture on ^{188}Re are identified in blue. The ^{186}Re neutron separation energy $S_n = 6179.59(5)$ determined in this work is identified with a red vertical line.

the high-gain spectrum is shown in Figure 22 with peak fits from HYPERMET-PC. Fitting the particular region shown in the figure was problematic. The 59.0-keV γ ray is the highest-intensity γ ray in the ^{185}Re(n,γ) spectrum, and after correcting for internal conversion it contributes over 80% to the total radiative-capture cross section σ_0, so it was essential that the peak intensity was properly fitted. However, the 59.0-keV γ ray peak is convolved with the 59.7- and 61.1-keV rhenium K_α

X rays. The fit of this multiplet was adjusted until the ratio of the intensities for the 59.7- and 61.1-keV K_α X rays was 0.584(13), which matched the ratio 0.584(18) from the X-ray yields in Reference [10]. The close agreement between these ratios gave a high degree of confidence in the fitted intensity ascribed to the 59.0-keV γ-ray peak.

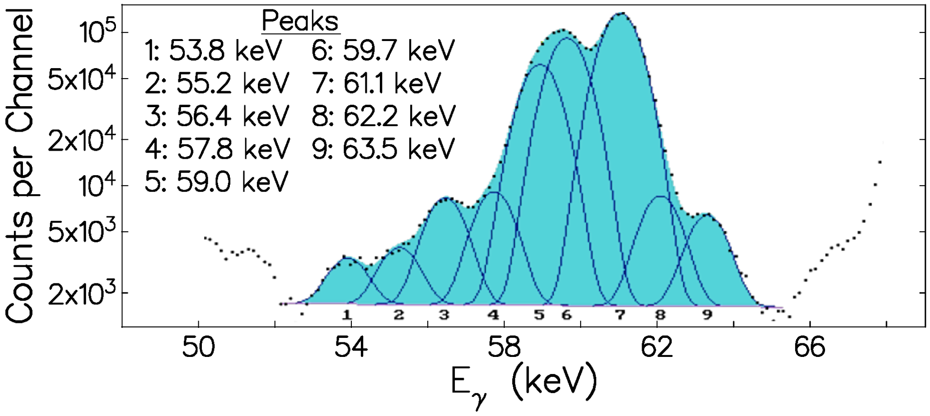

Figure 22. Representative section of the prompt γ-ray spectrum using the high-gain setting to show the quality of the fits performed using HYPERMET-PC. Black dots identify the experimental counts in logarithmic scale, while the shaded region is the result of the least-squares fit, and solid blue lines identify the fits of each peak in the 52- to 65-keV energy range.

4.3.2 Cross-Section Standardization.

Measurement of peak areas in the prompt neutron-capture γ-ray spectra from the enriched ^{185}Re target, corrected for detector efficiency and γ-ray attenuation in the target, provided γ-ray intensities for transitions in ^{186}Re. For these transitions, the partial cross sections σ_γ were determined by standardizing to the known $^{35}\mathrm{Cl}(n,\gamma)$ comparator cross sections $\sigma_{\gamma,c}$ from References [104, 105], listed in Table 3. Analysis of a spectrum from the irradiation of a stoichiometric $^{\mathrm{nat}}\mathrm{ReCl}_3$ target permitted determination of partial cross sections $\sigma_{\gamma,x}$ for a few strong prompt γ rays from the $^{\mathrm{nat}}\mathrm{Re}(n,\gamma)$ reaction using the relation

$$\frac{\sigma_{\gamma,x}}{\sigma_{\gamma,c}} = \frac{n_x}{n_c}\frac{A_{\gamma,x}/\epsilon(E_{\gamma,x})}{A_{\gamma,c}/\epsilon(E_{\gamma,c})}. \tag{37}$$

In Equation (37), $A_{\gamma,x}$ and $A_{\gamma,c}$ are the peak areas of the unknown and comparator γ rays, respectively, $\epsilon(E_{\gamma,x})$ and $\epsilon(E_{\gamma,c})$ are the detector efficiencies at the γ-ray energies $E_{\gamma,x}$ and $E_{\gamma,c}$, and the known $3:1$ stoichiometry of the target compound implies $(n_x/n_c) = {}^1\!/_3$ [106]. The ${}^{\mathrm{nat}}\mathrm{Re}(n,\gamma)$ cross sections obtained using Equation (37) were then corrected for isotopic abundance (${}^{\mathrm{nat}}\mathrm{Re}$ comprises 37.398% ${}^{185}\mathrm{Re}$ and 62.602% ${}^{187}\mathrm{Re}$ [1]) to arrive at isotopic ${}^{185}\mathrm{Re}(n,\gamma)$ cross sections. These ${}^{185}\mathrm{Re}(n,\gamma)$ cross sections were then used as standards for normalizing the intensities of all prompt γ rays obtained from the enriched ${}^{185}\mathrm{Re}$ spectrum (Figure 21).

4.3.3 Determination of Effective Target Thickness.

Rhenium metal has a density of 21.02 g/cm^3, and therefore has a large photon attenuation cross section for γ rays with energies below 300 keV. As a result, partial cross sections for low-energy γ rays must be corrected for self-absorption within the target mass during standardization. Because the target sample is of nonuniform thickness, it is difficult to accurately describe its geometry using particle-transport simulations. An alternative method involves comparing partial cross sections for low-energy γ rays, corrected for attenuation using an effective target thickness, with reference values obtained from irradiation of an optically-thin target sample. By adjusting the effective thickness to minimize the residual errors between the thick-target cross sections and the reference cross sections from the thin target, an effective thickness for the enriched ${}^{185}\mathrm{Re}$ target can be found that can be used to calculate the attenuation at any γ-ray energy [107].

To determine the effective thickness of the enriched ${}^{185}\mathrm{Re}$ target, a prompt γ-ray spectrum from irradiation of a lower-density hydrated rhenium chloride sample [106] was measured. The density of this sample was such that γ-ray self-absorption within the material was minimal and could be neglected. The comparator cross sections from ^{35}Cl(n,γ) in Table 3 were used to standardize the ^{185}Re(n,γ) cross sections using Equation (37). Standard partial cross sections (σ_γ^S) for the four strong, well-resolved γ-ray transitions in ^{186}Re listed in Table 3 were extracted and compared with the cross sections for the same γ rays obtained from the thick enriched ^{185}Re target (σ_γ^T).

Table 3. Elemental comparator cross sections $\sigma_{\gamma,c}$ for ^{35}Cl(n,γ) from References [104, 105] used in the analysis of the prompt γ-ray spectrum from ^{nat}ReCl$_3(n,\gamma)$ to determine standard isotopic ^{185}Re(n,γ) cross sections σ_γ^S, also listed.

Source (isotope; reaction)	E_γ (keV)	$\sigma_{\gamma,c}$, σ_γ^S (b)
^{36}Cl; ^{35}Cl(n,γ)	517.1	7.58(5)
^{36}Cl; ^{35}Cl(n,γ)	788.4	5.42(5)
^{36}Cl; ^{35}Cl(n,γ)	1164.9	8.91(4)
^{36}Cl; ^{35}Cl(n,γ)	1951.1	6.33(4)
^{36}Cl; ^{35}Cl(n,γ)	5715.2	1.820(16)
^{186}Re; ^{nat}ReCl$_3(n,\gamma)$	103.3	1.34(8)
^{186}Re; ^{nat}ReCl$_3(n,\gamma)$	214.7	6.6(4)
^{186}Re; ^{nat}ReCl$_3(n,\gamma)$	255.0	3.19(19)
^{186}Re; ^{nat}ReCl$_3(n,\gamma)$	391.0	3.27(6)

For a given γ ray produced in the target with intensity I_0, measured at the detector with intensity I_γ, the γ-ray attenuation factor is given by I_γ/I_0. The attenuation factor depends on the γ-ray energy E_γ and the target thickness t, and is obtained by integrating the exponential-attenuation law $I_\gamma/I_0 = \exp\left(-\mu_\gamma x\right)$ over the depth x to arrive at the expression

$$\frac{I_\gamma(E_\gamma,t)}{I_0} = \frac{\cos\theta}{t\rho\left(\frac{\mu_\gamma}{\rho}\right)_{E_\gamma}} \cdot \left[1 - \exp\left(\frac{-t\rho\left(\frac{\mu_\gamma}{\rho}\right)_{E_\gamma}}{\cos\theta}\right)\right]. \tag{38}$$

In Equation (38), $(\mu_\gamma/\rho)_{E_\gamma}$ is the γ-ray mass-attenuation coefficient at the γ-ray energy E_γ, ρ is the target sample density, and θ is the angle at which the sample face is oriented relative to the detector face [86, 107]. In the experiment described in this work, $\theta = 30°$, and mass-attenuation coefficients used in the calculations were taken from the XMUDAT database [108]. After correcting for attenuation and detector efficiency, the peak areas $A_{\gamma,x}$ from the thick target should be directly proportional to the thin-target standard cross sections σ_γ^S, i.e., the following relation should hold for all E_γ for a constant C :

$$\frac{\sigma_\gamma^S}{A_{\gamma,x}/\epsilon(E_{\gamma,x})} \cdot \frac{I_\gamma(E_\gamma, t)}{I_0} = C. \tag{39}$$

The effective sample thickness t for the enriched ^{185}Re target in Equation (39) was varied until C converged to a unique value for the 103.3-, 214.7-, 255.0-, and 391.0-keV γ rays. The errors about the mean value of C for each thickness were analyzed using the χ^2-minimization procedure outlined by Hurst *et al.* in Reference [107]. Two parameters, the thickness t and a global correlation coefficient (see Reference [107] for details), were adjusted to minimize the χ^2 to fit the four data points, leaving two degrees of freedom (ndf $= 2$). A plot of the χ^2 values as a function of thickness t is shown in Figure 23, where it is evident that the minimum (χ^2_{min}) is achieved at an effective thickness of $t = 0.086$ mm. The 1σ-uncertainty range for a 2-parameter adjustment is defined by $\chi^2_{\text{min}} + 2.3$ [109], which results in an uncertainty of ± 0.008 mm in the effective thickness.

The ratio of the partial cross sections from the attenuated thick-target sample, σ_γ^T, to the unattenuated thin-target values σ_γ^S, yields an experimental attenuation factor:

$$\left(\frac{I_\gamma}{I_0}\right)_{\text{exp}} = \frac{\sigma_\gamma^T}{\sigma_\gamma^S}. \tag{40}$$

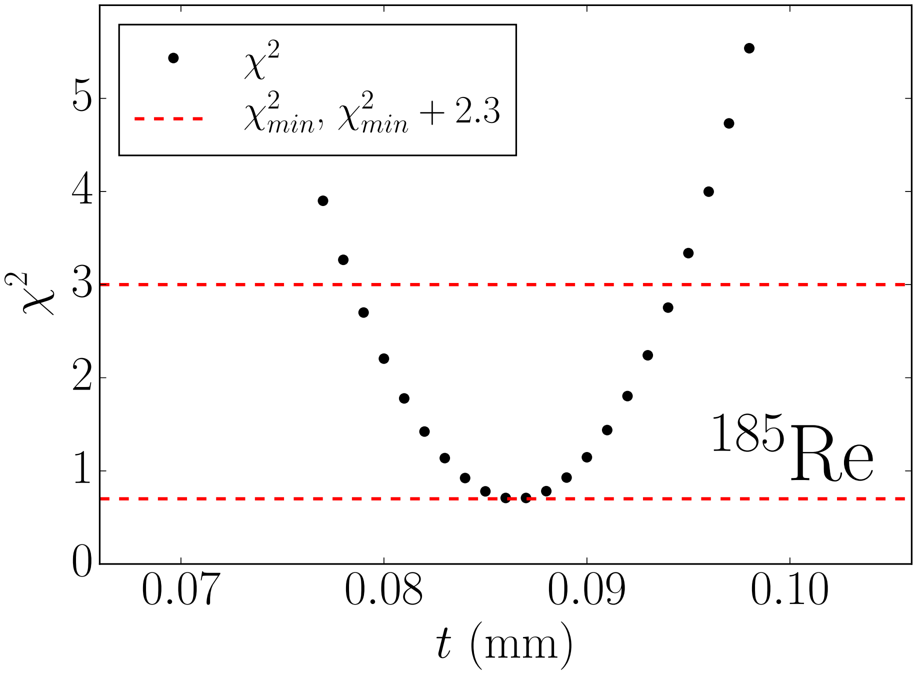

Figure 23. Plot of the global χ^2 values as a function of target thickness for the enriched ^{185}Re sample. The lower dashed-red line corresponds to the minimum of the global χ^2 distribution, which occurs at an effective thickness of 0.086 mm. The upper dashed-red line is drawn at $\chi^2_{\mathrm{min}} + 2.3$, which defines the 1σ range of $[0.078\ \mathrm{mm}, 0.094\ \mathrm{mm}]$ of acceptable t values for two adjustable parameters [109].

To illustrate the effectiveness of the χ^2-minimization procedure at producing an accurate effective thickness, the experimental attenuation factors $(I_\gamma/I_0)_{\mathrm{exp}}$ for comparator and other low-energy ^{186}Re γ rays were compared against the attenuation factors calculated using Equation (38) with an assumed thickness of $t = 0.086$ mm, with the same calculations performed at thicknesses of 0.078 mm and 0.094 mm to obtain the $\pm 1\sigma$ uncertainty band. The good agreement in the resulting plot, shown in Figure 24, validates the effective thickness found for the enriched ^{185}Re target. The calculated attenuation factors were used to correct the ^{185}Re(n, γ) cross sections obtained using Equation (37) at all γ-ray energies. Uncertainties in the attenuation factors were propagated through the calculations of the γ-ray production cross sections presented in this work.

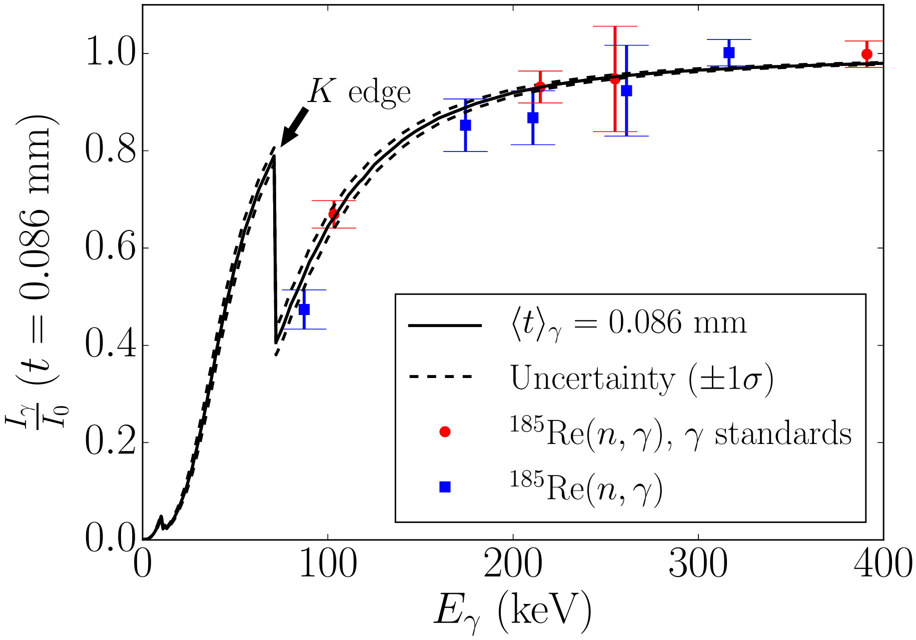

Figure 24. Plot of the attenuation factor I_γ/I_0 at an effective thickness of 0.086 mm (solid black line with dashed lines indicating uncertainty) with the experimental ratios of thick-target partial cross sections to thin-target partial cross sections, $\sigma_\gamma^T/\sigma_\gamma^S = (I_\gamma/I_0)_{\mathrm{exp}}$. The data points identified by red circles are for the well-resolved 103.3-, 214.7-, 255.0-, and 391.0-keV γ rays, which were used as standards to determine the effective thickness. Shown for comparison are the 87.2-, 174.3-, 210.7-, 261.2-, and 316.6-keV γ-ray transitions in ^{186}Re (blue-square data points), which are not as well-resolved in the spectra and could not be used for determining the effective thickness.

4.4 Statistical Modeling

A significant portion of the results presented in this work is based on a combination of experimental results with simulations of γ decay following thermal-neutron capture, based on a statistical model of the nucleus. The Monte-Carlo statistical-decay code DICEBOX [52], which assumes a generalization of the extreme statistical model of compound nucleus formation and decay [46], was used for these simulations.

To model the thermal-neutron capture cascade, DICEBOX simulates numerous (n, γ) decay-scheme simulations, known as nuclear realizations. Each realization is based on a statistical model of the level density $\rho(E, J, \pi)$ and γ-ray transition widths Γ_{if} for the formation and decay of the compound nucleus. To describe the decay scheme, all level energies, spin-parity assignments, and depopulating γ rays below a user-defined cutoff excitation energy (referred to as the critical energy E_c) are taken from the experimental-decay scheme. For levels in the quasicontinuum, defined in this case as the levels above E_c, the code generates a random set of levels according to an *a priori* assumed model of the level density (LD). Transitions to and from these levels to low-lying levels below E_c are randomly generated according to an *a priori* assumed model of the photon strength function (PSF), where angular-momentum selection rules are applied to determine allowed transitions. The PSFs, $f^{(XL)}(E_\gamma)$, for transitions with multipolarity $X = E$ (electric) or M (magnetic) and multipole order L, are used to describe statistical γ decay. For allowed transitions, the partial radiation widths Γ_{if}^{XL} of the transition probabilities from initial state i to final state f are assumed to follow a Porter-Thomas distribution [110]

$$P(x) = \frac{1}{\sqrt{2\pi x}} e^{-x/2}, \tag{41}$$

where $x = \Gamma_{if}^{XL} / \langle \Gamma_{if}^{XL} \rangle$, and the mean value $\langle \Gamma_{if}^{XL} \rangle$ is given by

$$\langle \Gamma_{if}^{XL} \rangle = \frac{f^{(XL)}(E_\gamma) \cdot E_\gamma^{2L+1}}{\rho(E_i, J_i, \pi_i)}. \tag{42}$$

Here $\rho(E_i, J_i, \pi_i)$ is the level density at an initial state E_i characterized with a spin-parity $J_i^{\pi_i}$ [111]. Gamma-ray transition probabilities are corrected for internal conversion using coefficients calculated with the Band-Raman Internal Conversion Calculator (BrIcc) version 2.3S code [28, 29]. Primary γ rays (i.e., those that originate at the capture state) feeding discrete levels below E_c are also taken from experiment. In order to obtain accurate probabilities of populating discrete levels below E_c with uncertainties (due to statistical Porter-Thomas fluctuations) small enough for comparison with experimental cross sections, 50 nuclear realizations were simulated for each PSF/LD model combination, with 100,000 γ-ray cascades simulated per realization [90].

4.4.1 Level Densities.

The nuclear-level density models used in this work were assumed to be functions of excitation energy E, spin J, and parity π, with the general form

$$\rho(E, J, \pi) = \rho(E) f(J) \pi(E), \tag{43}$$

where $\rho(E)$ is the total level density at excitation energy E, $f(J)$ is a spin-distribution factor, and $\pi(E)$ is the parity distribution identifying the fraction of positive- or negative-parity states as a function of excitation energy. Two different $\rho(E, J) = \rho(E) f(J)$ models were considered in the statistical-model calculations, the constant temperature formula (CTF) [112] and the backshifted Fermi gas (BSFG) models [112, 113].

The CTF LD model assumes a constant nuclear temperature T, and is given by

$$\rho(E, J) = \frac{f(J)}{T} \exp\left(\frac{E - E_0}{T}\right), \tag{44}$$

where E_0 is an energy backshift related to the nucleon pairing energy. The spin-distribution factor $f(J)$ is

$$f(J) = \frac{2J+1}{2\sigma_c^2} \exp\left[-\frac{(J+1/2)^2}{2\sigma_c^2}\right], \tag{45}$$

where σ_c is a spin cutoff factor. For a nucleus with mass number A, the formula $\sigma_c = 0.98A^{0.29}$ was adopted for the spin cutoff factor in the CTF LD model [114].

The BSFG LD model assumes the nucleus to be a two-component fermionic fluid, which leads to the expression

$$\rho(E,J) = f(J)\frac{\exp\left[2\sqrt{a(E-E_1)}\right]}{12\sqrt{2}\sigma_c a^{1/4}(E-E_1)^{5/4}}, \tag{46}$$

where E_1 is an energy backshift. The spin-cutoff factor σ_c for the BSFG model was taken as

$$\sigma_c^2 = 0.0146A^{5/3}\frac{1+\sqrt{1+4a(E-E_1)}}{2a}, \tag{47}$$

and a is a shell-model level-density parameter [114].

The parameters T, E_0, a, and E_1 in Equations (44), (46), and (47) were assumed to follow the parameterizations of von Egidy and Bucurescu in References [114] or [115], and are listed in Table 4.

Table 4. Level density parameters for the CTF (T and E_0) and BSFG (a and E_1) models used in statistical-model calculations to model γ-ray cascades in ^{186}Re. The parameters were taken to be the mean values quoted from the respective references.

Reference	T (MeV)	E_0 (MeV)	a (MeV^{-1})	E_1 (MeV)
[114]	0.56(1)	−1.76(18)	19.87(28)	−0.90(10)
[115]	0.54(1)	−1.59(15)	18.19(25)	−0.82(8)

We tested both a parity-independent ($\pi(E) = 1/2$) LD model as well as a LD model slightly dependent on parity at low excitation energies, described by Al-Quraishi *et al.* in Reference [116]. In the parity-dependent LD model, the function $\pi(E)$ is a Fermi-Dirac distribution describing the fraction of positive- or negative-parity states (depending on the sign used in the distribution function) as a function of E. The functional form for $\pi(E)$ is

$$\pi(E) = \frac{1}{2}\left(1 \pm \frac{1}{1+\exp\left[c(E-\delta_p)\right]}\right), \tag{48}$$

where the sign of the ± is determined from the parity of the ground state, c is a spin-cutoff factor, and δ_p is an energy shift. For ^{186}Re, when $\pi(E)$ represents the distribution of positive-parity states, a negative sign is used in Equation (48) to signify that low-energy levels have predominantly negative parity. For the statistical-model calculations, we assumed the parameterization $\delta_p = -0.1814$ MeV and $c = 3.0$ MeV^{-1} from Reference [116].

4.4.2 Photon Strength Functions.

For the transitions relevant to the statistical modeling of thermal-neutron capture γ-ray cascades, the $E1$ PSF (which dominates γ decay for $E_\gamma \geq 4$ MeV) is believed to be described by the low-energy tail of the giant dipole electric resonance (GDER). Above $E_\gamma \approx 8$ MeV, the shape of the $E1$ PSF can be probed using (γ, n) measurements. At these higher energies, the shape of the $E1$ PSF for deformed nuclei is usually well-described by a sum of two standard Lorentzians, sometimes known as the Brink-Axel (BA) model [117, 118]. At γ-ray energies below ~8 MeV, the shape of the $E1$ PSF is not well known, and several extrapolations of the BA model are typically used. In addition to the BA model, we tested the Kadmenski, Markushev, and Furman (KMF) [119], generalized Lorentzian (GLO) [120], and modified generalized Lorentzian (MGLO) [121] models for the $E1$ PSF in this work.

The Brink-Axel function $f_{\mathrm{BA}}^{(E1)}(E_\gamma)$ for the $E1$ PSF in deformed nuclei is a sum of two standard Lorentzians, corresponding to vibration modes along and perpendicular to the nuclear-symmetry axis:

$$f_{\mathrm{BA}}^{(E1)}(E_\gamma) = \frac{1}{3(\pi\hbar c)^2} \sum_{i=1}^{2} \frac{\sigma_{G_i} E_\gamma \Gamma_{G_i}^2}{(E_\gamma^2 - E_{G_i}^2)^2 + E_\gamma^2 \Gamma_{G_i}^2}. \tag{49}$$

The parameters E_{G_i} and Γ_{G_i} represent the resonant energies and widths of the GDER vibration modes, and the σ_{G_i} are the resonance cross sections. These values

Table 5. Resonance parameters for the GDER and GQER used in statistical-model calculations to model γ-ray cascades in ^{186}Re. The GDER parameters are from Reference [123], and the GQER parameters are from a theoretical global parameterization for isovector-isoscalar vibrations described in the text.

Resonance	E_{G_1} (MeV)	Γ_{G_1} (MeV)	σ_{G_1} (mb)	E_{G_2} (MeV)	Γ_{G_2} (MeV)	σ_{G_2} (mb)
GDER	12.63	2.77	279	15.24	4.69	375
GQER	11.04	3.88	4.64	-	-	-

are tabulated in the RIPL [96] for a variety of stable isotopes, and the systematics are such that the parameter values are relatively constant for nuclei with similar deformation in a given mass region. In our case we adopted values obtained from a least-squares fit of $^{\mathrm{nat}}$Re photoabsorption data [122] over the interval $10.8 - 18.8$ MeV [123]. The resulting GDER parameters, listed in Table 5, are adopted in the RIPL [96] and were used in the statistical-model calculations described in this work.

The BA model is dependent on E_γ alone, while other $E1$ PSF models considered in this work (KMF, GLO, MGLO) also include an additional temperature dependence, due to the inclusion of a temperature-dependent resonance width given by

$$\Gamma_{G_i}(E_\gamma, \Theta) = \frac{\Gamma_{G_i}}{E_{G_i}^2}\left(E_\gamma^2 + 4\pi^2\Theta^2\right). \tag{50}$$

In Equation (50) the nuclear temperature Θ is a function of the excitation energy E_f of the final state, level density parameter a from Reference [114], and a pairing energy Δ:

$$\Theta = \sqrt{(E_f - \Delta)/a}. \tag{51}$$

The pairing energy is determined for odd-odd nuclei via the formula $\Delta = -0.5|P_d|$, where P_d is the deuteron-pairing energy found in Reference [114]. For ^{186}Re,

$P_d = -1.492$ MeV and $\Delta = -0.796$ MeV.

For deformed nuclei, the KMF model of the $E1$ PSF is given by the equation

$$f^{(E1)}_{\mathrm{KMF}}(E_\gamma, \Theta) = \frac{1}{3(\pi\hbar c)^2} \sum_{i=1}^{2} F_K \frac{\sigma_{G_i}\Gamma_{G_i} E_\gamma \Gamma_{G_i}(E_\gamma, \Theta)}{(E_\gamma^2 - E_{G_i}^2)^2}, \tag{52}$$

where the dimensionless Fermi liquid parameter F_K is taken to have a value of 0.7 [124] in this work.

An empirical model, connecting the KMF at low E_γ with the BA model near the GDER maximum was proposed by Kopecky and Uhl in Reference [120]. This model, called the GLO, has the functional form

$$f^{(E1)}_{\mathrm{GLO}}(E_\gamma, \Theta) = \sum_{i=1}^{2} \frac{\sigma_{G_i}\Gamma_{G_i}}{3(\pi\hbar c)^2} \left[F_K \frac{4\pi^2\Theta^2\Gamma_{G_i}}{E_{G_i}^5} + \frac{E_\gamma \Gamma_{G_i}(E_\gamma, \Theta)}{(E_\gamma^2 - E_{G_i}^2)^2 + E_\gamma^2 \Gamma_{G_i}^2(E_\gamma, \Theta)} \right], \tag{53}$$

with terms as defined in the BA and KMF models above.

A generalization of the GLO model to describe deformed nuclei was later proposed by Kopecky *et al.* in Reference [125]. This model, referred to as the enhanced generalized Lorentzian (EGLO), includes an enhanced resonance width

$$\Gamma'_{G_i}(E_\gamma, \Theta) = \left[k_0 + (1 - k_0) \frac{E_\gamma - E_0}{E_{G_i} - E_0} \right] \Gamma_{G_i}(E_\gamma, \Theta), \tag{54}$$

where the energy shift $E_0 = 4.5$ MeV [125], and the parameter k_0 can be adjusted to achieve optimum agreement with the experimental photoabsorption cross-section data. The MGLO model [121] considered in this work modifies the behavior of the EGLO [125] at low γ-ray energies, and is obtained from Equation (53) by replacing the temperature-dependent resonance width $\Gamma_{G_i}(E_\gamma, \Theta)$ in Equation (50) with the enhanced resonance width from Equation (54).

The four $E1$ PSF models considered in this work are shown in Figure 25 with the (γ, n) data from Reference [122]. As evident, the KMF and GLO models (which were originally proposed for spherical nuclei) do not reproduce the (γ, n) data in the range $8 \leq E_\gamma \leq 10$ MeV. On the other hand, an enhancement of $k_0 = 2.9$ in the

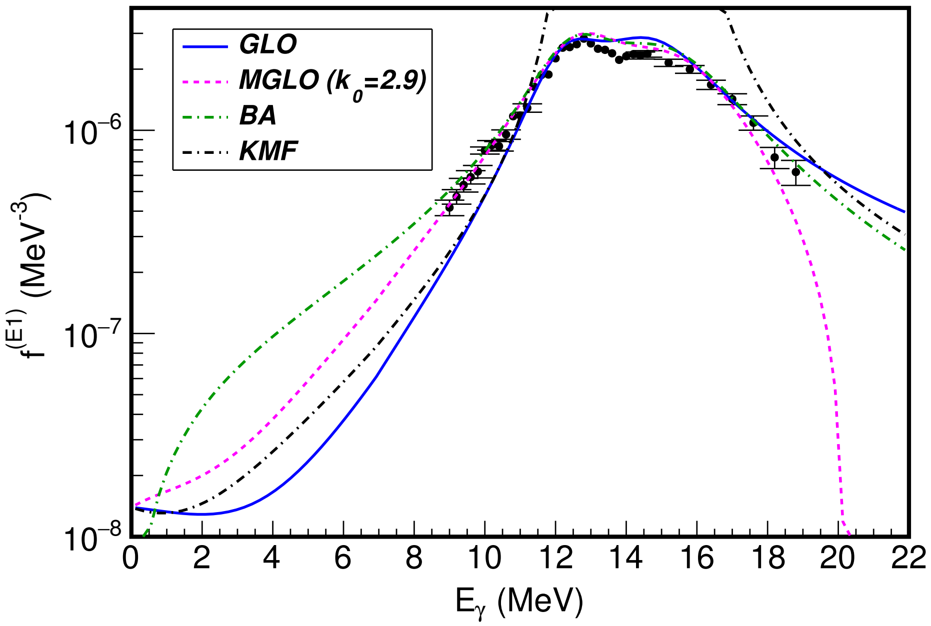

Figure 25. Experimental (γ, n) data from Reference [122] overlaid with the BA, GLO, MGLO, and KMF models for the $E1$ PSF for transitions from the capture state. The resonance parameters used in each model are from Reference [123]. The value of 2.9 for the enhancement factor k_0 in the MGLO model was chosen based on the observed agreement between the MGLO and the experimental cross-section data in the low-energy tail of the GDER.

MGLO model results in a good fit to the experimental photoabsorption data in the low-energy tail of the GDER. For this reason, we assumed an enhancement factor of 2.9 for all calculations in which the MGLO model was used for the $E1$ PSF.

The single-particle (SP) model for the $M1$ PSF was adopted in this work. Statistical-decay modeling of the tungsten isotopes ^{183,185,187}W, similar in mass to ^{186}Re, found that a value of $f_{SP}^{(M1)} = 1 \times 10^{-9}$ MeV^{-3} produced the best agreement between the predictions of the statistical model and the experimental cross sections and total radiative capture width [8]. The same effect was observed for ^{186}Re, so a SP strength of 1×10^{-9} MeV^{-3} was adopted for the calculations in this work. The scissors model [126] for the $M1$ PSF was also considered in this work. Due to the relative insignificance of $M1$ transitions in the statistical-model calculations, the scissors model produced results that were consistent with those of the SP model.

The contribution of $E2$ transitions is much smaller than that of dipole transitions. The GQER model, which uses a standard Lorentzian (SLO) with a single resonance to describe an isovector-isoscalar quadrupole vibration, was used for the $E2$ PSF:

$$f_{\mathrm{SLO}}^{(E2)}(E_\gamma) = \frac{1}{5(\pi\hbar c)^2} \frac{\sigma_{G_1} E_\gamma \Gamma_{G_1}^2}{(E_\gamma^2 - E_{G_1}^2)^2 + E_\gamma^2 \Gamma_{G_1}^2}. \tag{55}$$

The resonance parameters E_{G_1}, Γ_{G_1}, and σ_{G_1} for the GQER that were used in the statistical-model calculations in this work are listed in Table 5. These values were calculated using the following global parameterization: $E_{G_1} = 63A^{-1/3}$ [127], $\Gamma_{G_1} = 6.11 - 0.012A$ [128], and $\sigma_{G_1} = 1.5 \times 10^{-4} \frac{Z^2 E_{G_1}^2 A^{-1/3}}{\Gamma_{G_1}}$ [128].

The strengths of $M2$ and higher-multipole transitions are expected to be negligible in the statistical-decay modeling, and were not considered in modeling the neutron-capture γ cascade in this work.

4.4.3 Calculation of the Total Radiative Thermal-neutron Capture Cross Section.

Dicebox models the contribution to the total (n, γ) cross section from the quasicontinuum, and calculates the probability per neutron capture of direct feeding of the ground state from the quasicontinuum (P_0). The total radiative-capture cross section σ_0 is obtained by combining this contribution with the experimentally-measured partial γ-ray production cross sections from discrete levels below E_c feeding the ground state directly $(\sigma_{\gamma 0})$, using the expression

$$\sigma_0 = \sum \sigma_{\gamma 0}^{\mathrm{exp}} + \sum \sigma_{\gamma 0}^{\mathrm{sim}} = \frac{\sum \sigma_{\gamma 0}^{\mathrm{exp}}}{1 - P_0}. \tag{56}$$

In Equation (56), the superscripts ‘exp’ and ‘sim’ refer to the experimental and simulated cross sections, corrected for internal conversion, directly feeding the ground state from the discrete levels below E_c and from the quasicontinuum, respectively [8].

4.5 Results and Discussion

Partial γ-ray production cross sections for 106 γ rays deexciting and feeding 48 discrete levels from the adopted level scheme (Reference [3]) up to an excitation energy of 864.7 keV are listed in Table 6, along with 102 primary γ rays feeding levels from References [3, 63]. Gamma rays were placed in the ^{186}Re level scheme by matching the fitted peak energies from the prompt γ-ray spectrum with the energies of known transitions in the ENSDF [3]. Due to the high level density of ^{186}Re, peaks in the singles γ-ray spectra were often convolved in multiplets, which made direct measurement of the γ-ray intensities difficult. In these cases, identified by footnotes in Table 6, statistical-model calculations (for γ rays deexciting levels below $E_c = 746$ keV) or branching ratios from the ENSDF [3] were used to normalize the cross sections.

Production cross sections for multiply-placed γ rays for which the ENSDF provides only the undivided intensity [3], identified by footnotes in Table 6, were determined by dividing the total γ-ray intensity as necessary to optimize agreement between the level population from the statistical model and the experimental depopulation ($\sum_i \sigma_{\gamma_i}(1+\alpha_i)/\sigma_0$; where the summation is over all γ rays depopulating a given level). For the 218.1-, 228.6-, 193.8-, and 469.4-keV γ rays deexciting the 317.8-, 646.3-, 691.4, and 785.5-keV levels, respectively [3], the intensity resulting from this procedure was sufficiently small that there was no strong evidence for the existence of these γ rays on the basis of statistical-model results. These four γ rays are omitted from Table 6. The highly-internally-converted ($\alpha \approx 4.1 \times 10^6$) 50-keV γ ray [3] deexciting the 148.2-keV, $J^\pi = (8)^+$ isomer [22], and the 142.8-keV γ ray reported in the ENSDF as deexciting the 997.8-keV level [3] were not observed in the prompt γ-ray spectrum and are also omitted from Table 6.

Level spin-parity (J^π) assignments, transition multipolarities (XL) and multipole mixing ratios (δ_γ) in Table 6 were taken from the ENSDF [3] when available, while internal-conversion coefficients (α) were calculated with BrIcc [28]. Unknown transition multipolarities between levels with definite J^π assignments were assumed to be the lowest multipole order permitted by angular-momentum selection rules. It is important to note that many of these transitions may have mixed-multipole character, but the effect of multipole mixing on internal-conversion-corrected γ-ray production cross sections used in the statistical model is negligible for higher-energy ($E_\gamma > 250$ keV) transitions. For lower-energy ($E_\gamma \leq 250$ keV) γ-ray transitions, level populations calculated using the statistical model can be used to estimate multipole mixing ratios, discussed later in the text.

Gamma-ray transitions with $E_\gamma \gtrsim 3.5$ MeV were assumed to be primary γ-ray transitions, and were identified as such in Table 6 provided they satisfied the following criterion for a known level with excitation energy E_f:

$$S_n = E_\gamma + E_f + E_r. \tag{57}$$

Here S_n is the neutron-separation energy, E_γ is the measured γ-ray energy, and $E_r = E_\gamma^2/2A$ is the recoil energy of the nucleus (A is the atomic mass of the product nucleus). Of the primary transitions identified in this way, 50 were not previously reported in the evaluated literature (References [21, 60, 61, 62]). Of these 50 new primary transitions, 35 feed levels in the adopted level scheme for ^{186}Re [3]. The remaining 15 primary γ rays feed levels reported by Wheldon *et al.* in

Reference [63], in which levels in ^{186}Re were populated by (p, d) reactions on ^{187}Re at proton energies of 21 MeV. New primary γ rays are identified by footnotes in Table 6, with multipolarity assignments estimated on the basis of observed γ-ray intensities relative to the intensities of primary transitions with known multipolarity. The highest-intensity primary transition with $M1$ multipolarity (assumed from angular momentum selection rules), has an intensity of $\sigma_\gamma = 0.024(4)$ b, so primary transitions with $\sigma_\gamma \geq 0.03$ b that feed levels without a definite J^π assignment are given tentative multipolarities of $E1$, or tentative $E1$ or $M1$ multipolarity if $\sigma_\gamma < 0.03$ b.

Table 6. Experimental thermal-neutron capture partial γ-ray production cross sections σ_γ from the ^{185}Re(n,γ) reaction. Spin-parity assignments $J_{i,f}^{\pi_{i,f}}$ were taken from the ENSDF adopted levels for ^{186}Re [3], except those values in bold, which are proposed in this work on the basis of statistical-decay modeling results. Transition multipolarities XL are from the ENSDF [3], with those identified with square brackets assumed from angular-momentum selection rules and the values proposed in this work in bold text. Tentative values are identified with parentheses. Level excitation energies $E_{i,f}$ were obtained from a least-squares fit to the γ-ray energies E_γ measured in this work, unless otherwise noted. Internal conversion coefficients α were calculated using BrIcc [28] using the mean or limiting values of the mixing ratios δ_γ taken from the ENSDF [3], unless otherwise noted.

E_i (keV)	$J_i^{\pi_i}$	E_f (keV)	$J_f^{\pi_f}$	E_γ (keV)	σ_γ (b)	α	XL	δ_γ
0.0	1^-							
59.007(6)	2^-	0.0	1^-	58.987(6)	17.5(11)	4.14	$M1$	
99.381(7)	3^-	59.007(6)	2^-	40.364(7)^a	2.2(5)	15.59	$M1+E2$	0.11(2)
		0.0	1^-	99.449(11)	0.47(9)	4.21	$E2$	
146.227(9)	3^-	59.007(6)	2^-	87.199(8)^b	2.38(14)	7.66	$M1$	
		0.0	1^-	146.57(16)^a	0.20(4)	0.95	$[E2]$	
174.059(11)	4^-	99.381(7)	3^-	74.685(11)^c	0.95(7)	11.96	$M1+E2$	0.19(6)
∼186	6^-	174.059(11)	4^-	$(\sim12)^{d,i}$	$\leq 7\times10^{-5}$	7.1×10^4	$[E2]$	
		148.2(5)^f	8^+	$(\sim38)^{d,i}$	$\leq 5\times10^{-3}$	1.0×10^3	$[M2]$	
210.722(10)	2^-	146.227(9)	3^-	64.42(4)^{d,e}	0.051(9)	3.20	$[M1]$	
		99.381(7)	3^-	111.16(8)^a	1.28(18)	3.82	$M1$	
		59.007(6)	2^-	151.722(14)	2.45(14)	0.84	$E2(+M1)$	
		0.0	1^-	210.705(23)	3.05(18)	0.58	$M1(+E2)$	≤ 0.39
268.729(12)	4^-	146.227(9)	3^-	122.519(12)	1.82(13)	2.89	$[M1]$	
		99.381(7)	3^-	169.46(3)^a	0.36(9)	0.78	$E2(+M1)$	≥ 1.3
		59.007(6)	2^-	209.78(4)	0.41(4)	0.27	$[E2]$	
273.566(12)	4^-	174.059(11)	4^-	99.449(11)^a	0.30(7)	5.25	$[M1]$	
		146.227(9)	3^-	127.354(16)^a	0.76(17)	1.84	$M1+E2$	$1.8(^{+86}_{-7})$
		99.381(7)	3^-	174.31(3)	1.11(7)	0.74	$M1+E2$	$1.2(^{+7}_{-4})$
313.989(12)	3^+	210.722(10)	2^-	103.290(12)	1.34(8)	0.35	$[E1]$	
		146.227(9)	3^-	167.657(17)	0.57(3)	0.10	$(E1)$	
		99.381(7)	3^-	214.677(23)	6.6(4)	0.05	$E1$	
		59.007(6)	2^-	255.04(3)	3.19(19)	0.04	$E1$	
316.531(19)	1^-	59.007(6)	2^-	257.50(3)	3.11(18)	0.30	$M1+E2$	0.60(22)
		0.0	1^-	316.58(4)	5.63(16)	0.21	$M1$	
317.792(19)	5^-	174.059(11)	4^-	143.88(3)	1.6(2)	1.25	$M1+E2$	$1.6(^{+12}_{-5})$
322.488(15)	3^-	210.722(10)	2^-	111.65(3)^a	1.4(3)	3.77	$[M1]$	
		174.059(11)	4^-	148.92(7)^a	0.082(20)	1.66	$[M1]$	
		146.227(9)	3^-	176.32(3)^a	0.38(8)	1.03	$(M1,E2)$	
		99.381(7)	3^-	223.05(3)	0.50(3)	0.38	$M1+E2$	$1.02(^{+29}_{-22})$
		59.007(6)	2^-	263.14(7)^a	0.23(5)	0.34	$[M1]$	
∼330	5^+	∼186	6^-	144.230(22)	2.6(3)	0.15	$E1$	

Table 6. (*Continued.*)

E_i (keV)	$J_i^{\pi_i}$	E_f (keV)	$J_f^{\pi_f}$	E_γ (keV)	σ_γ (b)	α	XL	δ_γ
351.25(3)	$\mathbf{4}^{+}$	146.227(9)	3^-	205.14(9)^a	0.056(15)	0.06	$[E1]$	
		99.381(7)	3^-	251.87(3)	4.3(3)	0.04	$E1$	
378.535(18)	2^-	316.531(19)	1^-	62.22(4)^a	1.11(17)	3.55	$M1(+E2)$	$\leq 1.0^l$
		146.227(9)	3^-	232.16(3)^h	0.55(6)	0.48	$[M1]$	
		59.007(6)	2^-	319.48(4)	0.368(23)	0.20	$[M1]$	
		0.0	1^-	378.49(5)	1.52(9)	0.13	$M1$	
417.784(21)	$\mathbf{5}^{-}$	273.566(12)	4^-	144.230(22)^c	0.075(4)	1.82	$[M1]$	
		268.729(12)	4^-	148.92(7)	0.57(10)	1.21	$M1+E2$	$1.2(^{+8}_{-4})$
		146.227(9)	3^-	271.56(4)^a	0.23(7)	0.12	$[E2]$	
420.51(3)	4^+	313.989(12)	3^+	106.58(3)^c	0.91(11)	3.48	$M1+E2$	$1.7(^{+37}_{-7})$
425.70(3)	$\mathbf{4}^{+}$	313.989(12)	3^+	111.65(3)	1.1(4)	3.77	$[\boldsymbol{M1}]$	
462.914(18)	5^-	317.792(19)	5^-	145.131(8)^{d,e}	0.068(21)	1.79	$[M1]$	
		273.566(12)	4^-	189.270(20)^a	0.48(12)	0.62	$M1+E2$	$1.0(^{+4}_{-3})$
		268.729(12)	4^-	193.83(16)^h	0.142(8)	0.79	$[M1]$	
		174.059(11)	4^-	289.32(8)^a	0.044(13)	0.26	$[M1]$	
		99.381(7)	3^-	363.56(5)	0.239(17)	0.05	$[E2]$	
469.945(19)	4^-	322.488(15)	3^-	147.460(19)^h	1.03(3)	1.71	$(M1+E2)$	
		268.729(12)	4^-	201.16(3)^a	0.19(4)	0.59	$[M1]$	
		174.059(11)	4^-	296.03(5)	0.141(11)	0.25	$M1$	
470.755(21)	3^-	378.535(18)	2^-	92.104(21)^a	0.59(13)	6.03	$M1(+E2)$	≤ 1.4
		322.488(15)	3^-	148.09(6)^{d,e}	0.040(12)	1.69	$[M1]$	
		268.729(12)	4^-	202.64(4)^a	0.040(12)	0.70	$[\boldsymbol{M1}]$	
		59.007(6)	2^-	411.52(7)	0.321(24)	0.10	$[M1]$	
$\sim$471	$\mathbf{6}^{+}$	$\sim$330	5^+	141.31(4)	0.285(23)	1.55	$M1+E2$	$0.9(^{+9}_{-5})$
497.20(4)	6^-	317.792(19)	5^-	179.41(3)	0.23(4)	0.98	$[M1]$	
500.74(6)	$\mathbf{5}^{+}$	351.25(3)	$\mathbf{4}^{+}$	149.57(8)^a	0.8(4)	1.06	$M1+E2$	$1.8(^{+13}_{-5})$
		99.381(7)	3^-	401.29(7)	0.101(10)	0.37	$[\boldsymbol{M2}]$	
534.32(5)	4^-	273.566(12)	4^-	259.84(9)^g	0.76(16)	0.35	$[M1]$	
		174.059(11)	4^-	360.53(5)	0.95(6)	0.15	$M1$	
549.16(5)	$\mathbf{5}^{+}$	425.70(3)	$\mathbf{4}^{+}$	123.46(3)^c	0.38(5)	2.27	$M1(+E2)$	≤ 1.1
559.96(4)	5^+	425.70(3)	$\mathbf{4}^{+}$	134.16(4)	0.067(8)	2.23	$[\boldsymbol{M1}]$	
		420.51(3)	4^+	139.61(5)	0.37(6)	1.34	$M1+E2$	$1.8(^{+46}_{-7})$
$\sim$562	6^+	$\sim$330	5^+	232.16(3)^h	0.18(4)	0.48	$[M1]$	
577.87(3)	2^-	378.535(18)	2^-	199.81(13)^c	0.62(21)	0.72	$[M1]$	
		316.531(19)	1^-	261.23(3)	1.16(19)	0.35	$(M1)$	
588.92(3)	4^-	470.755(21)	3^-	118.173(13)	0.49(3)	3.21	$[M1]$	
601.82(4)	1^+	316.531(19)	1^-	285.29(4)	0.59(4)	0.03	$(E1)$	
		210.722(10)	2^-	391.01(5)	3.27(6)	0.01	$E1$	
623.97(5)	1^-	322.488(15)	3^-	300.51(13)^a	0.14(5)	0.09	$[\boldsymbol{E2}]$	
		210.722(10)	2^-	413.39(5)	0.42(3)	0.10	$[\boldsymbol{M1}]$	

Table 6. (*Continued.*)

E_i (keV)	$J_i^{\pi_i}$	E_f (keV)	$J_f^{\pi_f}$	E_γ (keV)	σ_γ (b)	α	XL	δ_γ
646.26(4)	5^-	469.945(19)	4^-	176.32(3)	0.37(9)	1.03	$(M1, E2)$	
		317.792(19)	5^-	$328.42(20)^{d,e}$	0.078(23)	0.19	$[M1]$	
658.27(4)	2^+	601.82(4)	1^+	$56.445(18)^a$	0.10(3)	29.59	$M1(+E2)$	≤ 1.1
		322.488(15)	3^-	$335.67(15)^a$	0.046(16)	0.02	$[E1]$	
		316.531(19)	1^-	340.969(11)	0.111(12)	0.02	$[E1]$	
665.23(6)	$\boldsymbol{6^+}$	500.74(6)	$\boldsymbol{5^+}$	$164.490(24)^c$	0.13(3)	0.89	$M1+E2$	$1.19(^{+29}_{-22})$
680.21(4)	$\boldsymbol{2^-}$	322.488(15)	3^-	357.77(5)	0.305(20)	0.15	$[\boldsymbol{M1}]$	
		210.722(10)	2^-	$469.38(7)^h$	0.174(16)	0.07	$[\boldsymbol{M1}]$	
		0.0	1^-	680.34(15)	0.58(13)	0.03	$[\boldsymbol{M1}]$	
686.20(3)	3^-	577.87(3)	2^-	$108.315(18)^a$	0.18(4)	4.11	$[M1]$	
		470.755(21)	3^-	$215.28(15)^{d,e}$	0.098(24)	0.59	$[M1]$	
		378.535(18)	2^-	307.69(4)	0.70(5)	0.22	$M1$	
691.44(5)	6^-	462.914(18)	5^-	$228.57(6)^h$	0.087(9)	0.50	$[M1]$	
		317.792(19)	5^-	373.60(6)	0.127(11)	0.13	$[M1]$	
736.39(4)	5^-	588.92(3)	4^-	$147.460(19)^h$	0.200(22)	1.71	$[M1]$	
745.47(4)	3^+	658.27(4)	2^+	$87.199(8)^{d,i}$	0.192(14)	7.66	$M1$	
$761.49(6)^j$	$(1^-, 2^-, 3^-)$	322.488(15)	3^-	438.89(7)	0.158(16)	0.09	$[\boldsymbol{M1}$ or $\boldsymbol{E2}]$	
		210.722(10)	2^-	$551.12(9)^a$	0.15(5)	0.05	$[\boldsymbol{M1}]$	
		0.0	1^-	$760.99(18)^k$	0.207(22)	0.02	$[\boldsymbol{M1}$ or $\boldsymbol{E2}]$	
$785.52(5)^j$		378.535(18)	2^-	406.98(6)	0.197(19)			
$796.24(4)^j$	(≤ 3)	577.87(3)	2^-	$218.14(6)^h$	0.114(12)			
		378.535(18)	2^-	$418.22(6)^a$	0.23(11)			
		316.531(19)	1^-	479.68(6)	0.63(4)			
		210.722(10)	2^-	$584.36(12)^a$	0.16(8)			
		0.0	1^-	$796.46(18)^a$	0.18(15)			
$819.21(5)^j$	$(2^-, 3^-)$	322.488(15)	3^-	496.78(7)	0.37(2)	0.06	$[\boldsymbol{M1}]$	
		210.722(10)	2^-	$607.50(12)^a$	0.24(9)	0.04	$[\boldsymbol{M1}]$	
		174.059(11)	4^-	$645.39(9)^a$	0.11(4)	0.03	$[\boldsymbol{M1}$ or $\boldsymbol{E2}]$	
		59.007(6)	2^-	$760.99(18)^k$	0.207(22)	0.02	$[\boldsymbol{M1}]$	
$821.47(5)^j$	(≤ 3)	658.27(4)	2^+	$163.47(7)^a$	0.13(5)			
		601.82(4)	1^+	219.70(4)	0.237(18)			
$826.48(5)^j$	(4^-)	686.20(3)	3^-	140.20(5)	0.52(6)	1.12	$E2, M1$	
		588.92(3)	4^-	$237.54(17)^a$	0.073(21)	0.45	$[M1]$	
		470.755(21)	3^-	$355.84(6)^a$	0.22(5)	0.15	$[M1]$	
$855.39(6)^j$	(4^+)	745.47(4)	3^+	109.93(5)	0.157(18)	3.94	$[M1]$	
		658.27(4)	2^+	$197.06(12)^a$	0.022(4)	0.34	$[E2]$	
$864.70(9)^j$	$(2^-, 3^-)$	577.87(3)	2^-	286.83(8)	0.118(11)	0.27	$[\boldsymbol{M1}]$	

Table 6. (*Continued.*)

E_i (keV)	$J_i^{\pi_i}$	E_f (keV)	$J_f^{\pi_f}$	E_γ (keV)	σ_γ (b)	α	XL	δ_γ
6179.59(5)	2^+, 3^+	2359.0(5)^{j,p}		3820.5(5)^{m}	0.018(7)		**(E1 or M1)**^{n}	
		2319.81(23)^{j,p}		3859.73(22)^{m}	0.068(7)		**(E1)**^{o}	
		2244.86(15)^{j}		3934.68(14)	0.143(11)		**(E1)**^{o}	
		2219.24(22)^{j}		3960.30(21)	0.049(6)		**(E1)**^{o}	
		2203.4(3)^{j}		3976.1(3)	0.049(7)		**(E1)**^{o}	
		1964.83(14)^{j}		4214.71(13)	0.05(3)		**(E1)**^{o}	
		1905.8(4)^{j}		4273.7(4)	0.056(8)		**(E1)**^{o}	
		1881.39(22)^{j}		4298.14(21)	0.172(14)		**(E1)**^{o}	
		1846.46(22)^{j}	$(2^-,3^-)$	4333.07(21)^{m}	0.068(9)		**[E1]**	
		1838.7(3)^{j}	$(1^-,2^-,3^-)$	4340.8(3)^{m}	0.046(6)		**[E1]**	
		1827.59(17)^{j}	$(2^-,3^-,4^-)$	4351.94(16)^{m}	0.188(14)		**[E1]**	
		1758.0(4)^{j}	$(2^-,3^-)$	4421.5(4)^{m}	0.090(15)		**[E1]**	
		1743.21(22)^{j,p}		4436.32(21)^{m}	0.104(9)		**(E1)**^{o}	
		1718.96(24)^{j}	$(2^-,3^-,4^-)$	4460.57(23)^{m}	0.218(17)		**[E1]**	
		1694.7(4)^{j,p}	$(2^-,3^-)$	4484.8(4)^{m}	0.031(6)		**[E1]**	
		1672.3(3)^{j}	$(1^-,2^-,3^-)$	4507.2(3)	0.205(15)		**[E1]**	
		1659.18(15)^{j,p}	$(^-)$	4520.35(14)^{m}	0.043(16)		**(E1)**^{o}	
		1646.93(23)^{j}	$(2^-,3^-,4^-)$	4532.60(22)	0.149(16)		**[E1]**	
		1628.24(22)^{j}	$(2^-,3^-,4^-)$	4551.29(21)	0.080(8)		**[E1]**	
		1607.16(22)^{j}		4572.37(21)	0.138(11)		**(E1)**^{o}	
		1601.7(3)^{j,p}		4577.8(3)^{m}	0.040(6)		**(E1)**^{o}	
		1587.11(16)^{j,p}		4592.42(15)	0.189(13)		**(E1)**^{o}	
		1572.04(20)^{j}	$(1^-,2^-,3^-)$	4607.49(19)^{m}	0.086(8)		**[E1]**	
		1566.41(18)^{j}	$(2^-,3^-,4^-)$	4613.12(17)	0.137(11)		**[E1]**	
		1550.71(20)^{j}	$(1^-,2^-,3^-)$	4628.82(19)^{m}	0.090(7)		**[E1]**	
		1545.01(17)^{j}	$(^-)$	4634.52(16)	0.312(19)		**(E1)**^{o}	
6179.59(5)	2^+, 3^+	1525.30(20)^{j}	(4^-)	4654.23(19)^{m}	0.063(6)		**[E1]**	
		1486.71(17)^{j,p}		4692.81(16)	0.182(13)		**(E1)**^{o}	
		1475.9(3)^{j}	$(^-)$	4703.6(3)	0.110(12)		**(E1)**^{o}	
		1462.4(5)^{j}	$(2^-,3^-)$	4717.1(5)^{m}	0.021(5)		**[E1]**	
		1457.50(21)^{j}	$(2^-,3^-)$	4722.02(20)^{m}	0.060(7)		**[E1]**	
		1449.8(4)^{j}	$(1^-,2^-,3^-)$	4729.7(4)^{m}	0.025(5)		**[E1]**	
		1437.76(24)^{j}		4741.76(23)	0.098(11)		**(E1)**^{o}	
		1419.0(3)^{j}	$(2^-,3^-)$	4760.5(3)^{m}	0.053(7)		**[E1]**	
		1405.48(16)^{j}	$(2^-,3^-,4^-)$	4774.04(15)	0.74(4)		**[E1]**	
		1393.0(3)^{j}	$(2^-,3^-)$	4786.5(3)^{m}	0.032(8)		**[E1]**	
		1375.7(7)^{j}	$(1^-,2^-,3^-)$	4803.8(7)^{m}	0.022(10)		**[E1]**	
		1360.3(4)^{j}	$(2^-,3^-,4^-)$	4819.2(4)^{m}	0.018(5)		**[E1]**	
		1355.4(3)^{j}	$(2^-,3^-)$	4824.1(3)^{m}	0.033(5)		**[E1]**	
		1351.21(19)^{j}	(4^-)	4828.31(18)	0.094(9)		**[E1]**	

Table 6. (*Continued.*)

E_i (keV)	$J_i^{\pi_i}$	E_f (keV)	$J_f^{\pi_f}$	E_γ (keV)	σ_γ (b)	α	XL	δ_γ
6179.59(5)	2^+, 3^+	1342.3(4)^{j,p}		4837.2(4)^{m}	0.017(4)		**(E1 or M1)**^{n}	
		1321.69(20)^{j}	$(2^-,3^-)$	4857.83(19)^{m}	0.251(17)		**[E1]**	
		1317.37(17)^{j}	$(2^-,3^-,4^-)$	4862.15(16)	0.71(4)		**[E1]**	
		1285.9(9)^{j}	$(2^-,3^-)$	4893.7(9)	0.056(9)		**[E1]**	
		1242.70(21)^{j}	$(2^-,3^-)$	4936.82(20)^{m}	0.35(3)		**[E1]**	
		1240.3(3)^{j,p}		4939.2(3)^{m}	0.079(16)		**(E1)**^{o}	
		1231.3(3)^{j}	$(2^-,3^-)$	4948.2(3)^{m}	0.058(6)		**[E1]**	
		1227.94(21)^{j,p}		4951.58(20)^{m}	0.138(10)		**(E1)**^{o}	
		1212.0(4)^{j,p}		4967.5(4)^{m}	0.023(5)		**(E1 or M1)**^{n}	
		1197.95(18)^{j}	$(2^-,3^-)$	4981.57(17)	0.315(20)		**[E1]**	
		1185.05(19)^{j}	$(2^-,3^-)$	4994.47(18)	0.115(9)		**[E1]**	
		1172.25(18)^{j}	$(^-)$	5007.27(17)	0.91(5)		**(E1)**^{o}	
		1157.85(20)^{j}	$(2^-,3^-,4^-)$	5021.66(19)^{m}	0.099(8)		**[E1]**	
		1151.19(18)^{j}	(4^-)	5028.32(17)	0.86(5)		**[E1]**	
		1140.9(3)^{j}	$(2^-,3^-)$	5038.6(3)^{m}	0.028(4)		**[E1]**	
		1132.12(20)^{j}		5047.39(19)	0.104(8)		**(E1)**^{o}	
		1122.55(23)^{j}	$(2^-,3^-)$	5056.96(22)^{m}	0.083(8)		**[E1]**	
		1102.74(18)^{j}	$(2^-,3^-)$	5076.77(17)^{m}	0.262(17)		**[E1]**	
		1097.06(18)^{j}	(4^-)	5082.45(17)	0.173(11)		**[E1]**	
		1071.5(6)^{j,p}	$(2^-,3^-)$	5108.0(6)^{m}	0.025(8)		**[E1]**	
		1068.61(22)^{j}	$(2^-,3^-)$	5110.90(21)	0.148(12)		**[E1]**	
		1057.5(5)^{j}	$(2^-,3^-)$	5122.0(5)^{m}	0.013(4)		**[E1]**	
		1053.8(6)^{j}	$(1^-,2^-,3^-)$	5125.7(6)^{m}	0.012(4)		**[E1]**	
		1040.30(19)^{j}	$(2^-,3^-,4^-)$	5139.21(18)	0.78(5)		**[E1]**	
		1017.65(17)^{j,p}	$(2^-,3^-,4^-)$	5161.86(16)^{m}	0.010(3)		**[E1]**	
		1013.7(3)^{j}	$(2^-,3^-,4^-)$	5165.74(24)^{m}	0.043(4)		**[E1]**	
		1003.08(19)^{j,p}	$(2^-,3^-,4^-)$	5176.43(18)	0.50(3)		**[E1]**	
		988.97(22)^{j}	$(2^-,3^-)$	5190.54(21)^{m}	0.051(6)		**[E1]**	
		982.32(18)^{j,p}		5197.19(17)^{m}	0.050(5)		**(E1)**^{o}	
		973.31(20)^{j}	$(^-)$	5206.20(19)	0.275(18)		**(E1)**^{o}	
		954.78(23)^{j}		5224.73(22)	0.048(5)		**(E1)**^{o}	
		935.37(20)^{j}	$(2^-,3^-)$	5244.14(19)	0.128(9)		**[E1]**	
		923.57(20)^{j}	$(2^-,3^-)$	5255.94(19)	0.307(19)		**[E1]**	
		902.43(19)^{j}	$(2^-,3^-)$	5277.08(18)	0.46(3)		**[E1]**	
		895.15(19)^{j}	$(2^-,3^-,4^-)$	5284.36(18)^{m}	0.230(15)		**[E1]**	
		888.70(24)^{j}	(4^-)	5290.81(23)	0.040(5)		**[E1]**	
		856.3(5)^{j}	$(2^-,3^-)$	5323.2(5)^{m}	0.013(3)		**[E1]**	
		826.48(5)^{j}	(4^-)	5353.09(20)	0.46(3)		**[E1]**	

Table 6. (*Continued.*)

E_i (keV)	$J_i^{\pi_i}$	E_f (keV)	$J_f^{\pi_f}$	E_γ (keV)	σ_γ (b)	α	XL	δ_γ
6179.59(5)	2^+, 3^+	819.21(5)[j]	(2^-,3^-)	5360.18(20)	0.214(13)		**[*E*1]**	
		796.24(4)[j]	(≤3)	5383.06(19)	0.086(6)		**(*E*1)**[o]	
		791.3(3)[j]	(1^-)	5388.19(24)[m]	0.035(4)		**[*E*1]**	
		761.49(6)[j]	(1^-,2^-,3^-)	5418.6(3)[m]	0.0142(23)		**[*E*1]**	
		753.50(22)[j]	(2^-,3^-)	5426.00(21)[m]	0.035(3)		**[*E*1]**	
		686.20(3)	3^-	5493.50(18)	0.297(18)		**[*E*1]**	
		680.21(4)	**2^-**	5499.4(3)[m]	0.031(3)		**[*E*1]**	
		623.97(5)	1^-	5555.4(8)[m]	0.0065(23)		**[*E*1]**	
		577.87(3)	2^-	5601.65(18)	0.367(22)		**[*E*1]**	
		534.32(5)	4^-	5645.07(20)	0.257(16)		**[*E*1]**	
		469.945(19)	4^-	5709.67(20)	0.386(24)		**[*E*1]**	
		425.70(3)	**4^+**	5753.2(3)[m]	0.024(4)		**[*M*1]**	
		420.51(3)	4^+	5759.1(8)	0.006(3)		**[*M*1]**	
		378.535(18)	2^-	5800.93(21)	0.051(4)		**[*E*1]**	
		322.488(15)	3^-	5856.95(19)	0.46(3)		**[*E*1]**	
		316.531(19)	1^-	5863.4(3)[m]	0.040(3)		**[*E*1]**	
		273.566(12)	4^-	5905.7(2)[m]	0.095(9)		**[*E*1]**	
		268.729(12)	4^-	5910.62(19)	2.00(5)		**[*E*1]**	
		210.722(10)	2^-	5968.92(24)	0.052(4)		**[*E*1]**	
		174.059(11)	4^-	6005.59(21)	0.184(12)		**[*E*1]**	
		146.227(9)	3^-	6033.26(21)	0.250(15)		**[*E*1]**	
		99.381(7)	3^-	6080.29(20)	0.406(24)		**[*E*1]**	
		59.007(6)	2^-	6120.38(20)	0.397(23)		**[*E*1]**	
		0.0	1^-	6179.30(21)	0.059(4)		**[*E*1]**	

[a] Multiplet resolved using ENSDF branching ratios [3].

[b] Multiplet resolved using X-ray yields from Reference [10].

[c] Multiplet resolved using statistical-model calculations.

[d] Transition not observed; γ-ray energy taken as ENSDF value [3] or deduced from level-energy difference.

[e] Transition not observed; intensity deduced from ENSDF branching ratios [3].

[f] Level energy from Reference [22].

[g] Multiplet resolved using γ-ray branching ratio adjusted to optimize agreement with model calculations.

[h] Gamma ray multiply-placed in level scheme; intensity divided using statistical-model calculations.

[i] Transition not observed; intensity deduced from statistical-model calculations.

[j] Level above E_c not included in statistical-model calculations.

[k] Gamma ray multiply-placed in level scheme; undivided intensity given.

[l] Mixing ratio other than the mean or limiting value from the ENSDF [3] used to calculate α.

[m] Newly-identified primary γ-ray transition not found in literature.

[n] Primary γ ray with $\sigma_\gamma < 0.03$ b assigned tentative $E1$ or $M1$ multipolarity.

[o] Primary γ ray with $\sigma_\gamma \geq 0.03$ b assigned tentative $E1$ multipolarity.

[p] Level proposed in Reference [63].

4.5.1 Nuclear Structure.

The predicted population of individual low-lying levels from statistical-model calculations can be plotted against the experimental depopulation, hereafter referred to as a population-depopulation (P-D) plot. Good agreement between the values, indicated by a line of slope 1 in the P-D plot and residual differences of less than 3 standard deviations (σ), provides support for the choice of LD and PSF models used, the placement of transitions and spin-parity assignments for levels below E_c in the level scheme, γ-ray branching ratios, and multipole mixing ratios δ_γ. This comparison can be used as an effective tool for evaluating the completeness and accuracy of the decay scheme. Preempting the results presented later in this section, optimal agreement in the P-D plot is achieved with the MGLO ($k_0 = 2.9$) model for the PSF (assuming the parametrization of Reference [123]) and the CTF LD model (assuming the parametrization of Reference [114]). The resulting P-D plot, which was generated for a critical energy of $E_c = 746$ keV and with the level spin-parity assignments, branching ratios, and multipole mixing ratios discussed later in the text, is shown in Figure 26.

Capture-state Spin Composition.

The ground-state spin-parity of the target nucleus ^{185}Re is $J^{\pi}_{\text{g.s.}} = 5/2^+$ [129], so s-wave neutron capture results in a ^{186}Re compound nucleus with an admixture of 2^+ and 3^+ spins. The total experimental capture cross section σ_0 is equal to the sum of the cross sections $\sigma(+,-)$ for populating the low-spin (2^+) and high-spin (3^+) resonances, and the cross section $\sigma(B)$ for populating any bound resonances (with spin $J_{\text{g.s.}} \pm 1/2$), according to the expression

$$\sigma_0 = \sigma_\gamma(-) + \sigma_\gamma(+) + \sigma_\gamma(\text{B}). \tag{58}$$

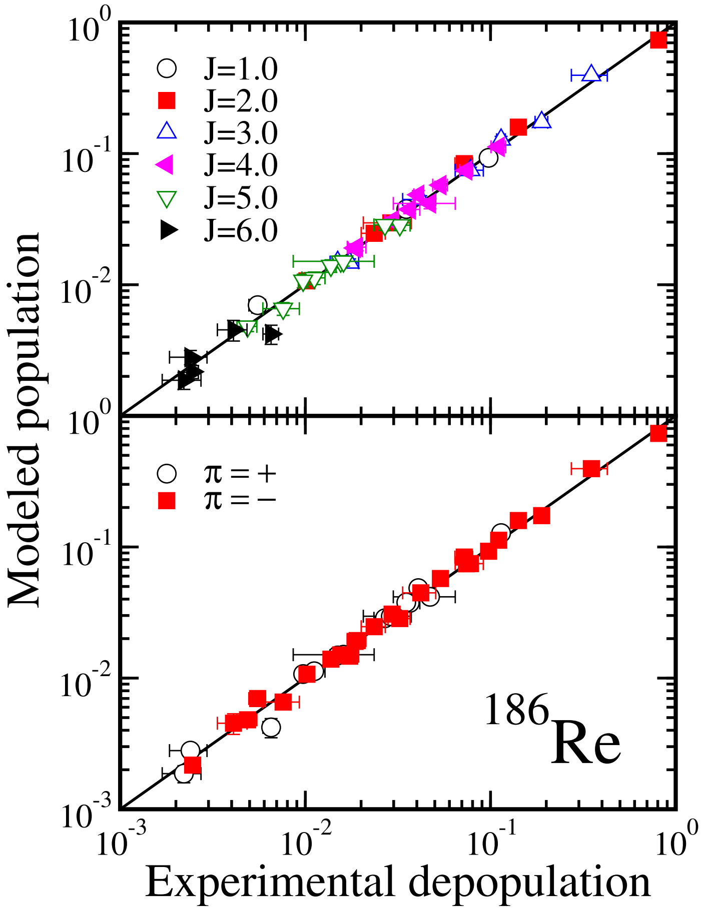

Figure 26. Plot of modeled population versus experimental depopulation (P-D plot) resulting from statistical-model calculations with a critical energy of $E_c = 746$ keV, using the MGLO model with $k_0 = 2.9$ for the PSF and the CTF model for the LD with the parameterization described in Reference [114]. The calculations used to generate this plot assume the level J^π assignments summarized in Table 7 and the branching ratio and multipole-mixing ratio adjustments described in the text.

There is one bound resonance with an energy of -4.466 eV relative to the neutron-separation energy of ^{186}Re, which has a tentative spin assignment of $J = (3)$ listed in Reference [111]. The expression in Equation (58) implies a capture-state spin composition with a fraction F^- in the low-spin 2^+ state given by

$$F^- = \frac{\sigma(-)}{\sigma_0}. \tag{59}$$

Using values of $\sigma_\gamma(+) = 58.9$ b for populating the $J^\pi = 3^+$ state, $\sigma_\gamma(-) = 1.3$ b for populating the $J^\pi = 2^+$ state, and $\sigma_\gamma(\mathrm{B}) = 51.8$ b from Reference [111], the resulting fraction is $F^- = 0.012$. Given the tentative nature of the $J = (3)$ spin assignment for the bound resonance, an alternative possibility is that the bound resonance has spin $J = 2$, which would result in a fraction

$$F^- = \frac{\sigma(-) + \sigma(\mathrm{B})}{\sigma_0} \tag{60}$$

in the 2^+ state, equal to $F^- = 0.474$ using the cross sections from Reference [111]. Statistical-model calculations were performed using both capture-state spin compositions, and the best agreement between modeled population and experimental depopulation is consistently achieved with $F^- = 0.012$. This composition is adopted for all calculations described in this work, and our results support the tentative claim of a $J = (3)$ assignment for the bound resonance [111].

Discrete-level Spin-parity Assignments.

The spin and parity is known unambiguously only for the ground state of ^{186}Re [3]. All excited states have only tentative assignments in the adopted level scheme [3]. The simulated population of low-lying levels depends on their J^π assignments, and the population of specific levels is largely independent of the choices of LD and PSF models. Therefore, a population-depopulation comparison provides a means of checking tentative J^π assignments for individual levels. Using the statistical model, we were able to confirm tentative assignments or suggest new values based on optimal agreement with experimental data (revealed through P-D plots) for all states below $E_c = 746$ keV in ^{186}Re. In this work, we have confirmed 32 previously tentative J^π assignments and recommend new assignments for seven other levels in ^{186}Re, which are summarized in Table 7. This technique of using statistical-decay model agreement with experimental data to propose J^π assignments has been employed previously in Reference [8].

Table 7. Level J^π assignments from the ENSDF adopted level scheme [3] and the proposed assignments from this work, based on observed agreement between experimental depopulation and modeled population. Levels are arranged according to their excitation energy E_x.

E_x (keV)	J^π_{ENSDF}	$J^\pi_{\text{this work}}$
351.25(3)	$(3)^+$	4^+
425.70(3)	$(2^+, 3^+, 4^+)$	4^+
~471	$(4)^+$	6^+
500.74(6)	$(4)^+$	5^+
549.16(5)	$(^+)$	5^+
665.23(6)	$(5)^+$	6^+
680.21(4)	$(2^-, 3^-)$	2^-

The improvement in the P-D plots after adjusting the J^π assignments for the 351.3-, ~471-, 500.7-, and 665.2-keV levels is evident from the significant reduction observed in the absolute residual differences $|R|$ between the modeled population and the experimental depopulation for these levels, shown in Figure 27. Adjusting the J^π assignment of a particular level can affect the feeding to other levels below it in the level scheme, so the proposals listed in Table 7 also improved agreement in the P-D plots for several other levels, which can be seen in Figure 27.

The new assignments proposed in this work are discussed, in turn, below.

351.3-, 500.7-, and 665.2-keV levels. The 351.3-keV level has a spin-parity assignment of $(3)^+$ in the adopted level scheme [3], based on the existence of an $E1$ transition to the $J^\pi = (3)^-$, 99.4-keV level. The multipolarity of this transition was determined from conversion-electron spectrometry by Lanier *et al.* [60]. Glatz [61] determined the 351.3-keV level to be the $K^\pi = (3)^+$ band head, and placed the $J^\pi = (4)^+$, 500.7-keV and $J^\pi = (5)^+$, 665.2-keV levels in the rotational band

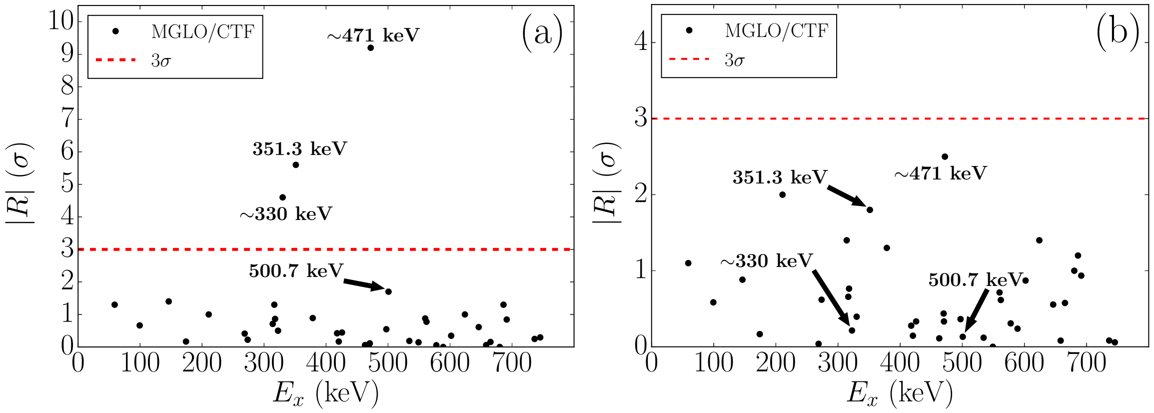

Figure 27. Plots of the absolute value of the residual difference $|R|$, in units of standard deviations σ, between the modeled population and experimental depopulation as a function of level excitation energy E_x, for (a) levels before spin-parity adjustments, and (b) after the spin-parity assignments for the 351.3-, ~471-, 500.7-, and 665.2-keV levels are adjusted as described in the text. The ~330-keV level is highlighted because its population is influenced by the J^π assignment of the ~477-keV level that directly feeds it. In both panels, the assignments for the 425.7-, 549.2-, and 680.2-keV levels are taken to be the proposed values from Table 7. The horizontal dashed line identifies a residual difference of 3σ. Both plots result from statistical-model calculations using the MGLO model with $k_0 = 2.9$ for the PSF and the CTF model for the LD with the parameterization described in Reference [114].

according to $\gamma-\gamma$ coincidences from (n,γ) reactions on ^{185}Re. In this work, agreement in the P-D plot for the 351.3-keV level is significantly improved when the spin is increased to $J = 4$, as illustrated in Figure 27. A $J^\pi = 4^+$ assignment for the 351.3-keV level remains consistent with the measured $E1$ multipolarity for the 251.9-keV transition to the 99.4-keV level. For the first member of the rotational band built on the 351.3-keV band head, the agreement between the modeled population and experimental depopulation is improved when the assignment for the 500.7-keV level is changed to $J^\pi = 5^+$. The rotational band structure implies an assignment of $J^\pi = 6^+$ for the 665.2-keV level. Unfortunately the 164.5-keV transition deexciting this level is part of a multiplet, and its intensity was adjusted using the DICEBOX results, so the P-D plots before and after the spin adjustment could not be compared.

425.7-keV level. This level has an indefinite spin-parity assignment of

$J^\pi = (2^+, 3^+, 4^+)$ in the adopted level scheme [3], deduced from the existence of a 111.7-keV transition that feeds the $J^\pi = (3)^+$ level at 314.0 keV. Of the three suggested values for the 425.7-keV level, the $J^\pi = 4^+$ assignment provides optimal agreement between the modeled population and the experimental depopulation for both the 425.7- and 314.0-keV levels.

∼471-keV level. The $J^\pi = (4)^+$ assignment in the ENSDF [3] for this level is based on a tentative $(\pi 9/2^-[514]) - (\nu 1/2^-[510])$ configuration from Reference [61] and the existence of a mixed $M1 + E2$ transition feeding the $J^\pi = (5)^+$ level at ∼330-keV. Calculations assuming the adopted spin-parity assignment for the ∼471-keV level produce a significantly greater population than the experimentally-observed depopulation for both the ∼330-keV level and the ∼471-keV level, which is clear from Figure 27(a). Optimal agreement in the P-D plot for both of these levels is achieved with a $J^\pi = 6^+$ assignment for the ∼471-keV level (Figure 27(b)), and this assignment is consistent with a transition to the $J^\pi = (5)^+$, ∼330-keV level with mixed $M1 + E2$ multipolarity. The $J^\pi = 6^+$ assignment proposed in this work may suggest that the ∼471-keV level is the first member of a rotational band built on the $K^\pi = (5)^+$, ∼330-keV level.

549.2-keV level. No spin assignment for this level is provided in the adopted level scheme [3], and it has only a tentative $\pi = (+)$ parity assignment based on the existence of a 123.5-keV $M1(+E2)$ transition feeding the 425.7-keV level from (n, γ) and (d, p) measurements by Lanier *et al.* [60]. Assuming a $J^\pi = 4^+$ assignment for the 425.7-keV level as discussed above, the possible assignments for the 549.2-keV level that are consistent with the measured $M1(+E2)$ multipolarity for the transition to the 425.7-keV level are $J^\pi = 3^+$, 4^+, and 5^+. Of these, the $J^\pi = 5^+$ assignment produces the best agreement in the resulting P-D plot.

680.2-keV level. In the adopted level scheme, this level has an indefinite spin-parity assignment of $J^{\pi} = (2^{-}, 3^{-})$ [3] due to the existence of γ rays feeding the $J^{\pi} = 1^{-}$ ground state, the $J^{\pi} = (2)^{-}$ level at 210.7 keV, and the $J^{\pi} = (3)^{-}$ state at 322.5 keV. A $J^{\pi} = 2^{-}$ assignment results in the best agreement between the modeled level population and the experimental depopulation, and implies the three γ-ray transitions deexciting this level have some degree of $M1$ character.

Isomer Feeding, Multipole Mixing, and Branching Ratios.

Four other levels below E_c also warrant discussion here:

148.2-keV level. The $J^{\pi} = (8^{+})$ isomer, recently reported in Reference [22] to have an excitation energy of 148.2(5) keV (cf. the adopted value of 149(7) keV [3]), is very weakly populated due to its large spin difference from the capture state. There was no observation of the highly-converted 50-keV transition deexciting the level [3] in the prompt γ-ray spectrum. As a result, no P-D comparison could be made. Calculations that include this level result in a cross section for populating the isomer equal to 0.071(24) b. Two measurements have been made of the ratio of thermal-neutron capture cross sections for the $^{185}\mathrm{Re}(n,\gamma)^{186}\mathrm{Re}^{m}$ and $^{185}\mathrm{Re}(n,\gamma)^{186}\mathrm{Re}^{g}$ reactions using activation techniques: 0.3% [21] and 0.54(11)% [17]. When combined with the adopted value of $\sigma_0 = 112(2)$ b for populating the ^{186}Re ground state [111], these ratios yield isomer cross sections of 0.34(10) b and 0.60(12) b, respectively. The discrepancy between the measured and calculated cross sections for isomer population may imply there are levels or transitions missing from the adopted level scheme below E_c that feed the isomer. A recent investigation of $^{187}\mathrm{Re}(n,2n)$ reactions by Matters *et al.* reported two feeding levels at 414.9 keV and 796.1 keV [22], but because these levels have proposed spin-parity assignments of $J^{\pi} = (9^{+})$ and (10^{+}) they are also weakly populated in the (n,γ) reaction, and their inclusion in the calculations does not correct the discrepancy. Given the $J^\pi = 6^+$ assignment proposed above for the ∼471-keV level, it is possible that this level feeds the isomer via an unplaced $E2$ transition with an energy of ∼323-keV. In the prompt γ-ray spectrum, there are three such unplaced γ rays at 321.57(7) keV, 322.61(9) keV, and 323.99(7) keV, with partial cross sections of 0.234(24) b, 0.204(21) b, and 0.143(14) b, respectively, which could partly account for the discrepancy. Isomer feeding from the $J^\pi = (6)^-$, ∼186-keV level, discussed below, is another possibility. These hypotheses could not be verified in this study, because no $\gamma - \gamma$ coincidence data was collected.

∼186-keV level. The $J^\pi = (6)^-$, ∼186-keV level is directly fed by the $J^\pi = (5)^+$, ∼330-keV level via an $E1$ transition, and has a modeled population of 4.5(4) b. In the adopted level scheme for ^{186}Re, there are no transitions out of this level to lower-lying levels [3], although a ∼12-keV $E2$ transition to the $J^\pi = 4^-$, 174.1-keV level and a ∼38-keV $M2$ transition to the 148.2-keV isomer have been proposed in the literature (References [21], [60], and [61]). Both transitions would be highly converted ($\alpha = 7.1 \times 10^4$ for the ∼12-keV transition and $\alpha = 1.0 \times 10^3$ for the ∼38-keV transition), and their energies would be sufficiently low that they would not be observable in the prompt $^{185}\mathrm{Re}(n, \gamma)$ spectrum of this work. The modeled population of the ∼186-keV level gives an upper bound for the γ-ray cross section of each of these two possible transitions, which are listed in Table 6. It should be noted that the modeled population and experimental depopulation of the 174.1-keV level is balanced prior to including the ∼12-keV transition in the calculations, but the mixed $M1 + E2$, 74.7-keV γ ray deexciting this level is part of a multiplet and its cross section was normalized using the statistical model. In this work, the ENSDF value of $\delta_\gamma = 0.19(6)$ [3] for the multipole-mixing ratio (adopted on the basis of subshell ratios from Reference [60]) was used to arrive at a conversion coefficient of $\alpha = 11.96$ for this transition. Another value for the mixing ratio, $\delta_\gamma = 0.9(2)$, has

been proposed [3] based on the value of $\alpha_{L1} = 0.93(13)$ from Reference [60], which would result in a conversion coefficient of $\alpha = 12.82$ and further increase the depopulation of the 174.1-keV level. Finally, the possibility of an unobserved 27.8-keV $M1$ transition from the 174.1-keV level to the $J^{\pi} = 3^{-}$, 146.2-keV level suggests that the agreement in the P-D plot for the 174.1-keV level could be maintained with the inclusion of significant feeding from the ~186-keV level.

378.5-keV level. For most levels, optimum agreement in the P-D plot is obtained when the mean or limiting values of the experimentally-measured multipole-mixing ratios [3] are used to compute internal conversion coefficients. In cases where adjusting the mixing ratio (within the limits of the uncertainty in the adopted value) significantly improves the agreement between the modeled population and the experimental depopulation, statistical-model calculations may be used to infer better values for the mixing ratios. For the 62.2-keV transition from the 378.5-keV level to the 316.5-keV level, the multipolarity from the ENSDF is given as $M1(+E2)$, with an upper bound on the mixing ratio of $\delta_{\gamma} \leq 1.0$ [3]. Statistical-model results suggest that transition has pure $M1$ multipolarity, because a mixing ratio of $\delta_{\gamma} = 0$ optimizes agreement in the P-D plot for the 378.5-keV level while simultaneously improving agreement for the 316.5-keV level. This improvement is evident from the residuals plots shown in Figure 28.

534.3-keV level. The ENSDF branching ratio for the 259.8-keV γ ray deexciting the 534.3-keV level is quoted as $I_{\gamma} = 31$ (with no stated uncertainty) relative to the intensity of $I_{\gamma} = 100(15)$ for the 360.5-keV γ ray deexciting the same level [3]. The branching ratios in the ENSDF for the 534.3-keV level were determined from the work of Lanier *et al.*, in which prompt γ-ray spectra from (n, γ) reactions on ^{185}Re were measured using a bent-crystal spectrometer [60], and are not reported elsewhere in the literature. The 259.8-keV γ ray is part of a multiplet, and

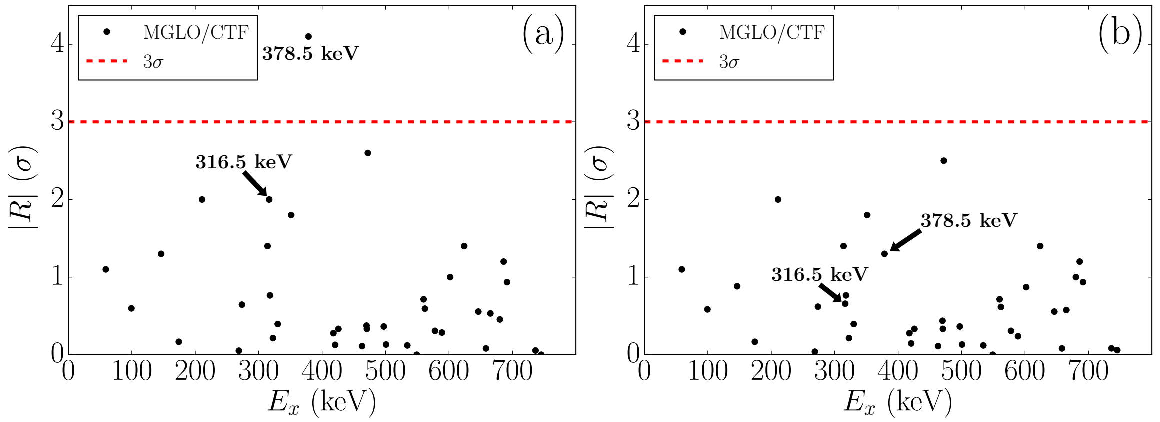

Figure 28. Plots of the absolute value of the residual difference $|R|$, in units of standard deviations σ, between the modeled population and experimental depopulation as a function of level excitation energy E_x, assuming (a) mixed $M1 + E2$ character for the 62.2-keV transition deexciting the 378.5-keV level with a mixing ratio of $\delta_\gamma = 1.0$ [3], and (b) pure $M1$ character ($\delta_\gamma = 0$) for this transition. The horizontal dashed line identifies a residual difference of 3σ. Both plots result from statistical-model calculations with the J^π assignments from Table 7 assumed, using the MGLO model with $k_0 = 2.9$ for the PSF and the CTF model for the LD with the parameterization described in Reference [114].

normalizing its partial cross section to that of the 360.5-keV γ ray using the ENSDF branching ratios results in a modeled population that exceeds the experimental depopulation by a residual difference of 3.5σ. The 534.3-keV level is fed by a relatively strong $E1$ primary transition with $E_\gamma = 5645.07(20)$ keV, so increasing the spin from its adopted assignment of $J^\pi = (4)^-$ to improve agreement in the P-D plot is not possible. Agreement between the modeled population and experimental depopulation for the 534.3-keV level, as well as the 378.5-keV level fed by the 259.8-keV γ ray, is optimized when the branching ratio is adjusted to $I_\gamma = 80(10)$ relative to the intensity of the 360.5-keV γ ray stated above. On the basis of the observed improvement in the P-D plot, we assess that the branching ratios in the ENSDF for this level may be incorrect, and we have adopted the revised value of the relative intensity, $I_\gamma = 80(10)$, for statistical-model calculations in this work. A possible alternative explanation for the lack of agreement observed in the P-D plot could be an unplaced γ ray that deexcites the 534.3-keV level.

4.5.2 Total Radiative Thermal-neutron Capture Cross Section for $^{185}\mathbf{Re}(n,\gamma)$.

After arriving at a list of partial γ-ray production cross sections σ_γ and making the adjustments to the level scheme described above, DICEBOX was used to compute the fraction P_0 of the total capture cross section σ_0 resulting from ground-state feeding from the quasicontinuum. The sum of the internal-conversion-corrected experimental cross sections $\sum_i \sigma_{\gamma i0}^{\exp}(1+\alpha_i)$ for feeding the ground state from levels below $E_c = 746$ keV was used with the calculated value of P_0 in Equation (56) to calculate a total $^{185}\mathrm{Re}(n,\gamma)$ thermal-neutron capture cross section σ_0 for a variety of PSF and LD model combinations. The agreement between the calculated mean s-wave resonance radiative width Γ_0 and the adopted value of $\langle\Gamma_0\rangle = 56(3)$ meV [111] was also used to assess the choices of LD and PSF models and parameters used in the calculations. The results of these calculations are shown in Table 8.

It is evident from Table 8 that the particular choices of PSF and LD models and LD parameterization used do not produce statistically-significant changes in the value of σ_0, which permits the determination of a model-independent value for σ_0. However, the s-wave resonance radiative width Γ_0 is relatively sensitive to the choices of PSF and LD models. This observed sensitivity in the calculated value of Γ_0 to the choice of models has been observed previously in studies involving the tungsten [8, 90] and palladium [87] isotopes. The best agreement in the P-D plots was consistently achieved with the MGLO/CTF combination of PSF/LD models, using the LD parameterization from Reference [114], while the KMF/BSFG model combination with the LD parameters from Reference [114] most accurately

Table 8. Total radiative thermal-neutron capture cross sections (σ_0), simulated fractions of transitions from the quasicontinuum to the ground state (P_0), and mean $s-$wave resonance radiative widths (Γ_0), corresponding to various combinations of $E1$ PSF and LD models and LD parameterizations. Fluctuations in Γ_0 and P_0, which lead to the uncertainties in the tabulated values, result from different nuclear realizations. For each combination, the sum of the internal-conversion-corrected experimentally-measured cross sections from levels below $E_c = 746$ keV directly to the ground state is $\sum_i \sigma_{\gamma_i 0}^{\text{exp}}(1+\alpha_i) = 106.8(57)$ b.

PSF/LD	P_0	σ_0 (b)	Γ_0 (meV)
MGLO/CTF[a]	0.0400(59)	111.2(60)	43.8(9)
MGLO/CTF[b]	0.0380(57)	111.0(59)	39.6(7)
MGLO/BSFG[a]	0.0366(51)	110.9(59)	78.6(9)
MGLO/BSFG[b]	0.0337(50)	110.5(59)	101.8(25)
GLO/CTF[a]	0.0395(55)	111.2(60)	27.6(4)
GLO/CTF[b]	0.0376(56)	111.0(59)	25.4(3)
GLO/BSFG[a]	0.0360(52)	110.8(59)	48.8(4)
GLO/BSFG[b]	0.0334(42)	110.5(59)	62.6(11)
KMF/CTF[a]	0.0409(61)	111.3(60)	32.7(6)
KMF/CTF[b]	0.0392(53)	111.1(60)	29.4(5)
KMF/BSFG[a]	0.0376(51)	111.0(59)	58.7(6)
KMF/BSFG[b]	0.0342(44)	110.6(59)	74.9(17)
BA/CTF[a]	0.0403(75)	111.3(60)	89.4(23)
BA/CTF[b]	0.0376(66)	111.0(60)	75.1(16)
BA/BSFG[a]	0.0367(60)	110.9(59)	164.5(21)
BA/BSFG[b]	0.0332(65)	110.5(59)	204.4(60)

[a] Assuming the LD parameterization from Reference [114].
[b] Assuming the LD parameterization from Reference [115].

reproduced the literature value of Γ_0. We tested parity-dependent as well as parity-independent LD models in this work, and the results for these two options are fully consistent. The values for P_0 from Table 8 were used to obtain a model-independent total radiative thermal-neutron capture cross section of $\sigma_0 = 111(6)$ b, which is in perfect agreement with the adopted value of $\sigma_0 = 112(2)$ b from Reference [111]. This value is also statistically consistent with each of the previous cross section measurements listed in Table 9.

The stability in the value of σ_0 as a function of E_c, which is similar to the behavior observed in the tungsten isotopes investigated in References [8, 90], is shown in Figure 29. It is evident from Figure 29 that the experimental contribution

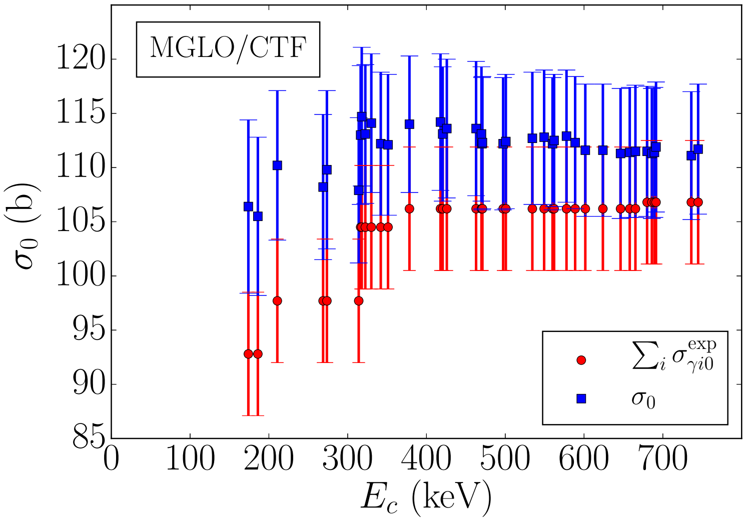

Figure 29. Plot of the variation in the total radiative-capture cross section $\boldsymbol{\sigma_0}$ and the sum of the experimental cross sections $\sum_i \boldsymbol{\sigma_{\gamma i0}^{\mathrm{exp}}}$ for feeding the ground state as a function of the critical energy $\boldsymbol{E_c}$, assuming the MGLO/CTF combination of PSF/LD models with an enhancement factor of $\boldsymbol{k_0 = 2.9}$ and the LD parameterization from Reference [114].

$\sum_i \sigma_{\gamma i0}^{\mathrm{exp}}(1+\alpha_i)$ and σ_0 have converged to a statistically-consistent value by $E_c = 317$ keV, though the study described in this work was extended up to $E_c = 746$ keV to make a more complete assessment of the ^{186}Re level scheme.

4.5.3 Neutron-separation Energy for ^{186}Re.

The primary γ rays listed in Table 6, a subset of which is shown in Figure 21, were used to determine the neutron separation energy S_n for ^{186}Re by applying a global least-squares fit to the level energies from References [3, 63], including a correction for nuclear recoil. The resulting value for the neutron separation energy is $S_n = 6179.59(5)$ keV. This value is reasonably consistent with the adopted value $S_n = 6179.35(18)$ keV from the 2012 Atomic Mass Evaluation (AME) [44], but the uncertainty on the value measured in this work is significantly smaller than the adopted value. The least-squares fit also produced smaller uncertainties in the excitation energies of known levels, listed in Table 6, than those reported in the adopted level scheme [3].

4.6 Conclusions

Past measurements of the total radiative thermal-neutron capture cross section for ^{185}Re have primarily been performed using neutron activation techniques. The neutron activation method requires precise knowledge of the neutron flux incident on the target, and determination of the cross section typically involves corrections for fast and epithermal contributions to the flux. In this work, we used the PGAA technique to measure γ-ray production cross sections for the ^{185}Re(n,γ) reaction, standardized using known ^{35}Cl(n,γ) cross sections from measurements with a stoichiometric $^{\mathrm{nat}}$ReCl$_3$ target. The measured partial cross sections were combined with statistical-decay modeling to calculate a total radiative thermal-neutron capture cross section of $\sigma_0 = 111(6)$ b for ^{185}Re(n,γ), which independently confirms the results of earlier measurements made using activation and pile oscillator techniques. The existing literature values for σ_0 are compared with the measurement from this work in Table 9.

Spectroscopic analysis of the experimental prompt γ-ray data resulted in the discovery of 50 newly-observed primary γ rays, which were combined with literature values for discrete-level energies in ^{186}Re to arrive at a new measurement of 6179.59(5) keV for the neutron separation energy in ^{186}Re. The independent measurement from this work, which has a smaller uncertainty than the adopted value from the 2012 AME [44], provides a useful input to future atomic mass evaluations.

Comparison of the modeled population, calculated using the DICEBOX code,

Table 9. Summary of total thermal-neutron capture cross section (σ_0) measurements on ^{185}Re.

Reference	Method	σ_0 (b)
This work	**PGAA**	**111(6)**
Mughabghab [111]	Evaluation	112(2)
Seren *et al.* [130]	Activation	101(20)
Pomerance [131]	Pile oscillator	100(8)
Lyon [132]	Activation	127.0(127)
Karam *et al.* [133]	Activation	96.5(100)
Friesenhahn *et al.* [134]	Activation	105(10)
Heft [135]	Activation	116(5)
De Corte *et al.* [136]	Activation	112(18)[a]
Hayakawa *et al.* [17]	Activation	132(26)
Farina-Arbocco *et al.* [137]	Activation	111.6(11)

[a] Calculated using I_0 from Reference [111].

with the experimentally-measured depopulation for individual levels is a powerful tool for evaluating the accuracy and completeness of nuclear-structure information. The results presented in this work include proposed adjustments to seven level J^π assignments and confirmation of all other tentative J^π assignments in the ^{186}Re level scheme [3] below an excitation energy of 746 keV. These results, combined with reduced uncertainties in level energies resulting from the global least-squares fit to the γ-ray and level energies, represent significant improvements to the ^{186}Re level scheme.

V. $(d,2n)$ Reactions on ^{186}W

The lack of useful γ-γ coincidence data from the GEANIE experiment described in Chapter III severely limited the ability to place new transitions in the ^{186}Re level scheme. The desire to uncover more of the structure above the isomer in ^{186}Re, and in particular to search for IS that could enable isomer depletion, led to experiments designed to measure γ-ray coincidences from $(d,2n)$ reactions on ^{186}W using detector arrays with higher efficiencies than GEANIE. The analysis of the data obtained from these experiments resulted in a draft manuscript, which is in preparation for submission to Physical Review C. This chapter contains the full text of the draft manuscript, titled “In-beam spectroscopy of medium-spin states in ^{186}Re.”

The draft manuscript was prepared by the primary author, who was responsible for the analysis of the data from the two experiments described in this work. F. G. Kondev of Argonne National Laboratory (ANL) was the principal investigator both experiments, and his direction and oversight were essential to the data analysis and manuscript preparation. M. P. Carpenter of ANL oversaw the CAGRA experimental campaign at RCNP and built the data acquisition system, and he provided essential direction to the primary author for sorting and analyzing the data from this experiment. J. J. Carroll of ARL participated in the CAGRA experiment, and together with C. J. Chiara provided key insights and direction to the primary author during the data analysis and manuscript preparation. J. W. McClory of AFIT provided guidance during the data analysis and reviewed the draft manuscript. G. D. Dracoulis, G. J. Lane, A. P. Byrne, P. M. Davidson, T. Kibédi, P. Nieminen, A. N. Wilson, and R. O Hughes, all of ANU, participated in the experiment there involving the CAESAR detector array. E. Ideguchi, Y. Fang, Y. Yamamoto, H. J. Ong, D. T. Tran, N. Aoi, S. Kanaya, and A. Odahara of Osaka University, Japan, ran the CAGRA experimental campaign. S. Noji and Y. Ayyad of the National Superconducting Cyclotron Laboratory at Michigan State University also participated in the CAGRA campaign. H. Watanabe, currently of RIKEN, Japan, participated in both the ANU and RCNP experiments. S. Zhu, R. V. F. Janssens, T. Lauritsen, C. R. Hoffman and B. P. Kay of ANL were responsible for key aspects of the CAGRA experimental campaign.

5.1 Abstract

Excited states in ^{186}Re with spins up to $J = 12\hbar$ were investigated in two separate experiments that involved measuring γ-ray coincidences from ^{186}W$(d, 2n)$ reactions at deuteron energies of 12.5 MeV and 14.5 MeV. Two- and three-fold coincidence data were collected using the CAESAR and CAGRA spectrometers, respectively, both high-efficiency Compton-suppressed HPGe detector arrays. Analysis of the data revealed six rotational bands built on medium-spin intrinsic states, including the astrophysically-important $K^{\pi} = (8^{+})$ isomer. Additions to the ^{186}Re level scheme include 26 γ rays and 12 levels not previously reported. Band assignments were supported by an analysis of $g_K - g_R$ values, and experimental intrinsic-state energies were compared with the results of multi-quasiparticle blocked BCS calculations based on the Lipkin-Nogami method.

5.2 Introduction

The low-spin structure of ^{186}Re has been previously investigated using (n, γ), (n, p), (n, t), (d, p), and (p, d) reactions [21, 43, 60, 61, 62, 63], while limited experimental work has informed the study of higher-spin states in this nucleus. As a result, the evaluated level scheme [3] is relatively well-developed in the low-spin $(J \leq 6\hbar)$ region, but little information exists on states at higher spins. A recent experiment involving ^{187}Re$(n, 2n)$ reactions revealed several new levels and transitions assessed as feeding the long-lived , $K^{\pi} = (8^{+})$ isomer [22], but a lack of useable coincidence data from this experiment limited the placement of new γ rays in the level scheme. Interest in elucidating the structure above the $^{186}\text{Re}^{m}$ isomer motivated experiments involving $^{186}\text{W}(d, 2n)$ reactions using high-efficiency Compton-suppressed HPGe arrays.

Accurate cross sections for producing the $^{186}\text{Re}^{m}$ isomer via slow-neutron capture on ^{185}Re are important to reducing nuclear-physics uncertainties in the $^{187}\text{Re}/^{187}\text{Os}$ cosmochronometer [17]. Previous measurements of this cross section [17, 21] suggest that the $^{186}\text{Re}^{m}$ isomer contributes negligibly to the chronometer error. However, these measurements have been performed using neutron-activation techniques, which are sensitive to the imprecisely-known [21] isomer half-life. Provided pathways for isomer feeding are known, the $^{185}\text{Re}(n, \gamma)^{186}\text{Re}^{m}$ cross section can be calculated using a statistical model of the capture-γ cascade (e.g., Reference [43]) that is independent of the isomer half-life. Of further astrophysical interest is the identification of intermediate states (IS) between the isomer and ground state. At stellar temperatures, the population of the $^{186}\text{Re}^{m}$ isomer might be affected by $^{186}\text{Re}(\gamma, \gamma')^{186}\text{Re}^{m}$ (photoactivation) and $^{186}\text{Re}^{m}(\gamma, \gamma')^{186}\text{Re}$ (photodepletion) reactions. Such thermal coupling between the isomer and ground states has the potential to increase the production of the $^{186}\text{Re}^{m}$ isomer in the nucleosynthesis of ^{187}Re and ^{187}Os. Using methods analogous to those described in Reference [69] for ^{180}Ta and ^{176}Lu, a temperature-dependent effective half-life for ^{186}Re can be estimated given the IS energies. Knowledge of cross sections for production and destruction of the $^{186}\text{Re}^{m}$ isomer would be useful for bounding errors in the $^{187}\text{Re}/^{187}\text{Os}$ chronometer.

5.3 Experiments

The analysis described in this work involved data from two separate experiments, performed at the Australian National University (ANU) and the Research Center for Nuclear Physics (RCNP) at Osaka University, Japan. Both were investigations of $(d, 2n)$ reactions on enriched ^{186}W targets, but beam availability and differences in the individual detector arrays made it advantageous to perform two experiments.

In the first experiment, the 14UD Pelletron accelerator at ANU was used to produce a direct-current deuteron beam at energies ranging from 12 – 18 MeV, which was directed at an 80%-enriched ^{186}W foil target with an areal density of 6 mg/cm^2. The excitation function for the ^{186}W$(d, 2n)$ reaction was mapped in this energy range by collecting and analyzing singles γ-ray spectra. Runs were subsequently performed at a beam current of 0.5 pnA and beam energies of 12.5 MeV and 14.5 MeV, which were chosen to maximize production of the ^{186}Re^m isomer while suppressing other reaction channels (particularly the $(d, 3n)$ channel). The CAESAR detector array was used to collect two-fold (γ-γ) coincidence data over periods of 17.5 h and 33.0 h at deuteron energies of 12.5 MeV and 14.5 MeV, respectively. For this experiment, the CAESAR array consisted of nine Compton-suppressed HPGe detectors and two unsuppressed planar low-energy photon spectrometers (LEPS) [138]. Calibration spectra were recorded using standard ^{133}Ba and ^{152}Eu calibration sources.

The second experiment was performed using the Clover Array Gamma-ray spectrometer at RCNP/RIBF for Advanced research (CAGRA). The CAGRA array was developed jointly between the U.S. and Japan and consisted of 16 Clover-type HPGe detectors, Compton-suppressed using bismuth germanate shields. The detectors were arrayed such that four each were angled at 45° and 135° to the incident beam path, and eight were oriented at 90° to the beam. The target used in the RCNP experiment was identical to that used in the ANU experiment, and it was centrally positioned inside the CAGRA array at a distance of approximately 14 cm from each detector face. The ring cyclotron at RCNP [139] was used to accelerate deuterons to 14.5 MeV, and the target was irradiated for seven days at an average beam current of between 1.0 – 2.5 pnA. Two-fold and higher data were collected with the CAGRA spectrometer, which was also calibrated using standard ^{133}Ba and ^{152}Eu calibration sources.

5.4 Analysis and Results

The γ-ray coincidence data from the CAESAR array were sorted into symmetrized two-dimensional E_γ-E_γ histograms (matrices), while the prompt γ-ray events from CAGRA were sorted into a three-dimensional E_γ-E_γ-E_γ histogram (cube). Analysis of matrices from CAESAR was performed using the Escl8r program from the Radware analysis package [81, 140, 141], and the cube from CAGRA was analyzed with the levit8r program. The partial level scheme for ^{186}Re determined in this work, which includes the rotational bands built on intrinsic states with $K \geq 4$, is displayed in Figure 30. The level scheme was constructed on the basis of observed γ-ray coincidence relationships in the two-fold data from CAESAR, and γ-ray placements were supported by a parallel analysis of the three-fold data from CAGRA. For γ rays with $E_\gamma > 100$ keV the statistical uncertainty in the transition energies is ±0.5 keV, while those γ rays with $E_\gamma < 100$ keV were measured with the LEPS detectors and are stated with an uncertainty of ±0.2 keV.

Gates on the known 141.1-keV and 144.0-keV transitions [Figure 31(a)] from the adopted level scheme [3] revealed states in a band built on the 324.4-keV level. The energy of this state, which was previously known only approximately, was

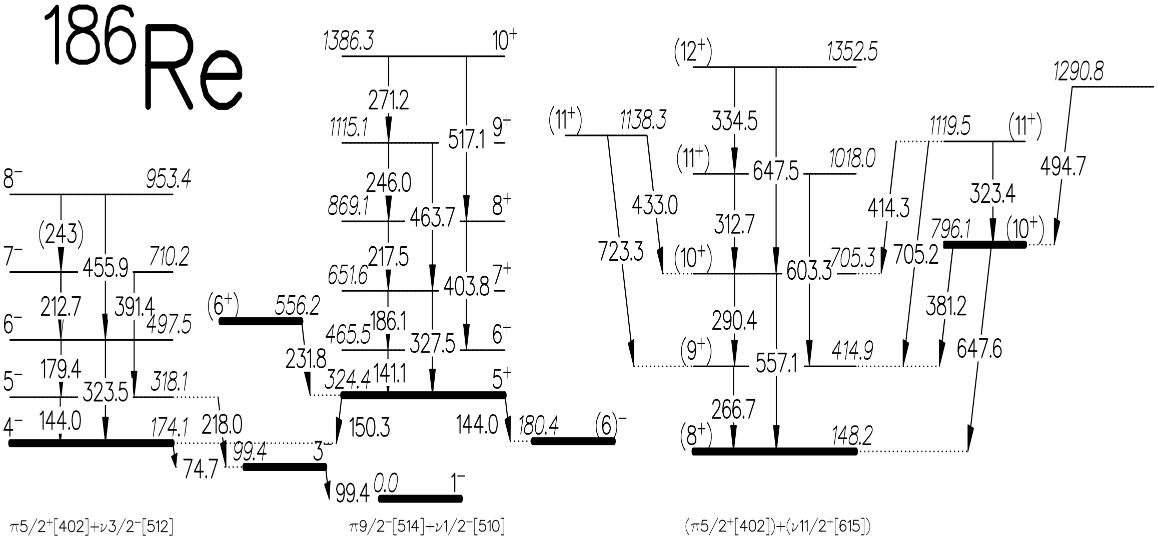

Figure 30. Partial ^{186}Re level scheme from the present work, with measured γ-ray transition energies in plain text and level energies in italics. Tentative transitions and assignments are identified with parentheses. The $J^\pi = 3^-$ level at 99.4 keV is shown to illustrate the decay path to the 1^- ground state from the 5^+, 324.4-keV level through the 4^-, 174.1-keV level. The proposed configurations discussed in the text for the $K^\pi = 4^-$, 5^+, and (8^+) bands are listed at the bottom of the figure.

established on the basis of an observed 150.3-keV γ ray that is part of a γ-ray cascade to the ground state. Placement of the 150.3-keV γ-ray also helped establish the energies of the 180.4 keV, 465.5 keV, and 556.2 keV states, which are listed as approximate in the ENSDF [3, 4].

The $J^\pi = 5^+$ and $J^\pi = (6)^-$ assignments for the 324.4-keV and 180.4-keV levels are supported by $E1$ multipolarities of the 150.3-keV and 144.0-keV transitions, which were deduced from balancing the relative intensities of the low-energy transitions into and out of the 324.4-keV level. Internal conversion was assumed to be responsible for the difference between the measured incoming and outgoing γ-ray intensities, which permitted extraction of the internal-conversion coefficients for comparison with coefficients calculated using BrIcc [28, 29]. Relative transition intensities, corrected for detector efficiency, were measured by fitting spectra obtained from gating on the 186.1-keV γ ray in the CAESAR coincidence data. From this analysis, which is summarized in Table 10, we concluded that both the

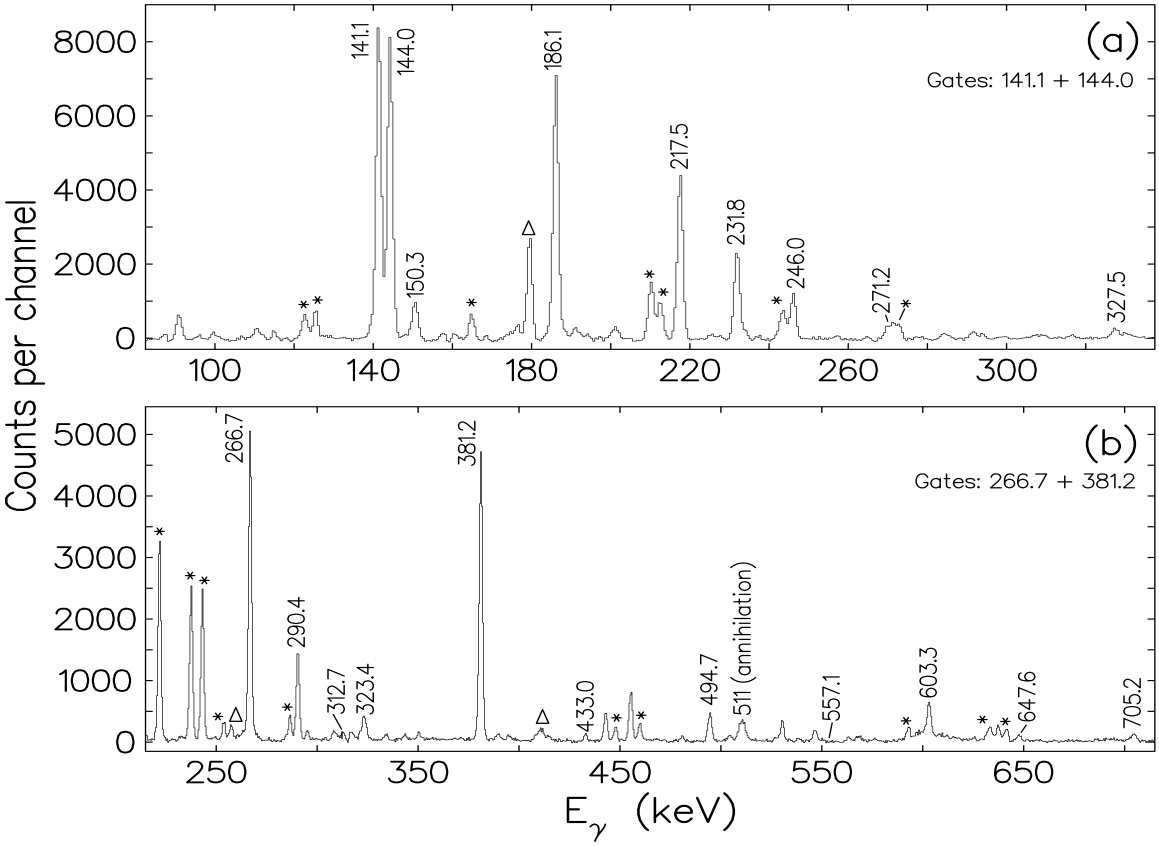

Figure 31. Representative gated γ-ray spectra from the coincidence data obtained with the CAESAR spectrometer, showing (a) the sum of gates on the 141.1-keV and 144.0-keV γ rays, and (b) the sum of gates on the 266.7-keV and 381.2-keV γ rays. Contaminant γ-ray peaks are identified with asterisks (*), while other γ rays in ^{186}Re not connected to the $K \geq 4$ bands of Figure 30 are labeled with triangles ($\boldsymbol{\Delta}$).

144.0-keV and 150.3-keV transitions have pure $E1$ character.

Isomer feeding via a 266.7-keV γ ray from a $J^\pi = (9^+)$ level at 414.9 keV and 381.2- and 647.6-keV γ rays from a $J^\pi = (10^+)$ level at 796.1 keV was proposed in Reference [22] on the basis of an analysis of ^{187}Re$(n, 2n\gamma)$ excitation functions. Gates on the 266.7-keV and 381.2-keV γ rays in the CAESAR γ-γ coincidence data revealed other γ rays likely involved in feeding the isomer, both intra-band and inter-band, shown in Figure 31(b). A double gate on the strong 266.7-keV and 381.2-keV γ rays in the CAGRA γ-γ-γ coincidence data revealed transitions at 323.4 keV and 494.7 keV, which established the existence of levels at 1119.5 keV

Table 10. Relative γ-ray intensities (I_γ) for the 141.1-, 144.0-, and 150.3-keV γ rays, measured by gating on the 186.1-keV γ ray in the CAESAR coincidence data. The internal-conversion-corrected intensities $I_\gamma(1+\alpha)$ for transitions feeding and deexciting the 324.4-keV level are shown for a variety of assumed transition multipolarities $M\lambda$ for the 144.0-keV and 150.3-keV transitions. Internal-conversion coefficients (α) were calculated using BrIcc [28]. The summed intensity of the outgoing 144.0-keV and 150.3-keV transitions most closely matches the incoming intensity due to the 141.1-keV transition when the outgoing transitions both have pure $E1$ character (identified with bold text).

E_γ [keV]	I_γ [arb.]	$M\lambda$	α	$I_\gamma(1+\alpha)$
141.1(5)	1.10(6)	$M1+E2$	1.56(2)^a	2.82(16)
144.0(5)	2.43(12)	**$E1$**	**0.150(2)**	**2.79(14)**
		$M1$	1.83(2)	6.88(3)
		$E2$	1.02(1)	4.91(24)
150.3(5)	0.32(2)	**$E1$**	**0.134(2)**	**0.36(2)**
		$M1$	1.62(2)	0.83(5)
		$E2$	0.87(1)	0.60(4)

^{a}Multipole-mixing ratio $\delta = 0.9$ [3] used to calculate α

and 1290.8 keV.

5.5 Discussion

A discussion of the evidence supporting the level assignments proposed in this work (shown in Figure 30) follows in this section. Level configurations and band assignments were motivated by a comparison of experimental level energies with the results of multi-quasiparticle Nilsson-type calculations, as well as an analysis of measured and calculated g-factors for each rotational band.

5.5.1 Multi-quasiparticle Blocking Calculations.

Multi-quasiparticle blocked BCS calculations were performed to arrive at energies of intrinsic states in ^{186}Re for comparison with experimental level energies. The results of the calculations are listed in Table 11 together with the experimental data. The technique for calculating the intrinsic-state energies involved first producing a set of basis states by calculating the Nilsson levels at the equilibrium deformation parameters $\varepsilon_2 = 0.200$ and $\varepsilon_4 = 0.093$ from Reference [142]. This was followed by adjusting the level energies near the Fermi surface to reproduce the average experimental one-quasiparticle energies in ^{185,187}Re (for neutrons) and ^{187}W, ^{187}Os (for protons). Pairing correlations were handled using the Lipkin-Nogami prescription, as described in Reference [143], with fixed monopole pairing strengths $G_\nu = 18.0/A$ and $G_\pi = 20.8/A$. Finally, the predicted energies of the multi-quasiparticle states were corrected for residual interactions using the methods described in Reference [144]. In most cases, agreement within 100 keV between the experimental and calculated level energies was achieved for levels below 1 MeV.

5.5.2 Branching Ratios and $g_K - g_R$ Analysis.

Rotational-band configurations have been supported in previous studies by an analysis of $g_K - g_R$ values [37, 38, 39, 40]. In the rotational model of the nucleus, the difference $g_K - g_R$ between the intrinsic and rotational g-factors should be a constant for all the rotational states in a given band [37]. The magnitude of the quantity $\left|\frac{g_K - g_R}{Q_0}\right|$, where Q_0 is the intrinsic quadrupole moment, can be determined from experimental measurements of γ-ray branching ratios for intra-band $\Delta J = 1$ and $\Delta J = 2$ transitions deexciting a particular state. This value is given by the expression

$$\left|\frac{g_K - g_R}{Q_0}\right| = 0.933\frac{E_1}{\delta\sqrt{J^2 - 1}}, \tag{61}$$

in which E_1 is the energy of the $\Delta J = 1$ transition in MeV, J is the initial-level spin, and the $M1 + E2$ multipole-mixing ratio δ can be determined (up to its sign)

Table 11. Selected two-quasiparticle states in ^{186}Re. Calculated intrinsic-state energies (E_{calc}) include the modeled two-quasiparticle energies E_{qp} combined with the strength of the residual interaction E_{res} as described in the text. The calculated values are compared with experimental results from this work for states with $K \geq 4$. Lower-K states are listed with energies and configurations taken from literature [3, 43, 61] to show agreement with the calculations.

K^π	Configuration		E_{qp}	E_{res}	$E_{\mathrm{calc}}{}^{a}$	E_{exp}
	π	ν			[keV]	
1^-	$5/2^+[402]$	$3/2^-[512]$	0	-78	0	0.0
4^-	$5/2^+[402]$	$3/2^-[512]$	0	78	156	174.1
3^-	$5/2^+[402]$	$1/2^-[510]$	26	-55	49	99.4
2^-	$5/2^+[402]$	$1/2^-[510]$	26	55	159	$210.699^{b,c}$
8^+	$5/2^+[402]$	$11/2^+[615]$	201	-125	154	148.2^{d}
3^+	$5/2^+[402]$	$11/2^+[615]$	201	125	403	$314.009^{b,c}$
6^-	$5/2^+[402]$	$7/2^-[503]$	245	-97	227	180.4^{d}
1^-	$5/2^+[402]$	$7/2^-[503]$	245	97	420	$316.463^{b,c}$
2^-	$5/2^+[402]$	$9/2^-[505]$	784	-75	788	$577.723^{b,c}$
7^-	$5/2^+[402]$	$9/2^-[505]$	784	75	937	
6^+	$9/2^-[514]$	$3/2^-[512]$	286	-77	288	556.2^{d}
3^+	$9/2^-[514]$	$3/2^-[512]$	286	77	441	$351.202^{b,c}$
5^+	$9/2^-[514]$	$1/2^-[510]$	312	-72	319	324.4
4^+	$9/2^-[514]$	$1/2^-[510]$	312	72	462	$425.823^{b,e}$
10^-	$9/2^-[514]$	$11/2^+[615]$	487	-143	422	
1^-	$9/2^-[514]$	$11/2^+[615]$	487	143	707	$761.42^{b,f}$
8^+	$9/2^-[514]$	$7/2^-[503]$	531	-107	502	
1^+	$9/2^-[514]$	$7/2^-[503]$	531	107	716	$601.58^{b,c}$
0^+	$9/2^-[514]$	$9/2^-[505]$	1070	-107	1041	
9^+	$9/2^-[514]$	$9/2^-[505]$	1070	107	1255	

[a] Calculated energies relative to the $K^\pi = 1^-$ state,
$E_{\mathrm{qp}}(1^-) + E_{\mathrm{res}}(1^-) = -78$ keV

[b] Level energy from ENSDF [3]

[c] K^π assignment from Reference [61]

[d] K^π assignment proposed as tentative in this work

[e] K^π assignment from Reference [43]

[f] J^π assignment listed in ENSDF as $(1^-,2^-,3^-)$ [3]

from the equation

$$\frac{\delta^2}{1+\delta^2} = \frac{2K^2(2J-1)}{(J-K-1)(J+K-1)(J+1)} \left(\frac{E_1}{E_2}\right)^5 \frac{T_2}{T_1}. \qquad (62)$$

In Equation (62), K is the spin of the band head, E_2 is the energy of the $\Delta J = 2$ transition, and T_2/T_1 is the ratio of the γ-ray intensities of the $\Delta J = 2$ and $\Delta J = 1$ transitions [40]. The intrinsic quadrupole moment $Q_0 = 6.18(6)$ eb was determined from the ENSDF value for the quadrupole moment $Q = +0.618(6)$ eb of the $J^\pi = 1^-$ ground state [3] using the rotational-model expression from Reference [33],

$$Q_0 = \frac{(J+1)(2J+3)}{3K^2 - J(J+1)} Q. \tag{63}$$

Experimental $|g_K - g_R|$ values obtained using Equations (61) and (62) were compared with calculated values for the proposed Nilsson configurations of each rotational band. The intrinsic g-factors for two-quasiparticle states in ^{186}Re were obtained from those of the proton (π) and neutron (ν) orbitals via the expression

$$g_K = \frac{\Omega_\pi (g_K)_\pi + \Omega_\nu (g_K)_\nu}{K}, \tag{64}$$

where the Ω_i are the proton and neutron spin projections on the axis of nuclear symmetry, so that $K = \Omega_\pi + \Omega_\nu$. The g_K values for the single-nucleon orbitals were calculated using the following prescription:

$$g_K = g_\Lambda + (g_\Sigma - g_\Lambda) \frac{\langle s_3 \rangle}{\Omega}, \tag{65}$$

where the orbital g-factor is

$$g_\Lambda = \begin{cases} 0 & \text{for neutrons} \\ 1 & \text{for protons,} \end{cases} \tag{66}$$

and the intrinsic g-factors for neutrons and protons are equal to 0.7 times their free

Table 12. Gamma-ray energies E_2 and E_1, and branching ratios T_2/T_1 for intra-band $\Delta J = 2$ and $\Delta J = 1$ transitions used to determine experimental $|g_K - g_R|$ values for the $K^\pi = 4^-$, 5^+, and (8^+) rotational bands in ^{186}Re. Calculated $g_K - g_R$ values are included for comparison with the weighted means of the experimental values for each band.

Band K^π [$\hbar$]	E_i [keV]	J_i^π [$\hbar$]	E_1 [keV]	E_2 [keV]	T_2/T_1	$\lvert g_K - g_R\rvert_{\text{exp}}{}^a$	$(g_K - g_R)_{\text{calc}}{}^b$
4^-	497.3	6^-	179.2(5)	323.5(5)	0.26(2)	0.82(3)	0.93
				Weighted mean:		0.82(3)	
5^+	651.6	7^+	186.1(5)	327.5(5)	0.053(5)	1.008(56)	0.73
	869.1	8^+	217.5(5)	403.8(5)	0.140(14)	1.054(62)	
	1115.1	9^+	246.0(5)	463.7(5)	0.50(5)	0.721(46)	
	1386.3	10^+	271.2(5)	517.1(5)	1.18(11)	0.563(32)	
				Weighted mean:		0.73(5)	
(8^+)	705.3	10^+	290.4(5)	557.1(5)	1.60(13)	0.084(17)	0.05
	1018.0	11^+	312.7(5)	603.3(5)	0.30(5)	0.09(4)	
				Weighted mean:		0.08(3)	

[a] Determined using $Q_0 = 6.18(6)$ eb [3, 33]

[b] Calculated using $g_R = 0.28$ [36]

values of -3.83 and +5.59, respectively [40]:

$$g_\Sigma = \begin{cases} -2.681 & \text{for neutrons} \\ 3.913 & \text{for protons.} \end{cases} \tag{67}$$

The quantity $\langle s_3 \rangle$ is the expectation value of the intrinsic-spin projection on the deformation axis [40]. The prescription above was applied in Woods-Saxon calculations with deformation parameters $\beta_2 = 0.221$, $\beta_4 = -0.094$, and $\beta_6 = 0.010$ [30] to yield theoretical g_K values. These g_K values were applied with $g_R = 0.28$ determined using the standard approximation $g_R = 0.7Z/A$ [36] to arrive at the values of $g_K - g_R$ listed in Table 12.

Intra-band branching-ratio data were limited due to the fact that gates were routinely contaminated with ^{185}Re γ rays from the ^{186}W$(d, 3n)$ reaction channel. The results of Table 12 show agreement between the measured and calculated $|g_K - g_R|$ values for the $K^\pi = 5^+$ and (8^+) bands, supporting the Nilsson configurations in Figure 30 and Table 11 for these bands. In the case of the $K^\pi = 4^-$ band, where the calculated and experimental $g_K - g_R$ values disagree, the discrepancy is not large enough to suggest an alternative configuration to that proposed here without additional branching-ratio data.

5.5.3 Configuration Assignments.

Much of the band structure and intrinsic-state configurations in the adopted level scheme [3] are from the work of J. Glatz [61], which involved an analysis of prompt and delayed γ-γ coincidences following slow-neutron capture on ^{185}Re. The known low-spin structure of ^{186}Re can be described generally by the coupling of a proton in the $5/2^+[402]$ orbital to neutrons in the $1/2^-[510]$, $3/2^-[512]$, $7/2^-[503]$, and $9/2^-[505]$ orbitals. Due to Coriolis mixing, transitions between levels in different rotational bands that are built on these states are numerous [61]. Transitions between the lower-K bands and those built on higher-spin intrinsic states with neutrons in the $11/2^+[615]$ orbital or protons in the $9/2^-[514]$ orbital generally have $|\Delta K| > 1$, so Coriolis mixing is forbidden. These bands are not as well-studied as those built on the low-K states, since higher-spin states are not strongly populated in (n, γ) reactions. A discussion of the bands that appear in Figure 30, which are the subject of this work, follows.

$K^\pi = 5^+$ band and $K^\pi = (6^+)$, $(6)^-$ levels.

The adopted level scheme for ^{186}Re includes unconfirmed levels at ~330, ~471, and ~562 keV that are expected to deexcite through a $J^\pi = (6)^-$ level at

$\sim$186 keV [3]. The adopted spin-parity assignments for the $\sim$330, $\sim$471, and $\sim$562 keV levels are $(5)^+$, $(4)^+$ and (6^+), respectively [3], though Matters *et al.* proposed a revised assignment of $J^\pi = 6^+$ for the $\sim$471-keV level on the basis of statistical modeling of the ^{185}Re$(n, \gamma)^{186}$Re cascade [43].

Observation of a 150.3-keV γ-ray in coincidence with the 141.1-keV γ ray and the other transitions in the $K^\pi = 5^+$ band connects the previously-unconfirmed level at $\sim$330 keV to the $J^\pi = 4^-$, 174.1-keV level from the adopted level scheme [3]. As described earlier, this establishes the energy of the $J^\pi = 5^+$ state at 324.4 keV as well as the energies of the $K^\pi = (6)^-$ and (6^+) levels. Observed γ-ray coincidences support the placement of the $\sim$471-keV level in the rotational band built on the 324.4 keV state, which confirms the $J^\pi = 6^+$ assignment proposed in Reference [43] for this level and leads to an improved excitation energy of 465.5 keV.

The proposed Nilsson configurations for the $K^\pi = 5^+$ and $(6)^-$ states listed in Table 11 result in excellent agreement between the empirical excitation energies from this work and the calculated values. However, in the case of the 556.2-keV level, a $J^\pi = (6^+)$ assignment as in Reference [3] leads to a difference of 268.2 keV between the experimental and calculated level energies.

$K^\pi = (8^+)$ band and $K^\pi = (10^+)$, (11^+) levels.

The known level structure of the neighboring odd-odd isotope ^{184}Re was useful as a guide for γ-ray placement and level J^π assignments above the isomer in ^{186}Re. ^{184}Re has a long-lived $J^\pi = 8^{(+)}$ isomer ($T_{1/2} = 169(8)$ d) with an excitation energy of 188.0463(17) keV [84]. The tentative Nilsson configuration for the ^{184}Re^m isomer is $(\pi 5/2^+[402]) + (\nu 11/2^+[615])$ [40, 84], identical to that of the ^{186}Re^m isomer [21, 3], suggesting that the structures above the isomers in ^{184}Re and ^{186}Re share similarities. This configuration in the blocked BCS calculations (Table 11) reproduces the experimental isomer energy of 148.2 keV to within 6 keV.

The placement of γ rays in the isomer band that were observed in the CAESAR and CAGRA data sets in coincidence with the 266.7 keV γ ray differs from the level scheme presented in Reference [22]. The placement presented in this work, in which the 381.2-keV and 647.6-keV γ rays feed the isomer from a $K^\pi = (10^+)$ band, agrees more closely with the known level structure in the isomer band of ^{184}Re [40, 84], and it is supported by the $g_K - g_R$ analysis described above. Observation of a 433.0-keV γ ray in coincidence with the 290.4-keV and 557.1-keV γ rays, together with a 723.3-keV γ ray in coincidence with the 266.7-keV γ ray suggest a level at 1138.3 keV.

Due to differences in spin J and spin projection K, transitions between levels above the isomer and other bands in the ^{186}Re level scheme are likely inhibited by angular-momentum selection rules or additional K-hindrance [31]. For this reason, despite an exhaustive search, no IS with decay branches to both the isomer and ground states were discovered in this work.

5.6 Conclusions

The experiment described in this work is the first investigation of the structure of ^{186}Re using $(d, 2n)$ reactions, leading to the discovery of new medium-spin levels and associated γ ray transitions. The low-spin structure of ^{186}Re has previously been well-studied, but little information about levels feeding the $K^\pi = (8^+)$ isomer has been reported. Information about doorway states through which the isomer can be populated in the γ cascade following slow-neutron capture on ^{185}Re are important for calculating ^{186}Re^m isomer production in the s-process nucleosynthesis of ^{187}Re. The spin difference between the ^{185}Re(n, γ) capture state (an admixture of $J^\pi = 2^+$ and 3^+ states [43, 111]) and these doorway states contributes to their significance in isomer population. In this work, a total of 15 γ-rays and eight levels have been placed above the isomer. These new levels and transitions could inform future studies involving statistical calculations of astrophysically-important reaction cross sections that involve ^{186}Re and its long-lived isomer.

Additionally, new additions to the $K^{\pi} = 5^{+}$ rotational band are proposed in this work, built on the previously-unconfirmed levels at ∼330 keV, ∼471 keV, and ∼562 keV [3]. Energies of these levels and the level at ∼186 keV have been firmly established, and a decay pathway from these levels to the ground state proposed. Further investigation of high-spin states in ^{186}Re using multi-nucleon transfer reactions would be helpful for extending the level scheme further.

This analysis revealed no evidence of coupling between the isomer and ground state in ^{186}Re. This suggests that if IS exist at energies below several MeV, branching to the isomer is probably weak relative to branching to lower-spin states. This observation supports the conclusion of Käppeler *et al.* in Reference [67], that the branching at ^{186}Re contributes insignificantly to the production of ^{187}Re in the s process. Future experiments involving direct measurement of (γ, γ') depletion of the ^{186}Re^{m} isomer, analogous to those described in [68] for ^{180}Ta^{m}, are suggested for verification.

VI. Conclusion

6.1 Summary of Findings

The significant outcome of this research was in enriching the ^{186}Re level scheme. In particular, the structure above the $\sim 2.0 \times 10^5$ y isomer in ^{186}Re has not been proposed before, and new γ-ray transitions observed in the ^{187}Re$(n, 2n\gamma)^{186}$Re and ^{186}W$(d, 2n\gamma)^{186}$Re reactions are evidence of pathways by which the isomer is populated. These proposed transitions lead to an improved estimate of the excitation energy of the ^{186m}Re isomer with an order-of-magnitude smaller uncertainty than the value adopted in the literature. Additionally, independent measurements were made of the ^{186}Re neutron-separation energy and total cross section for thermal-neutron capture on ^{185}Re.

6.1.1 Contributions to the Level Scheme of ^{186}Re.

The new levels and transitions proposed here as a result of analysis of the data from the GEANIE (Chapter III), BNC (Chapter IV), ANU, and CAGRA (Chapter V) experiments are significant additions to the ^{186}Re level scheme. Analysis of the data from the GEANIE experiment involving ^{187}Re$(n, 2n)$ reactions revealed five new transitions and one new level. The analysis of ^{185}Re(n, γ) reactions at BNC led to proposals for revised spin-parity (J^π) assignments for seven levels in the adopted level scheme of ^{186}Re while confirming assignments for 37 other levels. Additionally, 50 new primary transitions that populate discrete low-lying levels directly from the (n, γ) capture state were proposed based on analysis of the BNC data. Measurement of γ-ray coincidence data from $(d, 2n)$ reactions on ^{186}W at ANU and CAGRA led to the placement of 26 new γ-ray transitions and 12 new levels in the ^{186}Re level scheme, including substantial new structure above the

$J^\pi = (8^+)$ isomer.

In the analysis of the data from the GEANIE, ANU, and CAGRA experiments, no γ rays were observed that depopulated any of the states above the isomer to levels that feed the ground state. Such a γ-ray cascade would indicate an IS through which isomer depletion might be achieved, according to the scheme described in Section 2.3.2. The non-observation of IS suggests that coupling between the isomer and the ground state is weak, at least up to the excitation energies that could be accessed in this spectroscopic study.

6.1.2 Improved Estimate of ^{186m}Re Energy.

The adopted value of the ^{186m}Re excitation energy from the ENSDF database is 149 ± 7 keV, the original energy proposed by Seegmiller *et al.* in 1972 [3, 21]. A γ-ray peak at 266.69(4) keV observed in the $^{187}\mathrm{Re}(n, 2n\gamma)^{186}\mathrm{Re}$ reaction channel was proposed in Chapter III to be a transition feeding the isomer from a level at 414.9(5) keV. This places the isomer energy at $414.9(5) - 266.69(4) = 148.2(5)$ keV, which represents significant improvement over the 149(7) keV value in the evaluated database. Observation of this transition was confirmed in the ANU and CAGRA data sets, with a measured energy of 266.7(5) keV.

6.1.3 Measurements of Neutron-capture Cross Section and Separation Energy.

Analysis of the prompt γ-ray spectra from the $^{185}\mathrm{Re}(n, \gamma)$ experiment at BNC, combined with statistical modeling of the capture-γ cascade, resulted in an independent measurement of $\sigma_0 = 111(6)$ b for the total radiative thermal-neutron capture cross section for ^{185}Re. This value is consistent with previous measurements of σ_0, which were primarily made using neutron-activation techniques. The measurement reported in Chapter IV is significant because it demonstrates the accuracy of the PGAA technique for independently measuring σ_0, which is not sensitive to precise knowledge of the neutron flux as are traditional neutron-activation methods.

Measurement of primary γ-ray energies in the prompt-γ spectra from this experiment also permitted an independent measurement of the neutron-separation energy in ^{186}Re. The value obtained in this work, $S_n = 6179.59(5)$ keV, is consistent with the adopted value of $S_n = 6179.35(18)$ keV, but has an uncertainty that is over three times smaller.

6.2 Recommendations for Future Research

Production of an isomeric sample of ^{186m}Re could be accomplished by irradiation of an enriched sample of ^{185}Re in a research reactor. Following sufficient time for the unstable ^{186}Re in the ground state to decay, the remaining ^{186}Re would exist predominantly in the isomer. Future experiments with an isomeric sample would be beneficial for several reasons, outlined below.

6.2.1 Measurement of the ^{186m}Re Isomer Lifetime.

The half-life of ^{186m}Re is not precisely known. Seegmiller *et al.* reported that they measured the isomer half-life twice, once at 2.0×10^5 y and a confirmatory measurement of 1.7×10^5 y [21]. The value in the adopted literature is 2.0×10^5 y, with no stated uncertainty [3]. An average of the measurements of Seegmiller *et al.* suggests this value should be $1.85(15) \times 10^5$ y, a relative uncertainty of 8.1%. The uncertainty on this value could likely be improved with a careful equilibrium measurement of the γ decay following IT using a high-efficiency HPGe detector, combined with mass-spectroscopic measurements to determine the amount of ^{186}Re present in the sample.

6.2.2 Search for IS in ^{186}Re via (γ, γ') Reactions.

Although no IS were discovered in this work, the $J^{\pi} = (6)^{-}$, 180.5-keV level (which has an approximate energy of ∼186 keV in the adopted level scheme [3]) was proposed in References [21, 61] to feed the isomer, making it a possible IS for isomer depletion. The transitions postulated in these works include a 6.6-keV, $E2$ transition to the $J^{\pi} = (4)^{-}$, 173.929-keV level, and a 32.3-keV transition to feed the isomer. If the 180.5-keV level is an IS, irradiation of an isomeric sample with a Bremsstrahlung generator or other high-energy photon source tuned to maximize the photon flux at ∼32 keV would reveal γ rays in the decay of the 173.929-keV level to the ^{186}Re ground state (with γ-ray energies of 74.568 keV, 99.362 keV, 40.350 keV, and 59.009 keV), as well as an increase in the β-decay of the ground state (evident from the 137.157-keV γ-ray activity from the daughter ^{186}Os nucleus [3]). Irradiation at higher energies with a tunable Bremsstrahlung generator might reveal additional isomer-depletion IS.

6.2.3 Measurement of the Lifetime of the 180.5-keV Level.

The 180.5-keV level, which was assessed to have a tenative $J^{\pi} = (6)^{-}$ spin-parity assignment in Reference [60], likely decays via an $M3$ transition to the $J^{\pi} = (3)^{-}$, 99.361-keV level. The postulated 81.1-keV transition is likely too weak to be observed, due to internal conversion ($\alpha = 646.6$, calculated using BrIcc [28]). The 180.5-keV level was calculated in Reference [43] to be strongly populated in (n, γ) reactions, but no transitions out of this level have been placed in the level scheme. It is possible that this level is a second long-lived isomer in ^{186}Re, with an estimated lifetime from the Weisskopf estimates (Equation 6) of 29.5 min. If the 180.5-keV level is an IS, then measurement of γ decay following Bremsstrahlung irradiation of an isomeric sample could reveal the half-life of this state and establish whether or not it is a second long-lived isomer in ^{186}Re.

Bibliography

1. M. Berglund and M. E. Wieser, “Isotopic compositions of the elements 2009 (IUPAC technical report),” *Pure and Applied Chemistry*, vol. 83, no. 2, pp. 307–410, 2011.

2. Royal Society of Chemistry. Periodic table information. [Online]. Available: http://www.rsc.org/periodic-table

3. C. M. Baglin, “Nuclear data sheets for $A = 186$,” *Nuclear Data Sheets*, vol. 99, pp. 1–196, 2003.

4. Evaluated Nuclear Structure Data File (ENSDF). Brookhaven National Laboratory. [Online]. Available: http://www.nndc.bnl.gov/ensdf/

5. A. M. Hurst, “Isotopes project activities at LBNL,” Presentation at the Air Force Institute of Technology, February 2014.

6. N. J. Peters, “Challenges and successes in the application of evaluated nuclear data for the Missouri University,” Presentation at the Nuclear Data Needs and Capabilities for Applications (NDNCA) conference, Berkeley, CA, May 2015.

7. C. Duchemin, A. Guertin, F. Haddad, N. Michel, and V. Métivier, “Cross section measurements of deuteron induced nuclear reactions on natural tungsten up to 34 MeV,” *Applied Radiation and Isotopes*, vol. 97, pp. 52–58, 2015.

8. A. M. Hurst, R. B. Firestone, B. W. Sleaford, N. C. Summers, Z. Révay, L. Szentmiklósi, M. S. Basunia, T. Belgya, J. E. Escher, and M. Krtička, “Investigation of the tungsten isotopes via thermal neutron capture,” *Physical Review C*, vol. 89, p. 014606, 2014.

9. M. B. Chadwick *et al.*, “ENDF/B-VII.1 nuclear data for science and technology: Cross sections, covariances, fission product yields and decay data,” *Nuclear Data Sheets*, vol. 112, no. 12, pp. 2887–2996, December 2011.

10. R. B. Firestone, *Table of Isotopes*, 8th ed., C. M. Baglin, Ed. Wiley Interscience, 1999.

11. D. D. Clayton, “Cosmoradiogenic chronologies of nucleosynthesis,” *The Astrophysical Journal*, vol. 139, pp. 637–663, 1964.

12. K. L. Hainebach and D. N. Schramm, “Galactic evolution models and the rhenium-187/osmium-187 chronometer: A greater age for the galaxy,” *The Astrophysical Journal*, vol. 207, pp. L79–L86, 1976.

13. R. N. Boyd, *An Introduction to Nuclear Astrophysics.* Chicago, IL: University of Chicago Press, 2008.

14. F. Käppeler, S. Jaag, Z. Y. Bao, and G. Reffo, "The *s*-process branchings at ^{185}W and ^{186}Re," *The Astrophysical Journal*, vol. 366, pp. 605–616, 1991.

15. S. E. Woosley and W. A. Fowler, "A nuclear correction factor for Re/Os cosmochronology," *The Astrophysical Journal*, vol. 233, pp. 411–417, 1979.

16. M. Mosconi, "Re/Os cosmochronometer: Measurement of neutron cross sections," Ph.D. dissertation, Universität Karlsruhe, 2007.

17. T. Hayakawa, T. Shizuma, T. Kajino, S. Chiba, N. Shinohara, T. Nakagawa, and T. Arima, "New *s*-process path and its implications for a ^{187}Re-^{187}Os nucleo-cosmochronometer," *The Astrophysical Journal*, vol. 628, pp. 533–540, July 2005.

18. Defense Science Board, "Radionuclide power to lighten the soldiers' load," in *Technology and Innovation Enablers for Superiority in 2030*, 2013, pp. 48–54.

19. P. M. Walker and J. J. Carroll, "Ups and downs of nuclear isomers," *Physics Today*, pp. 39–44, June 2005.

20. J. J. Carroll, "Foundations of isomer physics for high energy density applications," Grant HDTRA 1-08-1-0014, 2010, proposal and final technical progress report covering period March 2008 - December 2010.

21. D. W. Seegmiller, M. Lindner, and R. A. Meyer, "^{186}Re: Nuclear structure and an isomer of half-life 2×10^5 y," *Nuclear Physics A*, vol. 185, pp. 94–112, 1972.

22. D. A. Matters, N. Fotiades, J. J. Carroll, C. J. Chiara, J. W. McClory, T. Kawano, R. O. Nelson, and M. Devlin, "New transitions and feeding of the $J^\pi = (8^+)$ isomer in ^{186}Re," *Physical Review C*, vol. 92, p. 054304, 2015.

23. M. Litz, T. Feroli, G. M. Merkel, N. Guardala, M. Helba, N. R. Pereira, and J. J. Carroll, "Evaluation of ^{166m}Ho: In search of photonuclear cross sections and trigger-level paths," *Laser Physics*, vol. 17, no. 6, pp. 868–873, 2007.

24. W. Greiner and J. A. Maruhn, *Nuclear Models.* Berlin-Heidelberg: Springer-Verlag, 1996.

25. P. Walker and G. Dracoulis, "High-spin nuclear traps," *Physics World*, February 1994.

26. R. F. Casten, *Nuclear Structure from a Simple Perspective*, 2nd ed. New York, NY: Oxford University Press, 2000.

27. K. S. Krane, *Introductory Nuclear Physics.* Hoboken, NJ: John Wiley & Sons, 1987.

28. T. Kibédi, T. Burrows, M. Trzhaskovskaya, P. Davidson, and C. Nestor. (2011, December) BrIcc v2.3S conversion coefficient calculator. [Online]. Available: http://bricc.anu.edu.au/

29. T. Kibédi, T. W. Burrows, M. Trzhaskovskaya, P. Davidson, and C. Nestor, "Evaluation of theoretical conversion coefficients using BrIcc," *Nuclear Instruments and Methods in Physics Research A*, vol. 589, pp. 202 – 229, 2008.

30. P. Möller, A. J. Sierk, T. Ichikawa, and H. Sagawa, "Nuclear ground-state masses and deformations: FRDM(2012)," *Atomic Data and Nuclear Data Tables*, vol. 109–110, pp. 1–204, 2016.

31. K. E. G. Löbner, "Systematics of absolute transition probabilities of K-forbidden gamma-ray transitions," *Physics Letters*, vol. 26B, no. 6, pp. 369–370, February 1968.

32. P. M. Walker *et al.*, "K-forbidden transitions from multi-quasiparticle states," *Physics Letters B*, vol. 408, pp. 42–46, 1997.

33. A. Bohr and B. R. Mottelson, *Nuclear Structure*, 2nd ed. River Edge, NJ: World Scientific, 1998.

34. N. J. Stone, J. R. Stone, P. M. Walker, and C. R. Bingham, "Quasi-particle and collective magnetism: Rotation, pairing and blocking in high-K isomers," *Physics Letters B*, vol. 726, pp. 675–679, 2013.

35. A. K. Mistry, "In-beam gamma and electron spectroscopy of ^{253}No," Ph.D. dissertation, University of Liverpool, 2014.

36. J. F. Smith, C. J. Chiara, D. B. Fossan, G. J. Lane, J. F. Lewicki, J. M. Sears, and P. Vaska, "Observation of signature inversion in the $\nu(h_{11/2}) \otimes \pi(h_{11/2})$ band of ^{122}Cs," *Physical Review C*, vol. 58, no. 6, pp. 3237 – 3242, 1998.

37. P. Alexander, F. Boehm, and E. Kankeleit, "Spin-23/2^- isomer of ^{177}Lu," *Physical Review*, vol. 133, no. 2B, pp. 284–290, January 1964.

38. C. Wheldon, P. M. Walker, P. H. Regan, T. Saitoh, N. Hashimoto, G. Sletten, and F. R. Xu, "High-K structures and triaxiality in ^{186}Os," *Nuclear Physics A*, vol. 652, pp. 103–131, 1999.

39. C. S. Purry, P. M. Walker, G. D. Dracoulis, S. Bayer, A. P. Byrne, T. Kibédi, F. G. Kondev, C. J. Pearson, J. A. Sheikh, and F. R. Xu, "Rotational and multi-quasiparticle excitations in ^{183}Re," *Nuclear Physics A*, vol. 672, pp. 54–88, 2000.

40. C. Wheldon, G. D. Dracoulis, A. N. Wilson, P. M. Davidson, A. P. Byrne, D. M. Cullen, L. K. Pattison, S. V. Rigby, D. T. Scholes, G. Sletten, and R. Wood, "Gamma-ray spectroscopy of the doubly-odd nuclide ^{184}Re," *Nuclear Physics A*, vol. 763, pp. 1–30, 2005.

41. H. Paetz gen. Shieck, *Nuclear Reactions: An Introduction.* Heidelberg: Springer, 2014.

42. G. L. Molnár, Ed., *Handbook of Prompt Gamma Activation Analysis.* Dordrecht, the Netherlands: Kluwer Academic, 2004.

43. D. A. Matters, A. G. Lerch, A. M. Hurst, L. Szentmiklósi, J. J. Carroll, Z. Révay, J. W. McClory, S. R. McHale, R. B. Firestone, B. W. Sleaford, M. Krtička, and T. Belgya, "Investigation of ^{186}Re via radiative thermal-neutron capture on ^{185}Re," *Physical Review C*, vol. 93, p. 054319, 2016.

44. M. Wang, G. Audi, A. H. Wapstra, F. G. Kondev, M. MacCormick, X. Xu, and B. Pfeiffer, "The AME2012 atomic mass evaluation," *Chinese Physics C*, vol. 36, no. 12, pp. 1603–2014, December 2012.

45. Evaluated Nuclear Data File (ENDF) database. [Online]. Available: http://www.nndc.bnl.gov/exfor/endf00.jsp

46. N. Bohr, "Neutron capture and nuclear constitution," *Nature*, vol. 137, pp. 344–348, February 1936.

47. J. M. Blatt and V. F. Weisskopf, *Theoretical Nuclear Physics.* New York, NY: Dover Publications, Inc., 1991.

48. K. Toshihiko, "Optical and Hauser-Feshbach statistical model code: CoH (ver. 3.4) manual," CoH$_3$ Software Distribution, ver. 3.4, 2015.

49. A. J. Koning, S. Hilaire, and M. C. Duijvestjn. TALYS 1.6 users manual. [Online]. Available: http://www.talys.eu/documentation/

50. T. Kawano, P. Talou, M. B. Chadwick, and T. Watanabe, "Monte Carlo simulation for particle and γ-ray emissions in statistical Hauser-Feshbach model," *Journal of Nuclear Science and Technology*, vol. 47, no. 5, pp. 462 – 469, 2010.

51. A. M. Hurst, "Capture-γ projects using thermal neutrons," Presentation at the University of Oslo, June 2016.

52. F. Bečvář, "Simulation of γ cascades in complex nuclei with emphasis on assessment of uncertainties of cascade-related quantities," *Nuclear Instruments and Methods in Physics Research A*, vol. 417, pp. 434–449, 1998.

53. P. Walker and G. Dracoulis, “Energy traps in atomic nuclei,” *Nature*, vol. 399, pp. 35–40, May 1999.

54. D. Belic *et al.*, “The new photoactivation facility at the 4.3 MV Stuttgart DYNAMITRON: Setup, performance, and first applications,” *Nuclear Instruments and Methods in Physics Research A*, vol. 463, pp. 26–41, 2001.

55. J. J. Carroll, M. S. Litz, K. A. Netherton, S. L. Henriquez, N. R. Pereira, D. A. Burns, and S. A. Karamian, “Nuclear structure and depletion of nuclear isomers using electron linacs,” in *Application of Accelerators in Research and Industry*, vol. 1525, March 2013, pp. 586–594.

56. J. J. Carroll, “Ups and downs of nuclear isomers,” Presentation at the Air Force Institute of Technology, September 2014.

57. G. D. Dracoulis *et al.*, “Connections between high-K and low-K states in the s-process nucleus ^{176}Lu,” *Physical Review C*, vol. 81, p. 011301, 2010.

58. J. J. Carroll *et al.*, “Photoexcitation of nuclear isomers by (γ, γ') reactions,” *Physical Review C*, vol. 43, pp. 1238–1247, 1991.

59. B. Pritychenko, E. Běták, M. A. Kellett, B. Singh, and J. Totans, “The nuclear science references (NSR) database and web retrieval system,” *Nuclear Instruments and Methods in Physics Research A*, vol. 640, pp. 213–218, 2011.

60. R. G. Lanier *et al.*, “Nuclear levels in ^{186}Re,” *Physical Review*, vol. 178, no. 4, pp. 1919–1948, February 1969.

61. J. Glatz, “Untersuchung der Anregungen von ^{186}Re nach der (n,γ)-Reaktion,” *Zeitschrift für Physik*, vol. 265, pp. 335–364, 1973.

62. F. Bečvář, Y. Honzatko, M. Králík, N. D. Nhuan, T. Stadnikov, and S. A. Telezhnikov, “Study of the reaction ^{185}Re(n,γ)^{186}Re in isolated resonances,” *Soviet Journal of Nuclear Physics*, vol. 37, no. 6, pp. 809–814, 1983.

63. C. Wheldon *et al.*, “High-resolution particle spectroscopy of ^{186}Re,” *Journal of Physics G: Nuclear and Particle Physics*, vol. 36, p. 095102, July 2009.

64. R. L. Macklin and P. G. Young, “Neutron capture cross sections of rhenium from 3 to 1900 keV,” *Nuclear Science and Engineering*, vol. 97, pp. 239–244, 1987.

65. R. B. Firestone. “Database of prompt gamma rays from slow neutron capture for elemental analysis,” (International Atomic Energy Agency, Vienna, 2006). [Online]. Available: https://www-nds.iaea.org/pgaa/egaf.html

66. D. A. Matters, “Analysis of the nuclear structure of ^{186}Re using neutron-induced reactions,” Master’s thesis, AFIT-ENP-MS-15-M-098. Graduate School of Engineering and Managment, Air Force Institute of Technology (AU), Wright-Patterson AFB, OH, March 2015 (ADA616795).

67. F. Käppeler, A. Mengoni, M. Mosconi, K. Fujii, M. Heil, C. Domingo-Pardo, and the nTOF collaboration, “Neutron studies for dating the universe,” *Journal of the Korean Physical Society*, vol. 59, no. 2, pp. 2094–2099, 2011.

68. D. Belic *et al.*, “Photoactivation of ^{180}Ta^m and its implication for the nucleosynthesis of nature’s rarest naturally occurring isotope,” *Physical Review Letters*, vol. 83, no. 25, pp. 5242–5245, December 1999.

69. J. J. Carroll, J. A. Anderson, J. W. Glesener, C. D. Eberhard, and C. B. Collins, “Accelerated decay of ^{180}Ta^m and ^{176}Lu in stellar interiors through (γ, γ') reactions,” *The Astrophysical Journal*, vol. 344, pp. 454–459, September 1989.

70. C. B. Collins *et al.*, “Resonant excitation of the reaction ^{180}Ta$^m(\gamma, \gamma')^{180}$Ta,” *Physical Review C*, vol. 42, no. 5, pp. R1813 – R1816, 1990.

71. D. Belic *et al.*, “Photo-induced depletion of the ^{180}Ta^m isomer via low-lying intermediate states: Structure and astrophysical implications,” *Physical Review C*, vol. 65, p. 035801, 2002.

72. P. Mohr, S. Goriely, T. Shizuma, and T. Hayakawa, “The *s*-process branching at ^{186}Re revised,” in *PoS (NIC-IX) 142*, ser. International Symposium on Nuclear Astrophysics – Nuclei in the Cosmos – IX, June 2006.

73. F. Becvar, Y. Gonzatko, M. Kralik, N. D. Nhuan, T. Stadnikov, and S. A. Telezhnikov, “Study of nuclei ^{186}Re levels using reaction ^{185}Re(n, γ)^{186}Re for isolated resonances,” in *Proc. Conf. Neutron Physics, Kiev*, vol. 2, 1980, p. 224.

74. A. J. Koning, S. Hilaire, and M. C. Duijvestijn, “TALYS-1.0,” in *Proceedings of the International Conference on Nuclear Data for Science and Technology*, O. Bersillon, F. Gunsing, E. Bauge, R. Jacqmin, and S. Leray, Eds. EDP Sciences, April 22 – 27, 2007 2008, pp. 211–214.

75. P. W. Lisowski and K. F. Schoenberg, “The Los Alamos Neutron Science Center,” *Nuclear Instruments and Methods in Physics Research Section A*, vol. 562, no. 2, pp. 910–914, June 2006.

76. S. A. Wender *et al.*, “A fission ionization detector for neutron flux measurements at a spallation source,” *Nuclear Instruments and Methods in Physics Research A*, vol. 336, pp. 226–231, 1993.

77. N. Fotiades *et al.*, “Measurements and calculations of ^{238}U$(n, xn\gamma)$ partial γ-ray cross sections,” *Physical Review C*, vol. 69, p. 024601, 2004.

78. P. W. Lisowski, C. D. Bowman, G. J. Russell, and S. A. Wender, "The Los Alamos National Laboratory spallation neutron sources," *Nuclear Science and Engineering*, vol. 106, pp. 208–218, 1990.

79. J. A. Becker and R. O. Nelson, "New opportunities in nuclear science with GEANIE at LANSCE/WNR," *Nuclear Physics News International*, vol. 7, p. 11, June 1997.

80. "MIDAS web page," October 2014. [Online]. Available: https://midas.triumf.ca

81. D. Radford. RADWARE home page. Oak Ridge National Laboratory. [Online]. Available: http://radware.phy.ornl.gov/info.html

82. M. S. Basunia, "Nuclear data sheets for $A = 187$," *Nuclear Data Sheets*, vol. 110, pp. 999–1238, 2009.

83. N. Fotiades, R. O. Nelson, M. Devlin, and J. A. Becker, "New levels and a lifetime measurement in ^{204}Tl," *Physical Review C*, vol. 77, p. 024306, 2008.

84. C. M. Baglin, "Nuclear data sheets for $A = 184$," *Nuclear Data Sheets*, vol. 111, pp. 275–523, 2010.

85. A. G. Lerch, "Nuclear structure of rhenium-186 revealed by neutron-capture gamma rays," Master's thesis, AFIT-ENP-14-M-21. Graduate School of Engineering and Managment, Air Force Institute of Technology (AU), Wright-Patterson AFB, OH, March 2014 (ADA598969).

86. Z. Révay, "Determining elemental composition using prompt γ activation analysis," *Analytical Chemistry*, vol. 81, no. 16, pp. 6851–6859, July 2009.

87. M. Krtička, R. B. Firestone, D. P. McNabb, B. Sleaford, U. Agvaanluvsan, T. Belgya, and Z. Révay, "Thermal neutron capture cross sections of the palladium isotopes," *Physical Review C*, vol. 77, p. 054615, 2008.

88. R. B. Firestone, M. Krtička, Z. Révay, L. Szentmiklósi, and T. Belgya, "Thermal neutron capture cross sections of the potassium isotopes," *Physical Review C*, vol. 87, p. 024605, 2013.

89. H. D. Choi, R. B. Firestone, M. S. Basunia, A. Hurst, B. Sleaford, N. Summers, J. E. Escher, Z. Révay, L. Szentmiklósi, T. Belgya, and M. Krtička, "Radiative capture cross sections of ^{155,157}Gd for thermal neutrons," *Nuclear Science and Engineering*, vol. 177, pp. 219–232, 2014.

90. A. M. Hurst, R. B. Firestone, L. Szentmiklósi, B. W. Sleaford, M. S. Basunia, T. Belgya, J. E. Escher, M. Krtička, Z. Révay, and N. C. Summers, "Radiative thermal neutron-capture cross sections for the ^{180}W(n, γ) reaction and determination of the neutron-separation energy," *Physical Review C*, vol. 92, p. 034615, 2015.

91. C. Genreith, *Partial neutron capture cross sections of actinides using cold neutron prompt gamma activation analysis*, ser. Energie & Umwelt. Forschungszentrum Jülich GmbH, 2015, vol. 250.

92. M. Rossbach *et al.*, “TANDEM: A mutual cooperation effort for transactinide nuclear data evaluation and measurement,” *Journal of Radioanalytical and Nuclear Chemistry*, vol. 304, pp. 1359–1363, 2015.

93. G. Schoeneich, H. Palmedo, C. Dierke-dzierzon, S. C. Mutter, and H. J. Biersack, “Rhenium-186 HEDP: Palliative radionuclide therapy of painful bone metastases: Preliminary results,” *Scandinavian Journal of Urology and Nephrology*, vol. 31, no. 5, pp. 445–448, 1997.

94. F. F. Knapp *et al.*, “Reactor-produced radioisotopes from ORNL for bone pain palliation,” *Applied Radiation and Isotopes*, vol. 49, no. 4, pp. 309–315, 1998.

95. L. Bernstein, D. Brown, A. Hurst, J. Kelly, F. Kondev, E. McCutchan, C. Nesaraja, R. Slaybaugh, and A. Sonzogni, “White paper: Nuclear data needs and capabilities for applications,” Lawrence Livermore National Laboratory, Berkeley, California, Tech. Rep. LLNL-CONF-676585, May 2015. [Online]. Available: http://arxiv.org/abs/1511.07772

96. R. Capote *et al.*, “RIPL – Reference Input Parameter Library for calculation of nuclear reactions and nuclear data evaluations,” *Nuclear Data Sheets*, vol. 110, pp. 3107–3214, 2009.

97. R. M. Lindstrom and Z. Révay, “Beams and Facilities,” in *Handbook of Prompt Gamma Activation Analysis*, G. L. Molnár, Ed. Dordrecht, the Netherlands: Kluwer Academic, 2004, ch. Beams and Facilities, p. 31.

98. L. Szentmiklósi, T. Belgya, Z. Révay, and Z. Kis, “Upgrade of the prompt gamma activation analysis and the neutron-induced prompt gamma spectroscopy facilities at the Budapest research reactor,” *Journal of Radioanalytical and Nuclear Chemistry*, vol. 286, pp. 501–505, 2010.

99. T. Belgya, Z. Kis, and L. Szentmiklósi, “Neutron flux characterization of the cold beam PGAA-NIPS facility at the Budapest research reactor,” *Nuclear Data Sheets*, vol. 119, pp. 419–421, 2014.

100. T. Belgya, “Target preparation for in-beam thermal neutron capture experiments,” in *JRC Scientific and Technical Reports: EFNUDAT Fast Neutrons*, ser. Proceedings of the Scientific Workshop on Neutron Measurements, Theory and Applications, F. J. Hambsch, Ed. Luxembourg: Publications Office of the European Union, 2009, pp. 21–26.

101. Z. Révay, T. Belgya, and G. L. Molnár, “Application of Hypermet-PC in PGAA,” *Journal of Radioanalytical and Nuclear Chemistry*, vol. 265, no. 2, pp. 261–265, 2005.

102. G. L. Molnár, Z. Révay, and T. Belgya, “Wide energy range efficiency calibration method for Ge detectors,” *Nuclear Instruments and Methods in Physics Research A*, vol. 489, pp. 140–159, 2002.

103. Institute of Isotopes, Budapest, “HYPERMET-PC Version 5.01 (v512).” [Online]. Available: http://www.iki.kfki.hu/nuclear/hypc/

104. G. L. Molnár, Z. Révay, and T. Belgya, “Accurate absolute intensities for the ^{35}Cl(n,γ) reaction gamma-ray standard,” *Nuclear Instruments and Methods in Physics Research B*, vol. 213, pp. 32–35, 2004.

105. Z. Révay, R. B. Firestone, T. Belgya, and G. L. Molnár, “Prompt Gamma-Ray Spectrum Catalog,” in *Handbook of Prompt Gamma Activation Analysis*, G. L. Molnár, Ed. Dordrecht, the Netherlands: Kluwer Academic, 2004, ch. Prompt Gamma-Ray Spectrum Catalog, p. 173.

106. Z. Révay and G. L. Molnár, “Standardisation of the prompt gamma activation analysis method,” *Radiochimica Acta*, vol. 91, pp. 361–369, 2003.

107. A. M. Hurst, N. C. Summers, L. Szentmiklósi, R. B. Firestone, M. S. Basunia, J. E. Escher, and B. W. Sleaford, “Determination of the effective sample thickness via radiative capture,” *Nuclear Instruments and Methods in Physics Research B*, vol. 362, pp. 38–44, 2015.

108. R. Nowotny, “XMuDat: Photon attenuation data on PC, Version 1.0.1.” [Online]. Available: https://www-nds.iaea.org/publications/iaea-nds/iaea-nds-0195.htm

109. J. Beringer *et al.* (Particle Data Group), “Review of particle physics,” *Physical Review D*, vol. 86, p. 010001, 2012, G. Cowan, Statistics, p. 390.

110. C. E. Porter and R. G. Thomas, “Fluctuations of nuclear reaction widths,” *Physical Review*, vol. 104, no. 2, pp. 483–491, 1956.

111. S. F. Mughabghab, *Atlas of Neutron Resonances: Resonance Parameters and Thermal Cross Sections, $Z = 1 - 100$*, 5th ed. Elsevier Science, 2006.

112. A. Gilbert and G. W. Cameron, “A composite nuclear-level density formula with shell corrections,” *Canadian Journal of Physics*, vol. 43, no. 8, pp. 1446–1496, 1965.

113. T. D. Newton, “Shell effects on the spacing of nuclear levels,” *Canadian Journal of Physics*, vol. 34, no. 8, pp. 804–829, 1956.

114. T. von Egidy and D. Bucurescu, “Systematics of nuclear level density parameters,” *Physical Review C*, vol. 72, p. 044311, 2005.

115. T. von Egidy and D. Bucurescu, “Experimental energy-dependent nuclear spin distributions,” *Physical Review C*, vol. 80, p. 054310, 2009.

116. S. I. Al-Quraishi, S. M. Grimes, T. N. Massey, and D. A. Resler, “Level densities for $20 \leq A \leq 110$,” *Physical Review C*, vol. 67, p. 015803, 2003.

117. D. M. Brink, “Some aspects of the interaction of fields with matter,” Ph.D. dissertation, University of Oxford, 1955.

118. P. Axel, “Electric dipole ground-state transition width strength function and 7-MeV photon interactions,” *Physical Review*, vol. 126, no. 2, pp. 671–683, April 1962.

119. S. G. Kadmenski, V. P. Markushev, and V. I. Furman, “Radiative widths of neutron resonances, giant dipole resonances,” *Soviet Journal of Nuclear Physics*, vol. 37, no. 2, pp. 165–168, 1983.

120. J. Kopecky and M. Uhl, “Test of gamma-ray strength functions in nuclear reaction model calculations,” *Physical Review C*, vol. 41, p. 1941, 1990.

121. J. Kroll *et al.*, “Strength of the scissors mode in odd-mass Gd isotopes from the radiative capture of resonance neutrons,” *Physical Review C*, vol. 88, p. 034317, 2013.

122. A. M. Goryachev, G. N. Zalesnyi, S. F. Semenko, and B. A. Tulupov, “Giant dipole resonance in nuclei of the transitional region around $A \sim 190$,” *Soviet Journal of Nuclear Physics*, vol. 17, no. 3, pp. 236–239, 1973.

123. S. S. Dietrich and B. L. Berman, “Atlas of photoneutron cross sections obtained with monoenergetic photons,” *Atomic Data and Nuclear Data Tables*, vol. 38, pp. 199–338, 1988.

124. J. Kopecky, “Gamma-ray strength functions,” in *Handbook for calculations of nuclear reaction data.* Vienna, Austria: IAEA, 1998, no. IAEA-TECDOC-1034, ch. Gamma-ray strength functions, p. 97.

125. J. Kopecky, M. Uhl, and R. E. Chrien, “Radiative strength in the compound nucleus ^{157}Gd,” *Physical Review C*, vol. 47, p. 312, 1993.

126. A. Richter, “Shell model and magnetic dipole modes in deformed nuclei,” *Nuclear Physics A*, vol. 507, pp. 99c–128c, 1990.

127. J. Speth and A. van der Woude, “Giant resonances in nuclei,” *Reports on Progress in Physics*, vol. 44, pp. 719–786, 1981.

128. W. V. Prestwich, M. A. Islam, and T. J. Kennett, “Primary $E2$ transitions observed following neutron capture for the mass region $144 \leq A \leq 180$,” *Zeitschrift für Physik A - Atoms and Nuclei*, vol. 315, pp. 103–111, 1984.

129. S. C. Wu, "Nuclear data sheets for $A = 185$," *Nuclear Data Sheets*, vol. 106, pp. 619–812, 2005.

130. L. Seren, H. N. Freidlander, and S. H. Turkel, "Thermal neutron activation cross sections," *Physical Review*, vol. 72, no. 10, pp. 888–901, November 1947.

131. H. Pomerance, "Thermal neutron capture cross sections," *Physical Review*, vol. 88, no. 2, pp. 412–413, October 1952.

132. W. S. Lyon, "Reactor neutron activation cross sections for a number of elements," *Nuclear Science and Engineering*, vol. 8, pp. 378–380, 1960.

133. R. A. Karam, T. F. Parkinson, and W. H. Ellis, "Final technical report on the nuclear properties of rhenium," University of Florida, Gainesville, FL, Tech. Rep. DTIC AD0402668, 1963.

134. S. J. Friesenhahn, D. A. Gibbs, E. Haddad, F. H. Fröhner, and W. M. Lopez, "Neutron capture cross sections and resonance parameters of rhenium from 0.01 eV to 30 keV," *Journal of Nuclear Energy*, vol. 22, pp. 191–210, 1968.

135. R. E. Heft, "A consistent set of nuclear parameters: Values for absolute INAA," Lawrence Livermore National Laboratory, Tech. Rep. UCRL-80286, May 1980.

136. F. De Corte and A. Simonits, "Recommended nuclear data for use in the k_0 standardization of neutron activation analysis," *Atomic Data and Nuclear Data Tables*, vol. 85, pp. 47–67, 2003.

137. F. Farina Arboccò, P. Vermaercke, K. Smits, S. L., and K. Strijckmans, "Experimental determination of k_0, Q_0, $\bar{E}_r$ factors and neutron cross-sections for 41 isotopes of interest in Neutron Activation Analysis," *Journal of Radioanalytical and Nuclear Chemistry*, vol. 296, pp. 931–938, 2013.

138. G. D. Dracoulis and A. P. Byrne, "Annual Report," Australian National University, Tech. Rep. ANU-P/1052, 1989.

139. K. Hatanaka, "RCNP cyclotron facility," *Journal of the Korean Physical Society*, vol. 54, no. 5, pp. 1937–1941, 2009.

140. D. C. Radford, "ESCL8R and LEVIT8R: Software for interactive graphical analysis of HPGe coincidence data sets," *Nucl. Instr. Meth. A*, vol. 361, pp. 297–305, 1995.

141. D. C. Radford, "Background subtraction from in-beam HPGe coincidence data sets," *Nucl. Instr. Meth. A*, vol. 361, pp. 306–316, 1995.

142. P. Möller, J. R. Nix, W. D. Myers, and W. J. Swiatecki, "Nuclear ground-state masses and deformations," *Atomic Data and Nuclear Data Tables*, vol. 59, pp. 185–381, 1995.

143. W. Nazarewicz, M. A. Riley, and J. D. Garrett, "Equilibrium deformations and excitation energies of single-quasiproton band heads of rare-earth nuclei," *Nuclear Physics A*, vol. 512, pp. 61–96, 1990.

144. K. Jain, O. Burglin, G. D. Dracoulis, B. Fabricius, N. Rowley, and P. M. Walker, "Multi-quasiparticle states in the mass-180 region," *Nuclear Physics A*, vol. 591, pp. 61–84, 1995.

Vita

Major David Matters grew up in San Jose, CA. He earned his commission as a second lieutenant in the Aviation Branch in 2004 from the University of San Francisco Army ROTC program before attending the Aviation Officers' Basic Course at Ft. Rucker, AL. He graduated from rotary-wing flight training in January 2006 as a rated pilot in the OH-58D(R) Kiowa Warrior scout/attack helicopter. From 2006 to 2008, he served as an Assistant Operations Officer and Platoon Leader in 1-25 Aviation Regiment (Attack) and 2-6 Cavalry Regiment at Wheeler Army Airfield, HI, and Kirkuk, Iraq. From 2008 to 2009, he served in the 3/25 Infantry Brigade Combat Team as an Assistant Brigade Aviation Officer and Future Plans Officer at Schofield Barracks, HI, and Tikrit, Iraq. Following completion of the Military Intelligence Captains' Career Course at Ft. Huachuca, AZ, in 2010, Major Matters commanded B Troop, 4-6 Attack Reconnaissance Squadron and served as the Operations Officer for the 46th Aviation Support Battalion at Joint Base Lewis-McChord, WA. In 2013, he transitioned to Functional Area 52 (Nuclear and Counterproliferation) and began his studies at the Air Force Institute of Technology.

Major Matters holds a Bachelor of Arts degree in Mathematics from the University of California, Berkeley, a Master of Arts degree in Mathematics from San Francisco State University, a Master of Business Administration degree from Webster University, and a Master of Science degree in Nuclear Engineering from the Air Force Institute of Technology. His awards and decorations include the Bronze Star (two awards), the Air Medal (three awards), the Meritorious Service Medal, the Army Commendation Medal (two awards), the Army Achievement Medal (two awards), and the Iraq Campaign Medal (three awards). He also holds the Aviator Badge, Air Assault Badge, and the Combat Action Badge. Following graduation, Major Matters will be assigned to the Defense Threat Reduction Agency at Ft. Belvoir, VA.

REPORT DOCUMENTATION PAGE

Form Approved
OMB No. 074-0188

1. REPORT DATE *(DD-MM-YYYY)* 24-12-2016	**2. REPORT TYPE** Ph.D. Dissertation	**3. DATES COVERED** *(From – To)* Mar 2015 – Dec 2016

4. TITLE AND SUBTITLE
Nuclear Structure of 186-Re

5a. CONTRACT NUMBER

5b. GRANT NUMBER

5c. PROGRAM ELEMENT NUMBER

6. AUTHOR(S)
Matters, David A., Major, USA

5d. PROJECT NUMBER

5e. TASK NUMBER

5f. WORK UNIT NUMBER

7. PERFORMING ORGANIZATION NAMES(S) AND ADDRESS(S)
Air Force Institute of Technology
Graduate School of Engineering and Management (AFIT/EN)
2950 Hobson Way, Building 640
Wright-Patterson AFB, OH 45433-7765

8. PERFORMING ORGANIZATION REPORT NUMBER
AFIT-ENP-DS-16-D-017

9. SPONSORING/MONITORING AGENCY NAME(S) AND ADDRESS(ES)
Bill Ulycni (william.ulycni@dhs.gov)
Department of Homeland Security – DNDO
MGMT/OPO/Mailstop 0115
245 Murray Lane SW
Washington, DC 20528-0115

10. SPONSOR/MONITOR'S ACRONYM(S)
DHS – DNDO

11. SPONSOR/MONITOR'S REPORT NUMBER(S)
HSHQDC-14-X-00089

12. DISTRIBUTION/AVAILABILITY STATEMENT
Distribution Statement A. Approved for Public Release; Distribution Unlimited

13. SUPPLEMENTARY NOTES
This material is declared a work of the U.S. Government and is not subject to copyright protection in the United States.

The unstable odd-*Z*, odd-*N* isotope ^{186}Re exists in a mid-shell deformed region of the chart of the nuclides where long-lived nuclear isomers are common. ^{186}Re (ground-state half-life $T_{1/2}$=3.7186 d) has an isomer with a half-life of $\sim 2.0 \times 10^5$ y. The ^{186m}Re isomer is a candidate energy-storage medium for a radioisotope power source of military importance that would operate on the principle of isomer depletion. Data about levels and transitions above the ^{186m}Re isomer, absent from the adopted level scheme for ^{186}Re, are needed to identify a means of depleting the isomer. Four experiments were performed to investigate the ^{186}Re level structure, which involved three different reactions: ^{187}Re(n,2nγ)^{186}Re, ^{185}Re(n,γ)^{186}Re, and ^{186}W(d,2nγ)^{186}Re. In each of these experiments, γ-ray spectra from the decay of excited states in ^{186}Re were measured and analyzed to reveal information about the discrete-level structure of ^{186}Re. This work resulted in new information about γ-ray transitions that feed the ^{186m}Re isomer, an improved value for the excitation energy of the isomer, independent measurements of the ^{186}Re neutron-separation energy and the cross section for thermal-neutron capture on ^{185}Re, and numerous γ-ray transitions and levels in ^{186}Re which are not included in the adopted level scheme.

15. SUBJECT TERMS
Nuclear Structure, Nuclear Reactions, Nuclear Isomers, 186-Rhenium

16. SECURITY CLASSIFICATION OF:			**17. LIMITATION OF ABSTRACT**	**18. NUMBER OF PAGES**	**19a. NAME OF RESPONSIBLE PERSON**
a. REPORT	**b. ABSTRACT**	**c. THIS PAGE**			Dr. John W. McClory
U	U	U	UU	164	**19b. TELEPHONE NUMBER** *(Include area code)* (937)255-6565 x7308

Standard Form 298 (Rev. 8-98)
Prescribed by ANSI Std. Z39-18